



Title	Computation of the Propeller-Hull and Propeller-Hull-Rudder Interaction Using Simple Body-Force Distribution Model
Author(s)	Win, Yan Naing
Citation	大阪大学, 2014, 博士論文
Version Type	VoR
URL	https://doi.org/10.18910/50514
rights	
Note	

The University of Osaka Institutional Knowledge Archive : OUKA

<https://ir.library.osaka-u.ac.jp/>

The University of Osaka

Doctoral Dissertation

Computation of the Propeller-Hull and
Propeller-Hull-Rudder Interaction Using
Simple Body-Force Distribution Model

YAN NAING WIN

July 2014

Graduate School of Engineering,
Osaka University

TABLE OF CONTENTS

List of symbols.....	1
List of tables.....	7
List of figures.....	8
CHAPTER 1: INTRODUCTION.....	15
1.1 Literature Review.....	15
1.2 Research Histories.....	16
1.3 Objectives and Scopes of the Work.....	17
CHAPTER 2: CFD METHODS.....	20
2.1 Overview of CFDSHIP-Iowa Version 4.....	20
2.2 Mathematical Model of the Code.....	21
2.2.1 Governing Equations.....	21
2.2.2 Turbulence Model.....	22
2.2.3 Single Phase Level-Set Free Surface Model.....	24
2.3 Grids, Computational Domain and Boundary Conditions.....	25
2.3.1 S60 Case.....	25
2.3.2 KVLCC2 Case.....	28
2.4 Propeller Model.....	32
2.5 EFD Backgrounds.....	37

2.5.1 S60 case	37
2.5.2 KVLCC2 case	38
CHAPTER 3: Without-Hub Computation of S60.....	41
3.1 Bare Hull Computation.....	41
3.2 Coupled computation of ship hull and propeller.....	49
3.2.1 Convergence history and propulsive quantities.....	49
3.2.2 Analysis of wake field behind the rotating propeller.....	51
3.2.3 Propeller hull interaction.....	67
3.3 Computation of load-varying test.....	71
CHAPTER 4: WITH-HUB COMPUTATION OF S60.....	75
4.1 Overview of computational condition.....	75
4.2 Propulsive quantities and flow field analyses.....	76
CHAPTER 5: COMPUTATION OF KVLCC2 MODEL.....	86
5.1 Overview of computation.....	86
5.2 Nominal wake field analysis.....	89
5.3 Wake field analyses at the model point	93
5.3.1 Without-rudder case.....	93
5.3.2 With-rudder case	99
5.4 Wake field analyses at the ship point	109
5.5 Comparison with real geometry propeller computation and other body-force propeller models	114

5.4 Discussion and summary	118
CHAPTER 6: STUDY OF COORDINATE SYSTEMS.....	120
6.1 Overview of computational coordinates.....	120
6.2 Ship geometry and grid generation	121
6.3 Coordinate transformation	123
6.4 Computations of maneuvering motions.....	125
6.5 Conclusion	129
CHAPTER 7: SUMMARY AND CONCLUSION.....	130
7.1 Summary of the thesis.....	130
7.1.1 S60 cases.....	130
7.1.2 KVLCC2 case	132
7.2 Overall conclusion.....	133
Reference.....	136
Appendix A.....	140
Appendix B.....	142
Appendix C.....	145
Acknowledgements.....	146
List of publications.....	148
Curriculum vitae.....	150

List of symbols

a_{rel}	: Source term of NS equation in non-inertial coordinate
A_e	: Expanded area of propeller
A_0	: Disc area of propeller
AP	: Aft perpendicular
B_{wl}	: Breadth at designed water line
c	: Chord length of the blade
CB	: Center of Buoyancy
C_B	: Block coefficient
C_D	: Drag coefficient
C_L	: Lift coefficient
CM	: Metacentric height
C_P	: Pressure coefficient
C_T	: Loading coefficient
$CD_{k\omega}$: Positive portion of the cross-diffusion in ω – transport equation
dL	: Segmental lift coefficient
dD	: Segmental drag coefficient
dT	: Segmental thrust force
dQ	: Segmental torque force
D	: Depth of the ship hull
Dia	: Diameter of the propeller
F	: Blade correction factor

FP	: Forward perpendicular
F_1	: Weight function
f_{b_i}	: Body-Force non-dimensionalized by $\rho U_0^2 / L_{PP}$
f_{bX}	: Body-force component in X-direction
f_{bY}	: Body-force component in Y-direction
f_{bZ}	: Body-force component in Z-direction
$f_{b\theta}$: Tangential body-force
f_{tip}	: Parameter for computing tip correction factor
Fr	: Froude number
g	: gravity
H	: Geometric Pitch of the blade
H_e	: Effective Pitch of the blade ($1.08H$)
J_a	: Advance ratio on advanced speed
J_s	: Advance ratio on Ship Speed
k	: Turbulent kinetic energy
kn	: Knots
K_T	: Thrust coefficient
K_Q	: Torque coefficient
L	: Ship length
L_1	: Distance between AP and LCF
L_2	: Distance between FP and LCF
LCB	: Longitudinal center of buoyancy (%)
LCF	: Longitudinal center of floatation
L_{PP}	: Ship length between perpendiculars

L_{wl}	: Ship length at designed water line
n_{rev}	: Propeller revolution rate
n	: Normal vector
N	: Number of blade
\hat{p}	: Piezometric pressure
p_a	: Air Pressure
p	: Total pressure
P	: Pitch of the propeller
Q	: Torque force
	: Q-criterion
r	: Radial distance from propeller center along the propeller blade
\mathbf{r}	: Moment arm of rotational motion
R	: Propeller radius
$\ddot{\mathbf{R}}$: Translational motion
Re	: Reynolds number
R_B	: Hub radius
R_T	: Resistance with propeller
R_{T0}	: Bare hull resistance
S	: Hull surface area
S_{ij}	: Strain rate
$1 - t'$: Thrust deduction factor
t	: Time in non-inertial coordinate system
t''	: Time in inertial coordinate system
T	: Thrust force

T'	: Period for maneuvering motions
$u_i = (u, v, w)$: Dimensional mean velocity components
U_t	: Total axial velocity component at propeller plane
$U_i = (U, V, W)$: Non-dimensional mean velocity components
U_a	: Advanced speed
U_0	: Ship speed
U'_i, U'_j	: Fluctuation velocities
ΔU	: Axial velocity difference
V_θ	: Tangential velocity at propeller plane
V_g	: Grid velocity
V_r	: Relative velocity in non-inertial coordinate system
V_R	: Resultant inflow velocity at propeller plane
w	: effective wake factor
W_{ij}	: Vorticity tensor
ΔX	: Grid spacing in X-direction
Y_{SC}	: Y position of shaft center line
z_a	: Trim at aft perpendicular
z_f	: Trim at forward perpendicular
Z_{SC}	: Z position of shaft center line
x, y, z	: Cartesian coordinate in dimensions
x', y', z'	: Non-dimensionalized Cartesian coordinate in non-inertial frame
$X, Y, Z = (\frac{x}{L_{PP}}, \frac{y}{L_{PP}}, \frac{z}{L_{PP}})$: Cartesian coordinate non-dimensionalized by L_{PP}
X', Y', Z'	: Non-dimensionalized Cartesian coordinates in inertial frame

Greek symbols

$\alpha_0, \alpha_{g0}, \alpha_{g1}$: Angles used in blade element
β, β^*, α	: Turbulence model coefficients
δ	: Wall distance
δ_{ij}	: Kronecker delta
ξ, η, ζ	: Non-orthogonal curvilinear coordinates
ε	: Dissipation of kinetic energy of turbulence
k_1	: Blade-to-blade interaction effect
k	: Kinetic energy of turbulence
k_{fs}	: Inlet boundary condition of turbulence kinetic energy
μ	: Dynamic viscosity
ν	: Kinematic viscosity (μ / ρ)
ν_t	: Eddy viscosity
φ	: Hydrodynamic pitch angle
ϕ	: 3D level set function
Φ	: Angle of circular motion test with respect to the center of rotation
Ω	: Rotational term
Ω_{lm}	: Vorticity tensor
$ \Omega_{lm} $: Scalar quantity of vorticity tensor
ω	: Specific dissipation of turbulence kinetic energy
ω_{fs}	: Inlet boundary condition of ω
ω'	: Angular frequency
ρ	: Water density

σ_k, σ_ω	: Turbulence model coefficients
θ	: Arbitrary angles by the Y- and Z- grid positions at propeller plane
Θ	: Yaw angle
ϑ	: Trim angle
τ	: Time in curvilinear coordinates

List of tables

Table 2-1 Details of Grids for without-hub condition (S60).....	26
Table 2-2 Details of Grids for with-hub condition (S60).....	26
Table 2-3 Boundary Conditions for both S60 and KVLCC2 models.....	28
Table 2-4 KVLCC2 geometry data	29
Table 2-5 Details of Grids for without-rudder condition (KVLCC2).....	30
Table 2-6 Details of Grids for with-rudder condition (KVLCC2).....	30
Table 3-1 Comparison of EFD and other propeller models.....	50
Table 3-2 Propulsive quantities at various loadings.....	72
Table 5-1 Comparison of propulsive identities.....	88
Table 5-2 Running conditions of the computations by IIHR	116
Table 5-3 Comparison for all four propeller models	117

List of figures

Figure 2-1 Overset grid system with seven blocks (five for without-hub case): boundary layer, hub, propeller, background and refinement and overset view in the stern part	27
Figure 2-2 Overset grid systems, nine blocks for without-rudder case and eleven blocks for with-rudder case: boundary layer, stern, hub, propeller, rudder, wake refinement and background and overset view in the stern part.....	31
Figure 2-3 Blade element theory	33
Figure 2-4 Chord length distribution of S60 propeller.....	36
Figure 2-5 Chord length distribution of KVLCC2 propeller	36
Figure 2-6 Pitch distribution of KVLCC2 propeller	36
Figure 2-7 KVLCC2 ship model, propeller models (left handed and right handed), rudder model and coordinate system	39
Figure 2-8 Experimental set up for PIV measurement.....	40
Figure 3-1 Comparison of axial velocity profiles between CFD (a) and EFD (b) at X=0.8 section.....	43
Figure 3-2 Comparison of axial velocity profiles between CFD (a) and EFD (b) at X=0.9 section	44
Figure 3-3 Comparison of axial velocity profiles between CFD (a) and EFD (b) at X=0.95 section.....	44
Figure 3-4 Comparison of axial velocity profiles between CFD (a) and EFD (b) at X=0.975 section.....	45
Figure 3-5 Comparison of axial velocity profiles between CFD (a) and EFD (b) at	

X=0.9875 section.....	46
Figure 3-6 Comparison of cross-flow components between CFD (a) and EFD (b) at X=0.9875 section.....	46
Figure 3-7 Comparison of U at X=0.9875 for each Z section.....	47
Figure 3-8 Comparison of V at X=0.9875 for each Z section.....	47
Figure 3-9 Comparison of W at X=0.9875 for each Z section.....	48
Figure 3-10 Comparison of C_p at X=0.9875 for each Z section.....	48
Figure 3-11 Convergence history of thrust and torque.....	50
Figure 3-12 Comparison of axial velocity profiles between CFD (a) and EFD (b) at X=0.98125 section.....	54
Figure 3-13 Comparison of cross-flow components between CFD (a) and EFD (b) at X=0.98125 section	55
Figure 3-14 Comparison of axial velocity profiles between CFD (a) and EFD (b) at X=1 section	56
Figure 3-15 Comparison of cross-flow components between CFD (a) and EFD (b) at X=1 section	56
Figure 3-16 Comparison of axial velocity profiles between CFD (a) and EFD (b) at X= 1.01875 section	57
Figure 3-17 Comparison of cross-flow components between CFD (a) and EFD (b) at X=1.01875 section	58
Figure 3-18 Comparison of axial velocity profiles between CFD (a) and EFD (b) at X=1.05 section	58
Figure 3-19 Comparison of cross-flow components between CFD (a) and EFD (a) at X=1.05 section	59

Figure 3-20 Comparison of axial velocity profiles between CFD (a) and EFD (b) at X=1.1 section	60
Figure 3-21 Comparison of cross-flow components between CFD (a) and EFD (b) at X=1.1 section	60
Figure 3-22 Comparison of U at X=0.98125 for each Z section.....	61
Figure 3-23 Comparison of V at X=0.98125 for each Z section	61
Figure 3-24 Comparison of W at X=0.98125 for each Z section.....	62
Figure 3-25 Comparison of C_p at X=0.98125 for each Z section.....	62
Figure 3-26 Comparison of U at X=1 for each Z section.....	63
Figure 3-27 Comparison of V at X=1 for each Z section.....	63
Figure 3-28 Comparison of W at X=1 for each Z section.....	64
Figure 3-29 Comparison of C_p at X=1 for each Z section.....	64
Figure 3-30 Comparison of U at X=1.1 for each Z section.....	65
Figure 3-31 Comparison of V at X=1.1 for each Z section.....	65
Figure 3-32 Comparison of W at X=1.1 for each Z section.....	66
Figure 3-33 Comparison of C_p at X=1.1 for each Z section.....	66
Figure 3-34 Axial-velocity difference ΔU between the with- and without- propeller conditions for upstream of propeller.....	68
Figure 3-35 Axial-velocity difference ΔU between the with- and without- propeller conditions for downstream of propeller.....	69
Figure 3-36 Surface-pressure distributions: pressure contours (CFD)	70
Figure 3-37 Surface-pressure distributions: pressure contours (EFD)	70
Figure 3-38 Surface-pressure distribution: stream-wise variation (a) Z= -0.008 (b) Z=-0.016 (c) Z=-0.023 (d) Z= -0.031 (e) Z=-0.038 (f) Z=-0.046	71

Figure 3-39 Thrust and torque coefficients of load varying test	72
Figure 3-40 Total resistance comparison of bare hull and with propeller case ...	73
Figure 3-41 Wake fraction with respect to the loading coefficients	73
Figure 4-1 Rotational boundary condition on the hub surface.....	76
Figure 4-2 Comparison of axial velocity profiles between CFD (a) and EFD (b) at X=0.9875 section.....	77
Figure 4-3 Comparison of axial velocity profiles between CFD (a) and EFD (b) at X=1 section	79
Figure 4-4 Comparison of cross-flow components between CFD (a) and EFD (b) at X=1 section	80
Figure 4-5 Comparison of cross-flow components of the computation between with-hub and without-hub conditions at X=1 section	81
Figure 4-6 Comparison of U at X=1 for each Z section.....	82
Figure 4-7 Comparison of V at X=1 for each Z section.....	82
Figure 4-8 Comparison of W at X=1 for each Z section.....	83
Figure 4-9 Comparison of C_p at X=1 for each Z section.....	83
Figure 4-10 Surface pressure distribution of CFD results.....	85
Figure 5-1 Trim position of KVLCC2 model experiment.....	87
Figure 5-2 Positions of the measurements.....	88
Figure 5-3 Comparison of axial velocity field at X=0.9825 (a) CFD (b) Original EFD (c) Corrected EFD	91
Figure 5-4 Comparison of axial velocity field at X=1 (a) CFD (b) Original EFD ...	91
Figure 5-5 Computational output of the axial velocity layout at X=0.98	92
Figure 5-6 Comparison of axial velocity (a) CFD (b) EFD and cross-flow	

components (c) CFD (d) EFD at X=0.9625 section for without-rudder case.....	93
Figure 5-7 Comparison of axial velocity field (a) CFD (b) EFD and cross-flow components (c) CFD (d) EFD at X=0.975 section for without-rudder case	96
Figure 5-8 Comparison of axial velocity (a) CFD (b) EFD and cross-flow components (c) CFD (d) EFD at X=0.9890625 section for without-rudder case.....	97
Figure 5-9 Comparison of axial velocity (a) CFD (b) EFD and cross-flow components (c) CFD (d) EFD at X=1 section for without-rudder case	98
Figure 5-10 Comparison of axial velocity (a) CFD (b) EFD and cross-flow components (c) CFD (d) EFD at X=0.9625 section for with-rudder case	102
Figure 5-11 Comparison of axial velocity (a) CFD (b) EFD and cross-flow components (c) CFD (d) EFD at X=0.97625 section for with-rudder case	103
Figure 5-12 Comparison of axial velocity (a) CFD (b) EFD and cross-flow components (c) CFD (d) EFD at X=0.9890625 section for with-rudder case	104
Figure 5-13 Comparison of axial velocity (a) CFD (b) EFD and cross-flow components (c) CFD (d) EFD at X=1 section for with-rudder case	106
Figure 5-14 Comparison of axial velocity (a) CFD (b) EFD and cross-flow components (c) CFD (d) EFD between CFD and EFD at X=1.025 section for with-rudder case	107
Figure 5-15 Comparison of axial velocity between CFD and EFD at X=1.025 for each vertical position (a) Z=-0.03 (b) Z=-0.035 (c) Z=-0.04 (d) Z=-0.045 (e) Z=-0.05 (f) Z=-0.055 (g) Z=-0.06	108
Figure 5-16 Surface pressure distribution of KVLCC2 for with-rudder case.....	109
Figure 5-17 Comparison of Axial Velocity (a) CFD (b) EFD and cross-flow vectors	

(c) CFD (d) EFD at X=1.0 for with-rudder case at ship point.....	110
Figure 5-18 Comparison of Axial Velocity (a) CFD (b) EFD and cross-flow vectors	
(c) CFD (d) EFD at X=1.01875 for with-rudder case at ship point	111
Figure 5-19 Comparison of Axial Velocity (a) CFD (b) EFD and cross-flow vectors	
(c) CFD (d) EFD at X=1.01875 for with-rudder case at ship point	112
Figure 5-20 Comparison of axial velocity at ship point between CFD and EFD at X=1.025 for each vertical position (a) Z=-0.03 (b) Z=-0.035 (c) Z=-0.04 (d) Z= -0.05 (f) Z=-0.055 (g) Z=-0.06	113
Figure 5-21 Comparison of axial velocity profiles at X=1 (a) Actual Propeller (b) Axisymmetric Model (c) Yamazaki Model (d) Current Propeller Model	116
Figure 5-22 Illustration of Q-criterion for Q=5000 colored by the axial velocity contours (a) Actual Propeller (b) Axisymmetric Model	117
Figure 5-23 Illustration of Q-criterion for Q=5000 colored by the axial velocity contours (a) Yamazaki Model (b) Current Propeller Model	118
Figure 6-1 Grid domain with different coordinate systems definitions	123
Figure 6-2 Moving grid geometry	124
Figure 6-3 Motion algorithms of CMT test	127
Figure 6-4 Pressure force distributions on the hull	128
Figure 6-5 Shear force distributions on the hull	128
Figure 6-6 Hydrodynamics forces on the hull in CMT test	129

THIS PAGE IS INTENTIONALLY LEFT BLANK

CHAPTER 1: INTRODUCTION

1.1 LITERATURE REVIEW

The study of propeller-hull and propeller-hull-rudder interaction is important to predict the efficiency of the propeller as well as its influences on the resistance of the ship hull. By the Computational Fluid Dynamics (CFD) method, the viscous flow computation of the ship hull is normally coupled with some propeller programs either by viscous method or by potential method. In the viscous model, the propeller, hull and rudder geometries are all resolved directly in the RANS grid in which the solid bodies are considered as no-slip faces and all of these become parts of the viscous flow solution. This method gives very detailed information about the stern and propeller flows, but the grid generation is considerably complicated and unsteady flow simulation is required. For some applications, the high level of details about the propeller flow itself is not required, so the inviscid approach can be applied. In this approach, both hull and rudder are still modeled geometrically in the RANS grid, but a parameter so called body-force field, which reflects the time-averaged influence of the propeller on the fluid in the propeller region, substitutes for the propeller geometry. The applied body-force fields are usually calculated by means of potential theory-based propeller models, but depending on how the individual propeller models are coupled with the RANS solver, they can be divided into prescribed and interactive models. In the prescribed model, the body-force field is calculated only once and then inserted into the RANS solver. Usually, the model is based on very few input parameters and simple equations. These will give a crude body-force distribution, but based on the nominal flow, the model

cannot account for the mutual interaction between the propeller and the hull/rudder flows but this model is still widely used for some specific purposes. In the interactive model, the propeller and RANS codes are run in turn to iterate towards a solution, which takes the effective propeller inflow into account. The propeller models applied in connection with the interactive approach range from relatively simple models such as lifting line type model to vortex lattice or even surface singularity potential flow models. Currently, the interactive model developed by Kyushu University which is known as Yamazaki Model is well known and is widely used over the world.

1.2 RESEARCH HISTORIES

Stern (et al., 1988a) presented a comprehensive viscous method for the computation of propeller-hull interaction in which a numerical method for calculating the viscous flow over and in the wake of a ship is coupled with a propeller-performance program in an interactive and iterative manner to predict the combined flow field which is completed by Stern (et al., 1988b) in the validation of the method. There also had axisymmetric body-force propeller model of Hough and Ordway (Stern et al., 1991) in which the thrust and torque of the propeller is prescribed and the propeller performance program gives the body-force to give the propulsive force for the ship. In 1990, Kim and Stern developed a “complete” viscous-solution method for rotating propeller blades to treat the complex blade-to-blade flow. After the publication of Stern (et al., 1988a), a number of researchers have pursued essentially the same approach to propeller-hull interaction (Piquet et al., 1987, Yang et al., 1990, Dai et al., 1991, Zhang et al., 1991).

Simonsen (et al., 2005) presented a model that interactively determines

propeller-hull interaction with a simplified potential theory-based infinite-bladed propeller model coupled with RANS code CFDSHIP-IOWA. Takada and El Moctar (et al., 2000), Kawamura (et al., 1997), Chou (et al., 2000), Tahara and Ando (et al., 2000), and Simonsen and Cross-Whiter (et al., 2002) have presented different propeller models ranging from prescribed models to interactive panel models in the calculation of body-force field for the case of propeller behind the ship without rudder. In Abdel-Maksoud (et al., 2000), a propeller behind a ship is modeled by its real geometry.

1.3 OBJECTIVES AND SCOPES OF THE WORK

Many researchers have presented several kinds of different propeller models and proved the advantage of each method. This research will present the traditional propeller-hull interaction problem but in different approach with simplicity. A simple body-force distribution model has been developed in the author's laboratory of Osaka University and the propeller model has proved its capability in the open water computation and its characteristics got good agreements with experiment. The very first idea was proved by using the polar type grid for the body-force computation (Kuroda et al., 2012). After that, the research has been extended by using the Cartesian rectangular grid type to show that the method can be applied in any types of grid (Yokota et al., 2013) and consequently, other improvements such as the simulations in several immersions to learn the free surface effect on the propeller by this method (Emel et al., 2014). All of these open water computations give very good agreement with the corresponding experiment data. However, the capability and application of the model will still need to prove in the complicated wake field behind the ship to convince

whether it can predict the propulsive identities reasonably or not. This brings the current research into the author's hand and this thesis will mainly discuss about the propeller-hull interaction and propeller-hull-rudder interaction by coupling the proposed propeller model with the RANS code and the flow behaviors as well as the propulsive quantities will be analyzed in details. In general the objectives of the research are

- (1) To prove that the proposed simple body-force distribution model is working well in the wake field of ship
- (2) To study the Propeller-Hull and Propeller-Hull-Rudder interaction using the proposed propeller model and validate with experimental results as well as to point out the advantages of this new proposal over the other methods
- (3) To study the importance of the inclusion of the rotational effect of hub in the computation of propeller force

For the current research, the Series 60 $C_B=0.6$ hull form (which will be abbreviated as S60 throughout this thesis) is selected as a representative fine hull form. It is conceived to provide systematic information on the design of lines for single-screw merchant ships. A full account of the original methodical series is provided by Todd (et al., 1963) and the parent form was designed based on considerations of then successful ship designs. The propeller is the MAU methodical series with 5 blades and located with the shaft immersion ratio, 0.88. Moreover, the research is extended to the second variant of Korean tanker known as KVLCC2 which was designed at the Korea Research Institute for Ships and Ocean Engineering around 1997 to be used as a test case for CFD predictions. Not only in CFD, but several extensive research activities are also being carried out by EFD method. Ranging from nominal wake measurements to

seakeeping predictions, the ship model is largely employed by many institutes. In this thesis, the propeller-hull-rudder interaction will be the study case by using KVLCC2 hull.

The thesis will cover four main parts of study cases: the propeller-hull interaction without-hub condition of S60 ship, with-hub condition of S60 ship, the without-rudder computation and with-rudder computation of KVLCC2 model. In general overview of the thesis, in Chapter 2, the computational background, the governing equations, turbulence models will be explained in the mathematical way. The chapter will also include the explanations on the mesh generation of the overset grid type by using PointWise Gridgen software and the theoretical description of the proposed propeller model.

The background of computation, the result and discussion of the results with Experimental Fluid Dynamics (EFD) data for S60 hull are discussed thoroughly in Chapter 3 and 4. The propeller-hull and propeller-hull-rudder interaction case for KVLCC2 ship is explained and discussed in Chapter 5. The study of coordinate systems is explained in Chapter 6 as the proposed propeller model is intended for the self-propulsion test in inertial coordinate system. But, due to the lack of time, these parts are out of scope and marked as future plan so that only the coordinate analysis is studied. The conclusion section in Chapter 7 includes the summary of the research and points out the necessary works that need to be carried out in the future.

CHAPTER 2: CFD METHODS

2.1 OVERVIEW OF CFDSHIP-IOWA VERSION 4

CFDSHIP-Iowa v4.0 (Carrica et al., 2010) is used for the CFD computations. It is an unsteady single-phase level-set solver with dynamic overset grids designed for ship applications using either absolute or relative inertial non-orthogonal curvilinear coordinate system for arbitrary moving but non-deforming control volumes. It solves the continuity and unsteady incompressible RANS equation using a Menter's blended $\kappa - \varepsilon / \kappa - \omega$ model for turbulence with wall-function option and with capabilities for detached eddy simulation (DES) turbulence modeling. A multi-block dynamic overset grid approach is used to allow relative motions between the grids for 6DoF ship motions. Captive, semi-captive, and full 6DoF capabilities for multi-objects with parent/child hierarchy are available but 6DoF function is deleted out in the present work and only the static overset grid system is used. The computation is performed for the ship-fixed case parallelization with MPI-based domain decomposition wherein each grid block is partitioned into sub-blocks by the user by specifying the number of times the grid needs to be split in I, J and K directions. The code provides propeller modeling using simplified body-force or direct discretization and has a proportional-integral-differential (PID) controller to allow self-propulsion or auto-piloted simulations.

The governing equations are discretized using finite difference schemes on body-fitted curvilinear grids. In the turbulence and momentum equations, the time derivatives are discretized using second order finite Euler backward difference, the convection terms are discretized with higher order upwind formula, and viscous terms

are computed by second order central difference scheme. Projection method, a two-stage fractional step scheme, is employed to couple pressure and velocity field effectively using the PETSc toolkit (Krylov subspace method; BCGSL, Stabilized version of BiConjuate Gradient Squared method). In order to solve the system of the discretized governing equations, between three and five inner iterations are run in each time step and solutions are considered to be converged once the error for velocities, pressure, and level-set reach to less than 10^{-5} , 10^{-8} , and 10^{-5} respectively.

2.2 MATHEMATICAL MODEL OF THE CODE

The information of the mathematical background of the computation code CFDShip-Iowa v4.0 is summarized and provided in this section. All variables and properties are non-dimensionalized with the reference velocity U_0 which is ship speed and length between fore and aft perpendiculars L_{PP} , water density ρ and viscosity μ .

The Reynolds number and Froude number are defined as in equation (1) and (2).

$$Re = \frac{\rho U_0 L_{PP}}{\mu} \quad (1)$$

$$Fr = \frac{U_0}{\sqrt{gL_{PP}}} \quad (2)$$

2.2.1 Governing Equations

In Cartesian coordinates, the incompressible continuity and momentum equations in non-dimensional form with the body-force term are expressed as in equation (3) and (4) with piezometric pressure described in equation (5).

$$\frac{\partial U_i}{\partial X_i} = 0 \quad (3)$$

$$\frac{\partial U_i}{\partial t} + U_j \frac{\partial U_i}{\partial X_j} = -\frac{\partial \hat{p}}{\partial X_i} + \frac{1}{Re} \frac{\partial^2 U_i}{\partial X_j \partial X_j} - \frac{\partial}{\partial X_j} \overline{U'_i U'_j} + f_{b_i} \quad (4)$$

$$\hat{p} = \frac{p - p_a}{(\rho U_0^2)} + \frac{Z}{Fr^2} \quad (5)$$

The Reynolds stresses in equation (4) which is related to the mean rate of strain through an isotropic eddy viscosity is calculated as:

$$-\overline{U'_i U'_j} = \nu_t \left[\frac{\partial U_i}{\partial X_j} + \frac{\partial U_j}{\partial X_i} \right] - \frac{2}{3} \delta_{ij} k \quad (6)$$

For the computation, the governing equations are transformed by applying the chain rule for partial derivatives from the physical domain in Cartesian coordinates (X, Y, Z, t) into the computational domain in non-orthogonal curvilinear coordinates (ξ, η, ζ, τ) where all cells are cubes with unit sides. A partial transformation is used in which only the independent variables are transformed, leaving the velocity components in the base coordinates.

2.2.2 Turbulence Model

A number of turbulence models are available such as $\kappa - \varepsilon$ / $\kappa - \omega$ based isotropic or anisotropic RANS and DES approach with near-wall and wall functions. In this study, Menter's blended $\kappa - \varepsilon$ / $\kappa - \omega$ without wall function is used (Menter et al., 1994). It is also known as the shear-stress transport (SST) model which effectively blend the robust and accurate formulation of the $\kappa - \omega$ model in the near-wall region with the free-stream independence of the $\kappa - \varepsilon$ model in the far field. To achieve this, the $\kappa - \varepsilon$ model is converted into a $\kappa - \omega$ formulation. The SST $\kappa - \omega$ model is similar to the standard $\kappa - \omega$ model, but includes some refinements in which the standard $\kappa - \omega$

model and the transformed $\kappa - \varepsilon$ model are both multiplied by a blending function and both models are added together. The blending function is designed to be one in the near-wall region, which activates the standard $\kappa - \omega$ model, and zero away from the surface, which activates the transformed $\kappa - \varepsilon$ model. It incorporates a damped cross-diffusion derivative term in the ω equation. The definition of the turbulent viscosity is modified to account for the transport of the turbulent shear stress. And the modeling constants are different. These features make the SST $\kappa - \omega$ model more accurate and reliable for a wider class of flows (e.g., adverse pressure gradient flows, airfoils, etc.) than the standard $\kappa - \omega$ model. Other modifications include the addition of a cross-diffusion term in the ω equation and a blending function to ensure that the model equations behave appropriately in both the near-wall and far-field zones.

$$\frac{\partial k}{\partial t} + \bar{U}_l \frac{\partial k}{\partial X_l} = -\bar{U}'_l \bar{U}'_m \frac{\partial \bar{U}_l}{\partial X_m} + \frac{\partial}{\partial X_l} \left\{ \frac{v_t}{\sigma_k} \frac{\partial k}{\partial X_m} + \frac{1}{Re} \frac{\partial k}{\partial X_m} \right\} - \beta^* k \omega \quad (7)$$

$$\begin{aligned} \frac{\partial \omega}{\partial t} + \bar{U}_l \frac{\partial \omega}{\partial X_l} &= \frac{\partial}{\partial X_m} \left\{ \frac{v_t}{\sigma_\omega} \frac{\partial \omega}{\partial X_m} + \frac{1}{Re} \frac{\partial \omega}{\partial X_m} \right\} - \alpha \frac{\omega}{k} \bar{U}'_l \bar{U}'_m \frac{\partial \bar{u}_l}{\partial X_m} - \beta k \omega^2 \\ &\quad + 2(1 - F_1) \sigma_{\omega^2} \frac{1}{\omega} \frac{\partial k}{\partial X_m} \frac{\partial \omega}{\partial X_l} \end{aligned} \quad (8)$$

Where,

$$v_t = \frac{a_1 k}{\max(a_1 \omega, \Omega F_2)}, \quad a_1 = 0.31, \quad \Omega = |\Omega_{lm}|, \quad |\Omega_{lm}| = \sqrt{2\Omega_{lm}\Omega_{lm}}, \quad \Omega_{lm} = \frac{1}{2} \left(\frac{\partial U_l}{\partial X_m} + \frac{\partial U_m}{\partial X_l} \right)$$

$$F_2 = \tanh(\arg_2^2), \quad \arg_2 = \max \left[2 \frac{\sqrt{k}}{0.09 \omega \delta}, \frac{500 \nu}{y^2 \omega} \right]$$

$$F_1 = \tanh(\arg_1^4), \quad \arg_1 = \min \left[\max \left[2 \frac{\sqrt{k}}{0.09 \omega \delta}, \frac{500 \nu}{\delta^2 \omega} \right], \frac{4 \rho \sigma_{\omega^2} k}{CD_{k\omega} \delta^2} \right]$$

$$CD_{k\omega} = \max \left[2 \rho \sigma_{\omega^2} \frac{1}{\omega} \frac{\partial k}{\partial X_m} \frac{\partial \omega}{\partial X_l}, 10^{-20} \right]$$

Where δ is the distance to the wall, $\beta^* = 0.09$, $\sigma_{\omega^2} = 0.856$, $\kappa = 0.41$ are model constants and $\sigma_k, \sigma_\omega, \beta$ and $\alpha = \frac{\beta}{\beta^*} - \sigma_\omega \kappa^2 / \sqrt{\beta^*}$ are calculated by weight averaging

the $\kappa - \omega$ and standard $\kappa - \varepsilon$ models with the weight coefficient F_1 which is 1 near wall region and 0 at outer place.

2.2.3 Single Phase Level-Set Free Surface Model

The free surface detection is computed by the level set method. The standard level set method for incompressible free surface viscous flows is originated about 1995 which is well known as two-phase level set method in which the solution is obtained in both fluids. In this computation, only one phase will be taken into account to get the solution known as single phase level set method. The 3D level set function ϕ is defined in the whole domain with its value related to the distance to the interface. The sign of ϕ is arbitrarily set to negative in air and positive in water and the iso-surface $\phi = 0$ represents the free surface. Since the free surface is considered a material interface, then the equation for the level set function is:

$$\frac{\partial \phi}{\partial t} + \frac{\partial(\phi U_i)}{\partial X_i} = 0 \quad (9)$$

And from the level set function, the normal can be computed as

$$\mathbf{n} = -\frac{\nabla \phi}{|\nabla \phi|} \quad (10)$$

The boundary conditions for the velocity at the interface is

$$\nabla \mathbf{U} \cdot \mathbf{n} = 0 \quad (11)$$

In addition, a zero normal gradient for both k and ω is used at the free surface as

$$\nabla k \cdot \mathbf{n} = 0 \quad (12)$$

$$\nabla \omega \cdot \mathbf{n} = 0 \quad (13)$$

Details of the level set method used in CFDShip-Iowa including re-initialization

techniques are described in Carrica et al. (2007a).

2.3 GRIDS, COMPUTATIONAL DOMAIN AND BOUNDARY CONDITIONS

2.3.1 S60 Case

The whole computational grid domain is constructed by totally five blocks for without-hub computation namely boundary layer (BL) grids (Port & Starboard), propeller grid, wake refinement grid and background grid, and by seven blocks for with-hub condition with additional hub grids (Port & Starboard). As no wall-function is utilized, the BL grids are generated around the solid hull surface with the non-dimensional minimum grid spacing 1×10^{-6} from the surface. The propeller grid is also generated by adequate grid size in order to compute the propeller force. The wake refinement grid is added near the stern region that covers the propeller in order to capture the complicated wake field injected from the rotating propeller. The background grid is the outermost part of the domain with the finer grid spacing near the free surface with non-dimensional minimum grid spacing in order of 10^{-5} . In the with-hub case, the hub grids for port and starboard side are generated with the non-dimensional minimum grid spacing 1×10^{-6} which overlaps on the ship hull solid surface. H-O grid typology is applied in the mesh generation with H-type for wake refinement and background grid while O-type is for BL grids and propeller grid.

Meshes are generated by PointWise Grid generation software and the necessary boundary conditions are set in the software. The overset interpolation information between each block is determined by SUGGAR which is originally developed by IIHR,

the University of Iowa. Some solid surface interpolation points will be cut-out by SUGGAR and those that will not be in the computation are defined as ghost cells and Panel Weights Programs are used to determine the ghost cell size for the whole domain. Totally, 6.8 million grids is used for without-hub condition and 8.3 million is used for the with-hub case which are listed in Table 2-1 and 2-2 with grid topology.

Table 2-1 Details of Grids for without-hub condition (S60)

	Topology	I	J	K	Total
Boundary Layer Starboard	O	154	50	143	1101100
Boundary Layer Port	O	154	50	143	1101100
Propeller block	O	25	63	101	159075
Wake Refinement	H	201	51	51	522801
Background	H	216	121	151	3946536

Table 2-2 Details of Grids for with-hub condition (S60)

	Topology	I	J	K	Total
Boundary Layer Starboard	O	170	51	137	1187790
Boundary Layer Port	O	170	51	137	1187790
Hub Starboard	O	31	49	25	37975
Hub Port	O	31	49	25	37975
Propeller block	O	27	115	101	313605
Wake Refinement	H	251	81	81	1646811
Background	H	216	121	151	3946536

The whole grid domain with boundary conditions is shown in Figure 2-1. The free

surface is located at $Z = 0$ and $0.22L_{PP}$ height above the free surface with $1L_{PP}$ depth is generated. The boundary layer grid is shown to the starboard part only for the clear vision of the hull solid surface where no-slip boundary condition is applied. The information for the detailed boundary condition is listed in Table 2-3.

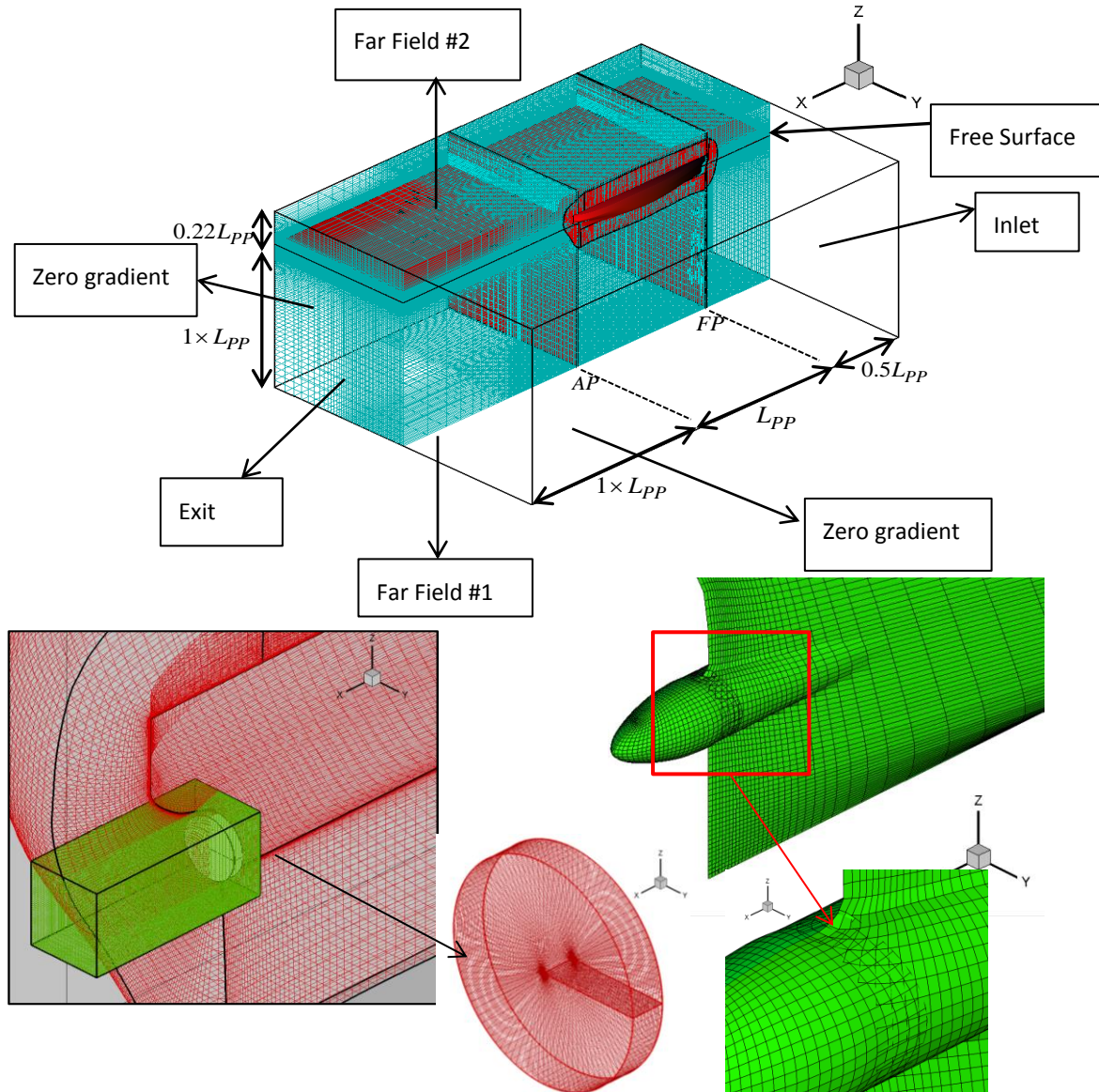


Figure 2-1 Overset grid system, seven blocks (five for without-hub case): boundary layer, hub, propeller, background and refinement and overset view in the stern part

Table 2-3 Boundary conditions for both S60 and KVLCC2 models

	Inlet	Exit	Bottom	Top	Sides
p	$\frac{\partial p}{\partial n} = 0$	$\frac{\partial p}{\partial n} = 0$	$p = 0$	$\frac{\partial p}{\partial n} = 0$	$\frac{\partial p}{\partial n} = 0$
k	$k_{fs} = \frac{9 \times 10^{-3}}{Re}$	$\frac{\partial k}{\partial n} = 0$			
ω	$\omega_{fs} = 9$	$\frac{\partial \omega}{\partial n} = 0$			
U	$U = U_0$	$\frac{\partial^2 U}{\partial n^2} = 0$	$\frac{\partial U}{\partial n} = 0$	$\frac{\partial U}{\partial n} = 0$	$\frac{\partial U}{\partial n} = 0$
V	$V = 0$	$\frac{\partial^2 V}{\partial n^2} = 0$	$\frac{\partial V}{\partial n} = 0$	$\frac{\partial V}{\partial n} = 0$	$\frac{\partial V}{\partial n} = 0$
W	$W = 0$	$\frac{\partial^2 W}{\partial n^2} = 0$	$\frac{\partial W}{\partial n} = 0$	$\frac{\partial W}{\partial n} = 0$	$\frac{\partial W}{\partial n} = 0$

2.3.2 KVLCC2 Case

In KVLCC2 case, the two cases are studied; one is propeller-hull interaction and the other is propeller-hull-rudder interaction. In the first case, the wake field produced from the propeller model is easy to observe and the analyses can be carried out easily. As the rudder part is not included, the capability of the proposed propeller model can be studied clearly. The latter case includes the rudder to understand the effect of rudder on the propeller and hull. The total computational domain is comprised of 9 blocks for without-rudder case (12.9 million grids) and 11 blocks for with-rudder case (13.1 million grids). All the grid generation process and overset method is similar to S60 case and the total grid sizes for both cases are listed in Table 2-5 and 2-6. The computational domain and geometry of the ship without-rudder and with-rudder cases are shown in Figure 2-2. The boundary conditions are similar to S60 case and Table 2-3 can be referred.

Table 2-4 KVLCC2 geometry data

Main Particulars	Full Scale	Osaka University Model
Scale	1	1/100
L_{PP} (m)	320.0	3.2
L_{wl} (m)	325.5	3.255
B_{wl} (m)	58	0.58
Depth(m)	30	0.3
Draft (m)	20.8	0.208 (for even keel)
Displacement (m ³)	312622	0.313
S w/o rudder (m ²)	27194	2.71
CB	0.8098	0.8098
CM	0.9980	0.9980
LCB (%), fwd +	3.48	3.48
Propeller		
Type	FP	FP
No. of blades	4	4
Diameter (m)	9.86	0.0986
P/D (0.7R)	0.721	0.721
Ae/A0	0.431	0.431
Rotation	Right hand	Right hand
Hub ratio	0.155	0.155
Rudder		
Type	Horn	Horn
S of rudder (m ²)	273.3	0.02733
Lat. Area (m ²)	136.7	0.01367
Service speed		
U_0 (m/s, full scale: kn)	15.5	0.795
Fr	0.142	0.142

In this case, as the stern part is as not simple as S60, finer port and starboard blocks known as the tail blocks are generated just for the stern part and they overlap the original boundary layer blocks. Then, the hub blocks overlap the tail blocks and

SUGGAR is used to determine the overset structure and Panel weight program is used for ghost cells. The general dimension of KVLCC2 used in this thesis is listed in Table 2-4.

Table 2-5 Details of Grids for without-rudder condition (KVLCC2)

	Topology	I	J	K	Total
Boundary Layer Starboard	O	154	50	144	1108800
Boundary Layer Port	O	154	50	144	1108800
Tail part (Starboard)	O	55	50	40	110000
Tail part (Port)	O	55	50	40	110000
Hub (Starboard)	O	55	50	40	110000
Hub (Port)	O	55	50	40	110000
Propeller block	O	27	126	101	343602
Wake Refinement	H	281	141	151	5982771
Background	H	216	121	151	3946536

Table 2-6 Details of Grids for with-rudder condition (KVLCC2)

	Topology	I	J	K	Total
Boundary Layer Starboard	O	154	50	144	1108800
Boundary Layer Port	O	154	50	144	1108800
Tail part Starboard	O	55	50	40	110000
Tail part Port	O	55	50	40	110000
Hub Starboard	O	55	50	40	110000
Hub Port	O	55	50	40	110000
Propeller block	O	27	126	101	343602
Rudder Starboard	O	44	43	70	132440
Rudder Port	O	44	43	70	132440
Wake Refinement	H	281	141	151	5982771
Background	H	216	121	151	3946536

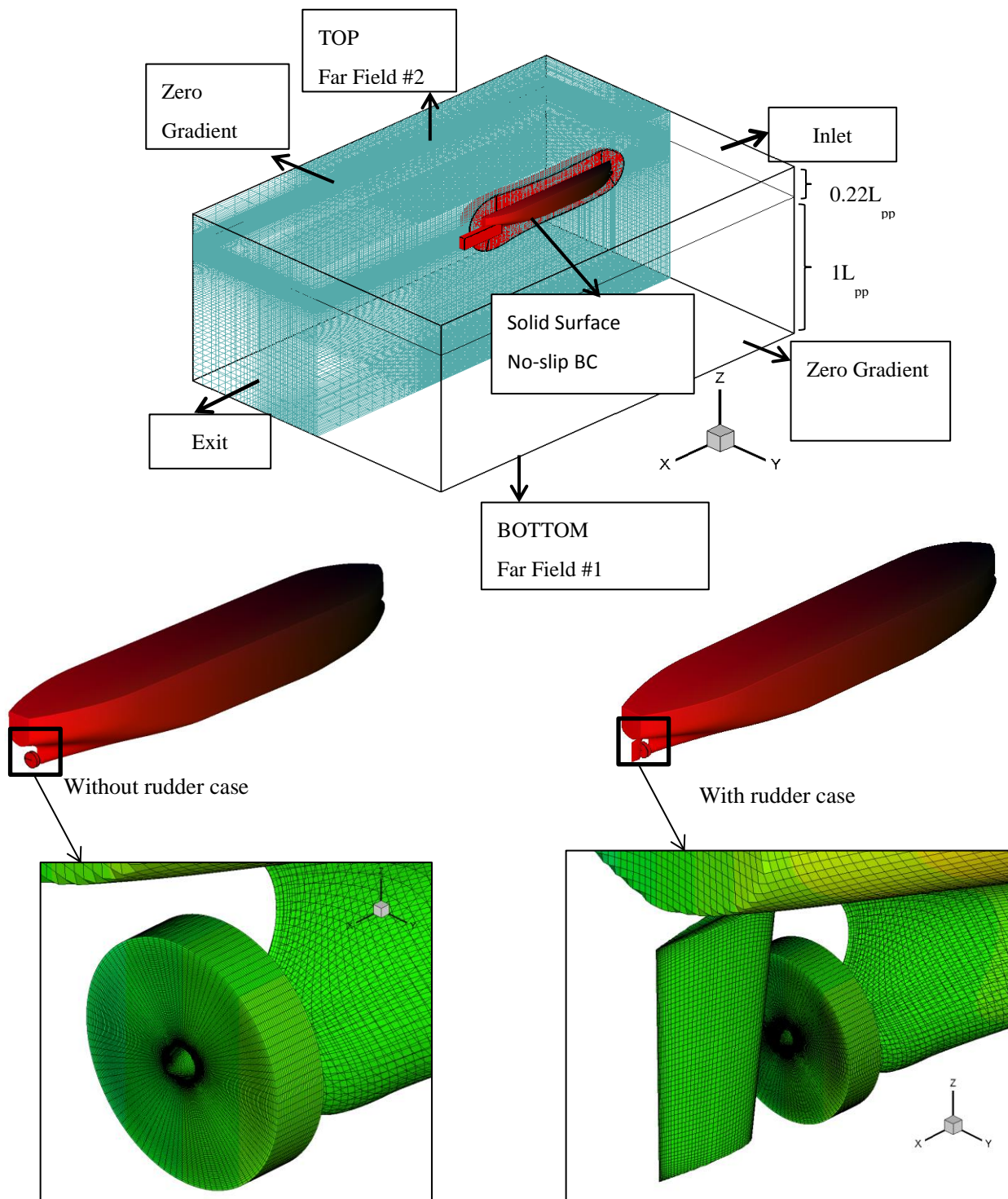


Figure 2-2 Overset grid systems, nine blocks for without-rudder case and eleven blocks for with-rudder case: boundary layer, stern, hub, propeller, rudder, wake refinement and background and overset view in the stern part

2.4 PROPELLER MODEL

The propeller model is treated as the infinite-bladed model with a simplified quasi-steady blade element theory with consideration of time averaged propeller induced velocity field. The propeller blade has airfoil shape and twist distribution and the blade element uses these geometrical properties to determine the forces exerted by a propeller on the flow field. The propeller blade which has radius R is split radially into each piece forming airfoil control volume with the radial distance r from the center of the propeller.

The blade element theory for thrust and torque calculation for one blade element is illustrated in Figure 2-3. The drag and lift forces are computed on each segment and the time averaged body force components can be calculated by equation (28) approximately at any point for $R < r < R_B$ where R_B is hub radius. The integration of forces inside the propeller radius gives thrust (T) and torque (Q) of the propeller. When the propeller is rotating, with effective inflow velocity, there will be an induced velocity by the propeller and the RANS computation with body force distribution can give the resultant axial velocity component and the propeller model is running based on this value.

Based on Figure 2-3, the resultant velocity V_R is calculated as in equation (14) and hydrodynamic pitch angle φ is computed in equation (15) using the axial and tangential velocity components. Here, U_t is the total axial velocity component at the propeller plane. V_θ is the tangential velocity with the induced velocity which can be calculated as in equation (16) by the cross-flow components V and W at the propeller plane. The formulations in equation (17) and (18) show geometrical computation on the grid at propeller plane with respect to the shaft center position and terms with

subscript SC refer to positions at shaft center.

$$V_R = \sqrt{U_t^2 + (2\pi n_{rev}r - V_\theta)^2} \quad (14)$$

$$\varphi = \tan^{-1} \left(\frac{U_t}{2\pi n_{rev}r - V_\theta} \right) \quad (15)$$

$$V_\theta = V \sin \theta - W \cos \theta \quad (16)$$

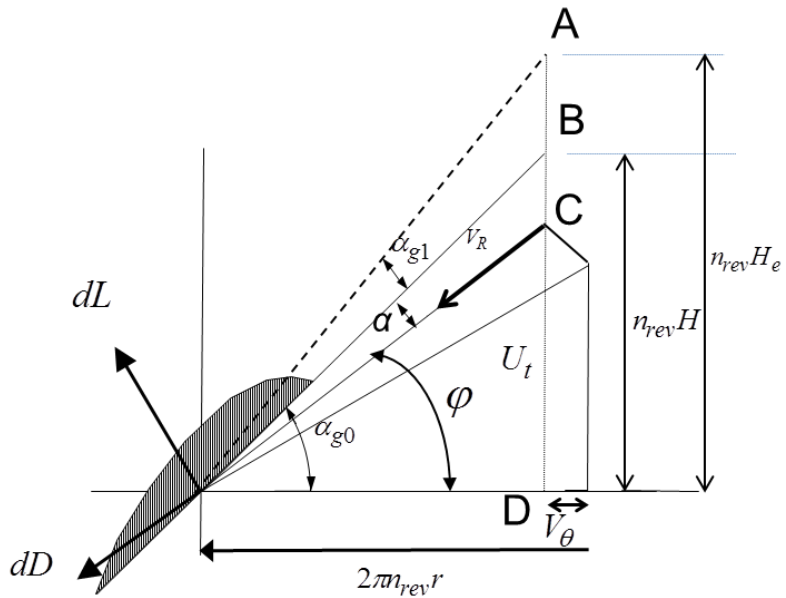


Figure 2-3 Blade element theory

$$\cos \theta = \frac{(Y - Y_{SC})}{\sqrt{(Y - Y_{SC})^2 + (Z - Z_{SC})^2}} = \frac{(Y - Y_{SC})}{r} \quad (17)$$

$$\sin \theta = \frac{(Z - Z_{SC})}{\sqrt{(Y - Y_{SC})^2 + (Z - Z_{SC})^2}} = \frac{(Z - Z_{SC})}{r} \quad (18)$$

The drag coefficient C_D is assumed to be 0.02 which has been determined by several experiments and the lift coefficient is calculated by equation (19) as a function of inflow angle of attack. The formulation for inflow angle of attack is shown in equation (20~22) based on the geometric pitch (H) and effective pitch ($H_e=1.08H$ for S60 and $H_e=1.1H$ for KVLCC2) of the propeller. The variable k_1 in equation (19) represents the

blade-to-blade interaction effect calculating based on the maximum chord length of the blade which is at $r = 0.7R$ of the blade for the current propeller and is computed by equation (22).

$$C_l = 2\pi k_1 \sin(\alpha_0 + \alpha_{g1}) \quad (19)$$

$$\alpha_0 = \tan^{-1}\left(\frac{H}{2\pi r}\right) - \varphi \quad (20)$$

$$\alpha_{g1} = \tan^{-1}\left(\frac{H_e}{2\pi r}\right) - \tan^{-1}\left(\frac{H}{2\pi r}\right) \quad (21)$$

$$k_1 = 1.07 - 1.05\left(\frac{c_{0.7R}}{R}\right) + 0.375\left(\frac{c_{0.7R}}{R}\right)^2 \quad (22)$$

The segmental lift and drag forces are calculated by equation (23~24) where, c is the chord length of each segment. The blade has a suction surface and pressure surface, and the vortices shed from the blade tips into the slip stream on the induced velocity field that can create multiple helical structures in the wake and play a major role in the induced velocity distribution. For this deficiency, Prandtl's tip correction factor is used in the computation as shown in equation (25).

$$dL = 0.5C_l V_R^2 c \quad (23)$$

$$dD = 0.5C_D V_R^2 c \quad (24)$$

$$F = \frac{2}{\pi} \cos^{-1} e^{-f_{tip}}, \quad f_{tip} = \frac{N}{2} \frac{R-r}{r \sin \varphi} \quad (25)$$

$$dT = (dL \cos \varphi - dD \sin \varphi)F \quad (26)$$

$$dQ = (dL \sin \varphi + dD \cos \varphi)rF \quad (27)$$

$$f_{bX} = \frac{dT}{\Delta X} \frac{N}{2\pi r}, \quad f_{b\theta} = \frac{dQ}{\Delta X} \frac{N}{2\pi r^2} \quad (28)$$

$$f_{bY} = f_{b\theta} \sin \theta, \quad f_{bZ} = -f_{b\theta} \cos \theta \quad (29)$$

$$T = \int_{r_B}^R \int_0^{2\pi} f_{bX} r \Delta X d\theta dr, \quad Q = \int_{r_B}^R \int_0^{2\pi} f_{b\theta} r^2 \Delta X d\theta dr \quad (30)$$

$$K_T = \frac{T}{n_{rev}^2 Dia^4}, \quad K_Q = \frac{Q}{n_{rev}^2 Dia^5} \quad (31)$$

The segmental thrust and torque forces are computed as in equation (26) to (27) with tip loss correction factor. The axial and tangential body-force terms are calculated as in equation (28) in time-averaged manner which is implemented in equation (4), where ΔX represents grid spacing at the propeller plane in X_1 direction and Y and Z components of body-force are computed in equation (29) (Yokota et. al., 2013). The integration of the segmental thrust and torque forces from the hub to the tip gives the total thrust and torque forces (equation (30)) and the corresponding thrust and torque coefficients are calculated in equation (31).

It is obvious that the proposed method is very simple and a comparison can be made with another simple infinite propeller model, which is proposed by Kyushu University and the model is known as Yamazaki model. In Yamazaki model, the effective wake at the propeller plane is extracted from the inflow total velocity components of the CFD solution and these are used to calculate the thrust and torque distribution by potential flow theory. This current method is an equivalent method in viscous flow code with Kyushu University method but no extraction step is required for effective wake. Within this theory, the inflow velocity components, including induced velocity effect by time averaged infinite bladed vortex system shed by propeller blade, to the propeller are determined by CFD code and thrust and torque distributions are calculated by blade element theory with some modification similar to the potential flow theory. Therefore, the potential flow code is not required in the proposed method which is simplifier.

The propeller for S60 is fixed pitch and KVLCC2 propeller is variable pitch. The detailed dimensions for S60 propeller is described in section 2.5 and for KVLCC2 propeller is listed in Table 2-4. For the computation, all variables are non-dimensionalized and the chord length distribution for S60 is shown in Figure 2-4

and the pitch and chord length distribution for KVLCC2 is shown in Figure2-5 and 2-6.

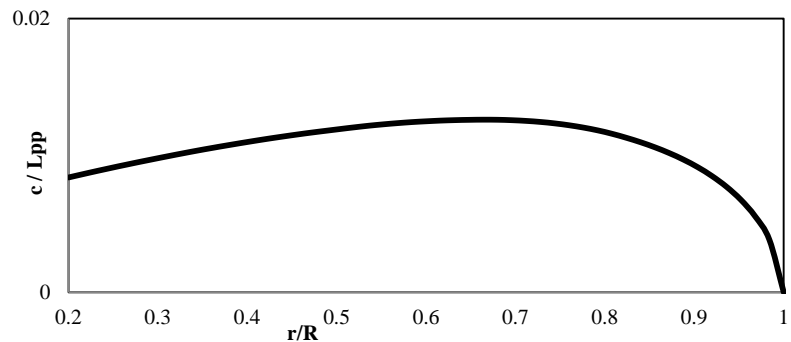


Figure 2-4 Chord length distribution of S60 propeller

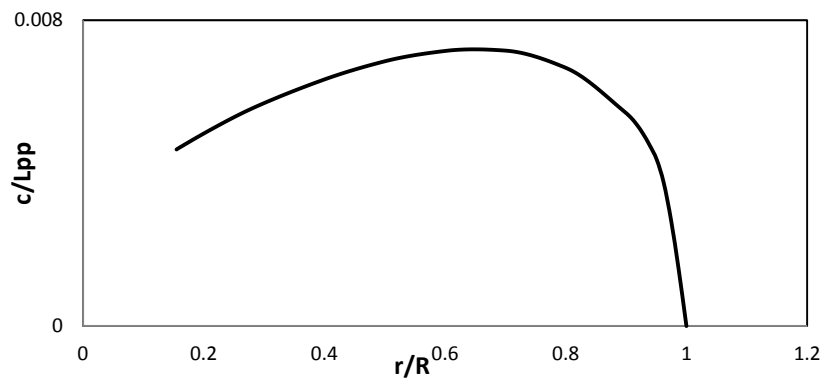


Figure 2-5 Chord length distribution of KVLCC2 propeller

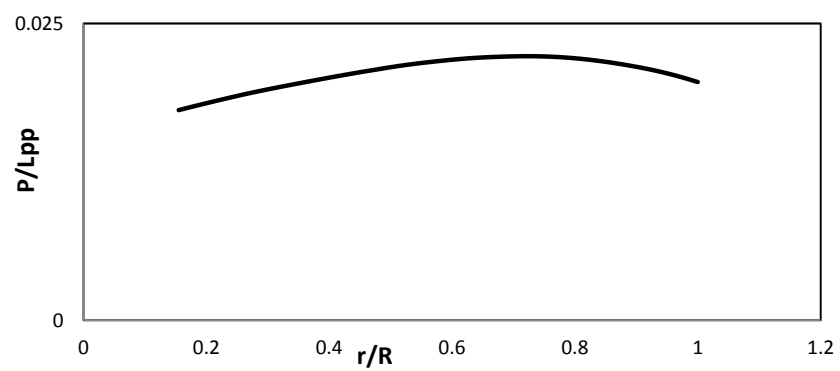


Figure 2-6 Pitch distribution of KVLCC2 propeller

2.5 EFD BACKGROUNDS

2.5.1 S60 case

Extensive experimental data is obtained for the Series 60 model at the Osaka University towing tank as a cooperative study with the Iowa Institute of Hydraulic Research (Toda et al., 1990). The tank is 100 m long, 7.8 m wide and 4.35 m deep. It is equipped with a drive carriage and also equipped with plunger-type wave maker generating regular and irregular waves up to 500 mm wave height and wave length of 0.5 to 15m. The wave absorber is a small fixed gridiron beach at the basin's end, with movable beaches along its sides.

Mean-velocity and pressure field measurements are made for both the without and with-propeller conditions for Series 60 $C_B = 0.6$ hull form at numerous stations upstream and downstream of the propeller and in the near wake region. Surface pressure distributions and wave profiles are measured for both conditions. Resistance and self-propulsion tests are also conducted.

Two 4 m long models are constructed for the experiments: a wooden model is used for the mean-velocity and pressure field measurements; and a fiber-reinforced-plexiglass model with pressure taps is used for the surface-pressure measurements. In order to induce turbulent flow, a row of trapezoidal studs with 1.5 mm height, 1.5 mm length and 2 mm front width and 1 mm back width, are fitted at 10 mm spacing on both models at $X=0.05$. Single- and duplex-balance rod-deflection type dynamometers are used for the resistance and propeller open-water tests, respectively. These same dynamometers are also used for the self-propulsion tests. The propeller is a conventional stock

propeller designed based on the MAU methodical series (Tsuchida et al., 1958) with 145.64 mm diameter, constant pitch, zero skew, 6 degree rake, 5 blades, and MAU n=25 sections. For each experiment, the voltage output from the transducers is sampled, digitized, recorded, and analyzed by a microcomputer on the carriage. The measurements are monitored with a multi-pen recorder during each carriage run. Froude number for S60 is 0.16 and Reynolds number is 3.96×10^6 .

2.5.2 KVLCC2 Case

The PIV measurement for KVLCC2 ship model with 1/100 scale ratio has been tested in the same towing tank in 2013 in different seasons (one in summer and one in winter). The principle dimensions of the model and the propeller is listed in Table 2-4. The ship model, the coordinate system applied, the propeller models (right handed and left handed models) and the rudder model is shown in Figure 2-7. The experimental set up of PIV system is shown in Figure 2-8. The experiments include the open water propeller test, the bare hull test, the test without propeller and the test with different kinds of rudder ranging from normal rudder to the ones fitted with energy saving devices. The Reynolds number for KVLCC2 is 2.05×10^6 .

The open water propeller test is carried out first. There are two propeller models for right handed and left handed and both of which are designed with same pitch distribution. Both propellers are tested and the open water characteristic curve for each is evaluated separately. The two results are almost similar which are illustrated in Figure A-2 of Appendix. The ship model is tested for bare hull resistance test and the self-propulsion point is found out and PIV measurement is carried out for the nominal

wake field. For the wake field measurement, the propeller revolution rate is set at 16.5 rps which is for self-propulsion point and 11.1 rps for ship point. As the laser measurement can be read only one side of the ship, the experiments are carried out with left-handed propeller and right handed propeller separately and the port side data and starboard data are superposed finally. The tests are carried out without rudder and with different rudder types including normal rudder to special types fitted with energy saving devices. The purpose is not only to understand the flow field of the tanker but also the advantages of the energy saving devices. The experimental results until the test with normal-rudder will be using in this thesis for the comparison with the computation.



Figure 2-7 KVLCC2 ship model, propeller models (left handed and right handed), rudder model and coordinate system

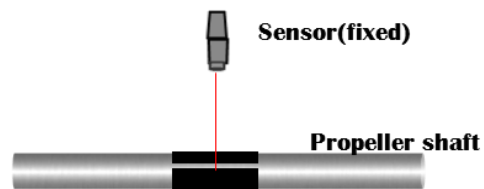
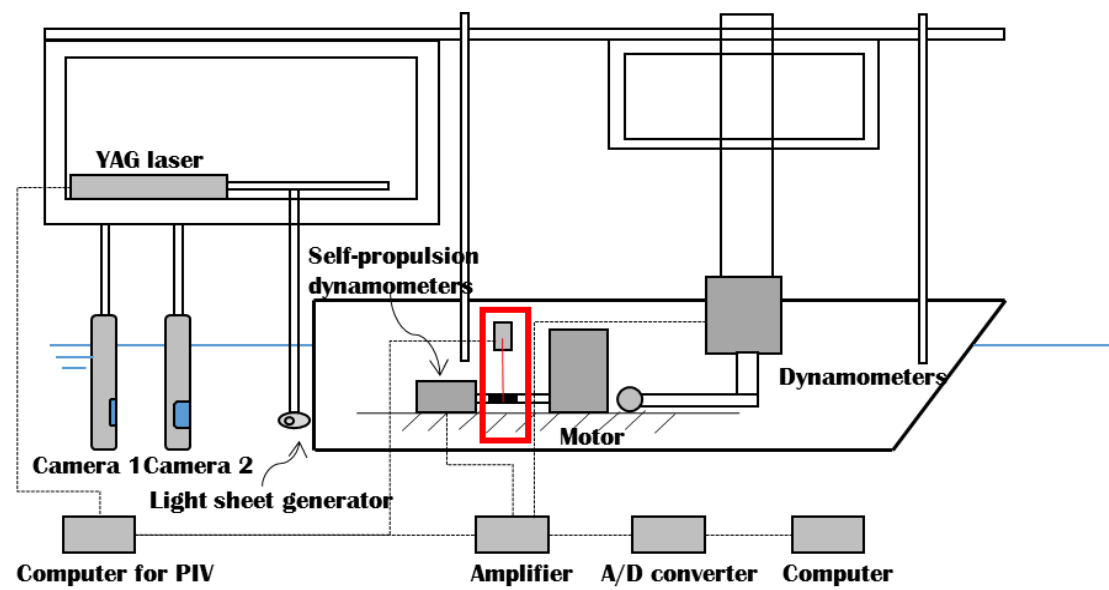


Figure 2-8 Experimental set up for PIV measurement

CHAPTER 3: WITHOUT-HUB COMPUTATION OF S60

3.1 BARE HULL COMPUTATION

Most CFD users deal the computations with special care not to get a numerical divergence. Coupling the propeller performance program together with the ship hull in the undisturbed fluid domain might lead to numerical divergence as the propeller has to work harder in nominal wake. The computation conditions have been explained in Chapter 2. In this study, the bare hull case and the propeller computation will be carried out separately. So, before coupling of the propeller model to the RANS code, the computation of the bare hull will be carried out first until the residuals approach 3rd or 4th order accuracy. The nominal wake flow and the bare hull resistance can be analyzed from the converged solution which could be validated with the experimental data (Toda et al., 1990).

The flow field in the stern region especially at the propeller section is analyzed thoroughly and compared with the experiment to ensure the RANS result is good enough. The essential feature of the mean flow is required to predict with considerable accuracy, including the pressure, the boundary-layer thickness and the mean-velocity field at the stern. The computation is performed for many time steps to achieve the converged solution as it will be used as the initial flow field when the propeller model is turned on. The axial velocity contour of the computation at each section ($X=0.8, 0.9, 0.95, 0.975$) along the hull are shown in Figure 3-1 to Figure 3-4 with a comparison to the EFD flow field. The boundary layer shapes and thickness at these stations are much close to the experimental results so that the computation result is convinced in

the converged state.

The axial velocity contour and cross-flow vector comparison is made at the propeller plane ($X=0.9875$) to understand the nature of wake which is shown in Figure 3-5 and 3-6. The circle marks as the propeller disc with the small white circle for the hub section in EFD case and flow field inside is mainly observed. The wake field at the propeller section is essentially needed to analyze to confirm that the nominal wake inflow is reliable to work with a propeller model and is important as the thrust and torque of the propeller will be calculated based on it. Due to the lack of hub, the flow field near the center line of the computation is distinctly different to the one in EFD. In the cross-flow vector field, the experimental vector is a bit longer than that of CFD because the effect of stern tube displacement and modification of the cursor stern shape in EFD makes the cross-flow fields higher. So, the velocity fields and pressure coefficient at $X=0.9875$ is extracted for each vertical position ($Z = -0.01, -0.015, -0.02, -0.025, -0.03, -0.035, -0.04, -0.045, -0.05$) and the comparison is plotted with EFD data to see the difference which are shown in Figure 3-7 to Figure 3-10. Even though the axial velocity field and the pressure coefficients have good agreements with EFD, the cross-flow components (V and W) have deflected shapes near the center line ($Y=0$) which is consistent with the longer cross-flow vectors of EFD in Figure 3-6. However, in general sense, the computation gives much good agreements with EFD and the computation code is convinced to couple with propeller model.

Moreover, the surface-pressure distribution for bare-hull computation is extracted to make a comparison with the case of with-propeller conditions to observe the effect of propeller which will be explained in Section 3.2. The bare hull resistance which is the combination of the components of friction, pressure and wave is also computed and the

non-dimensional data shows 0.343×10^{-3} which is a bit lower than the experimental data, 0.344×10^{-3} and the comparison is illustrated in Figure 3-39. It shows the present computation shows good agreement with experimental data.

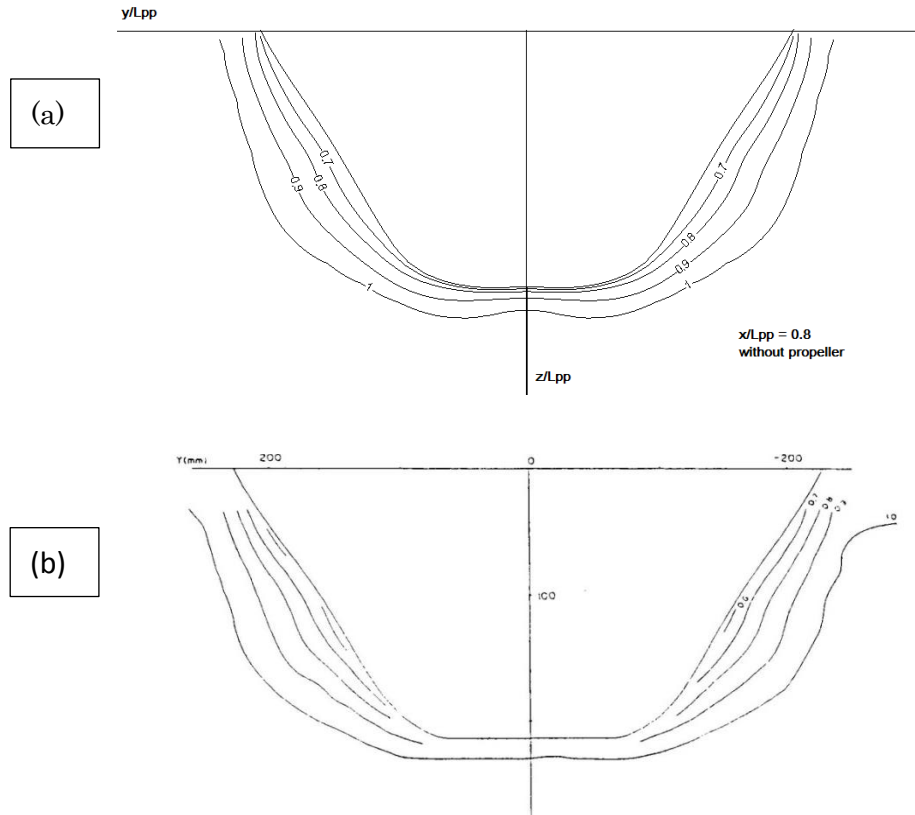
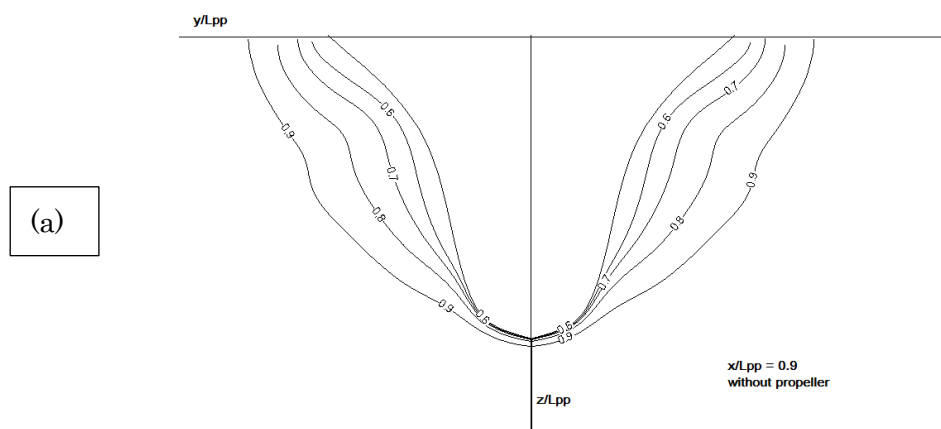


Figure 3-1 Comparison of axial velocity profiles between CFD (a) and EFD (b)
at $X=0.8$ section



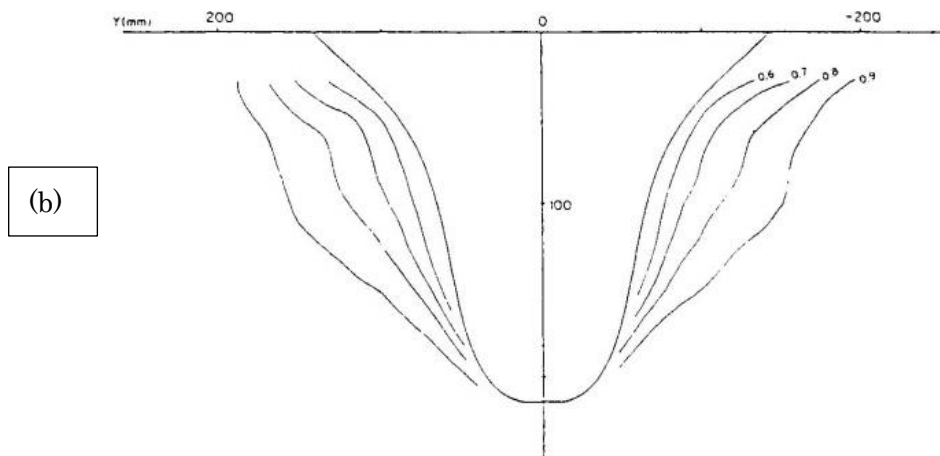


Figure 3-2 Comparison of axial velocity profiles between CFD (a) and EFD (b)
at $X=0.9$ section

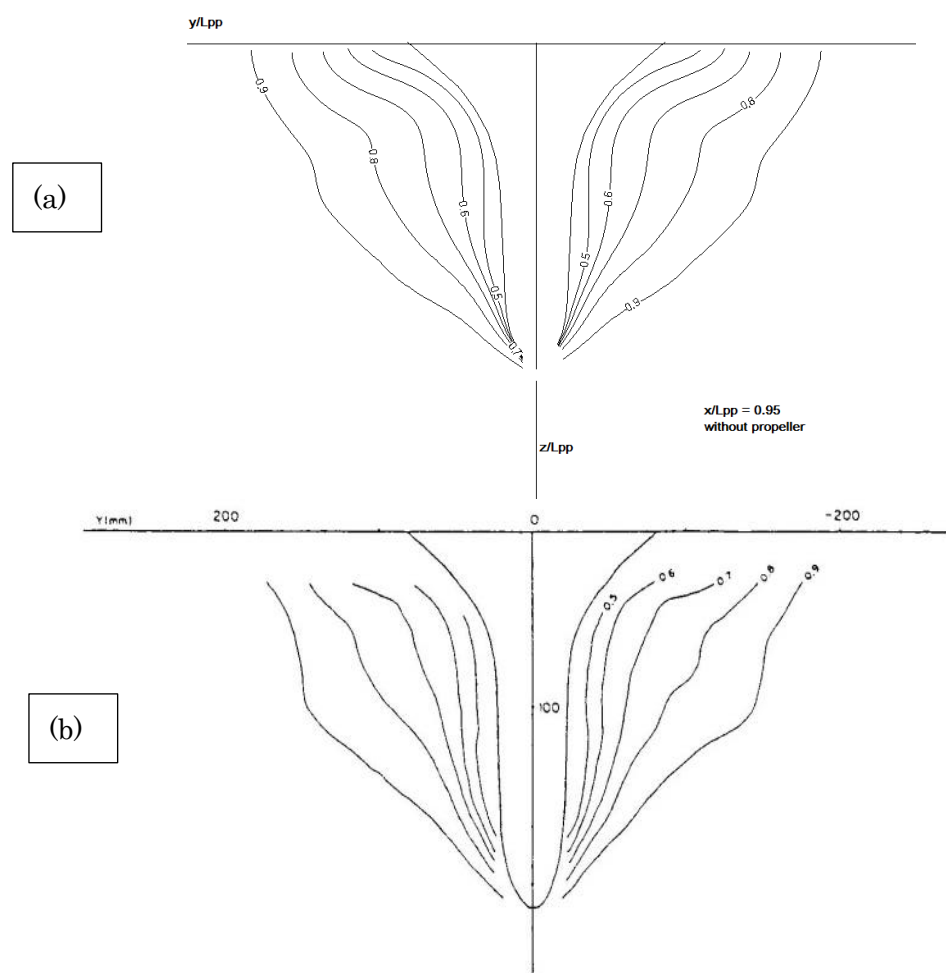


Figure 3-3 Comparison of axial velocity profiles between CFD (a) and EFD (b) at
 $X=0.95$ section

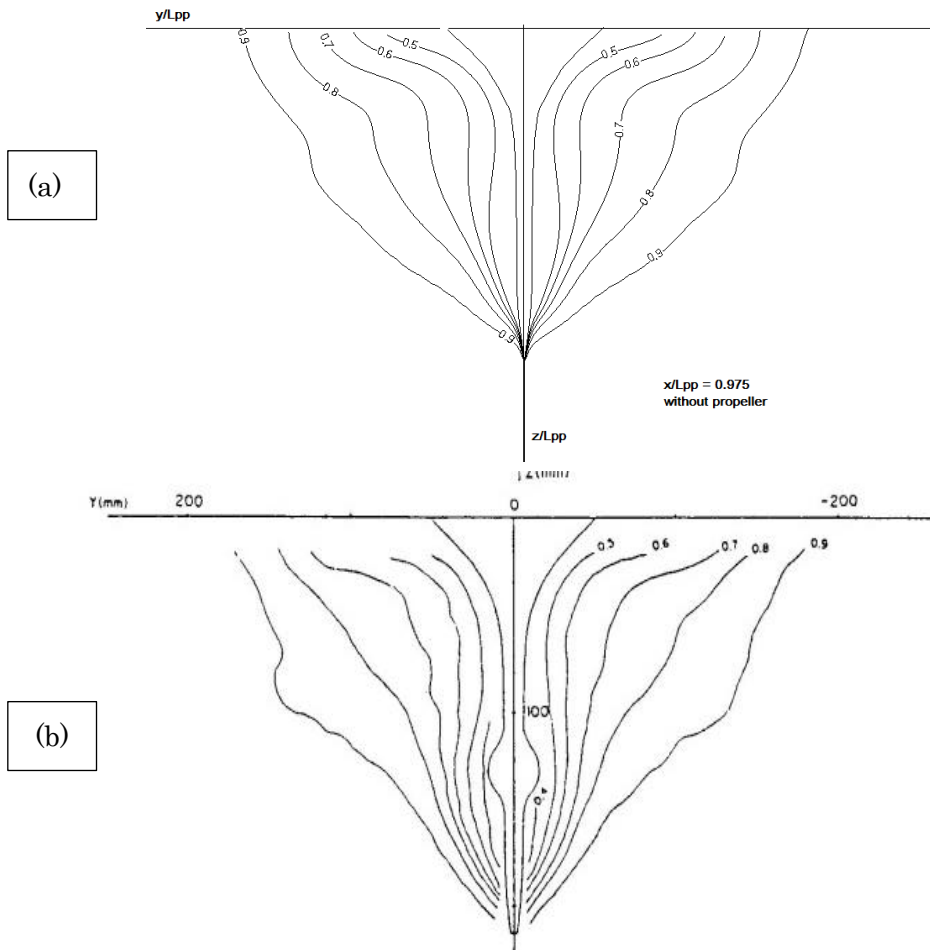
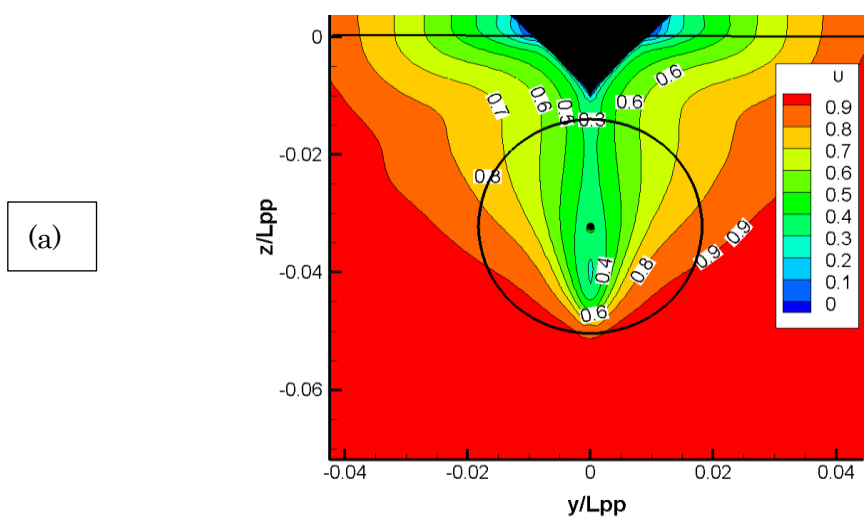


Figure 3-4 Comparison of axial velocity profiles between CFD (a) and EFD (b)
at $X=0.975$ section



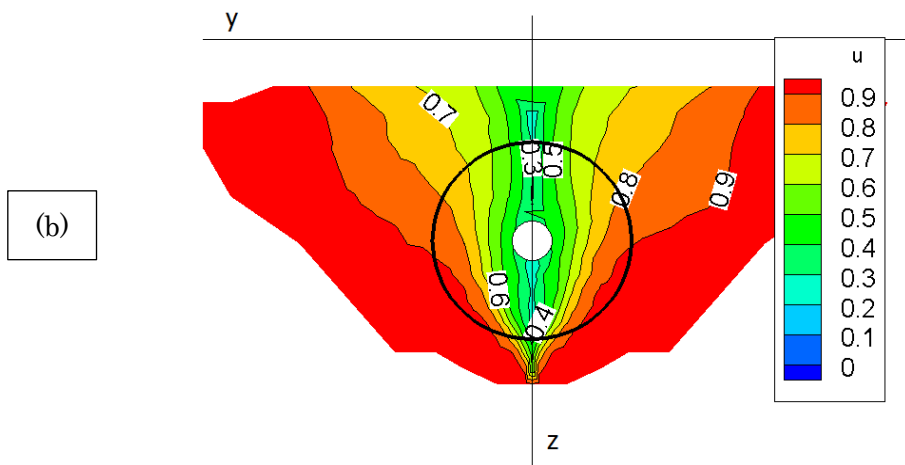


Figure 3-5 Comparison of axial velocity profiles between CFD (a) and EFD (b) at X=0.9875 section

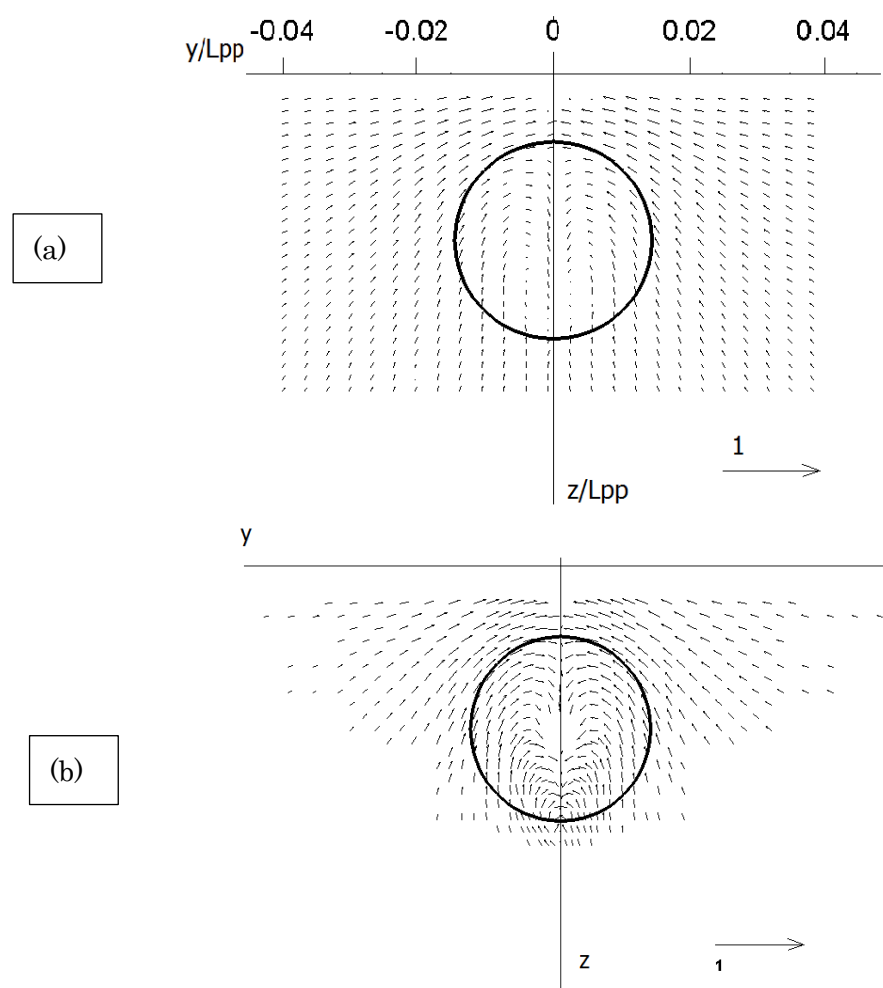


Figure 3-6 Comparison of cross-flow components between CFD (a) and EFD (b) at X=0.9875 section

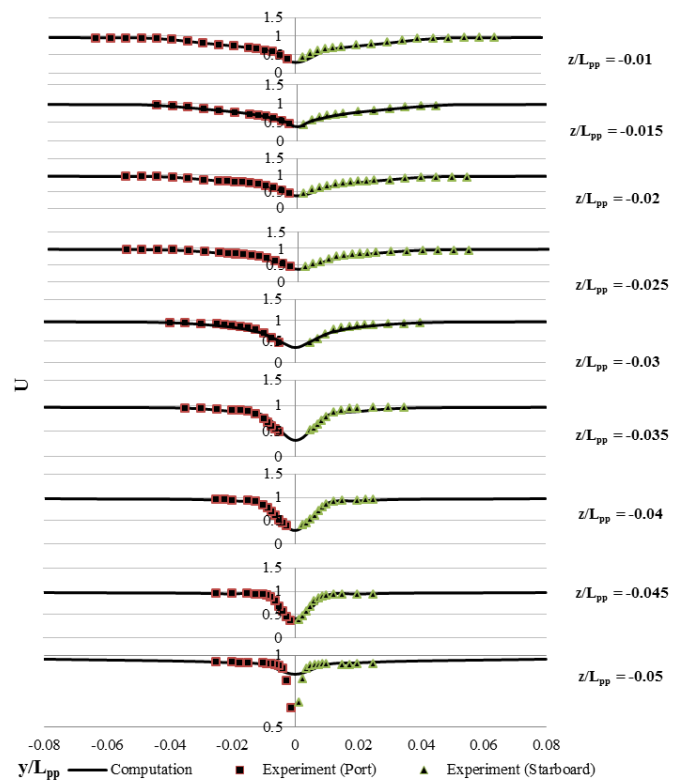


Figure 3-7 Comparison of U at $X=0.9875$ for each Z section

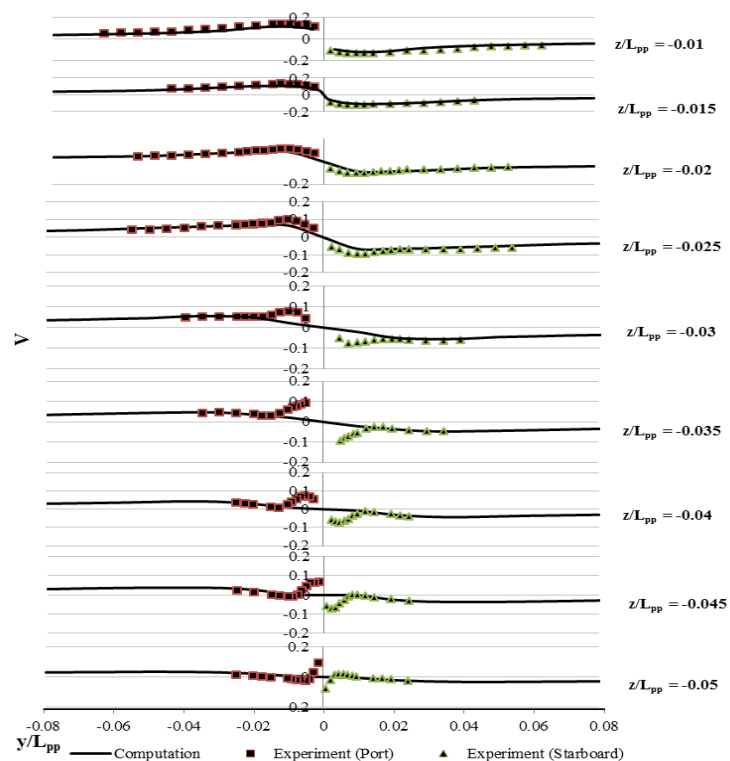


Figure 3-8 Comparison of V at $X=0.9875$ for each Z section

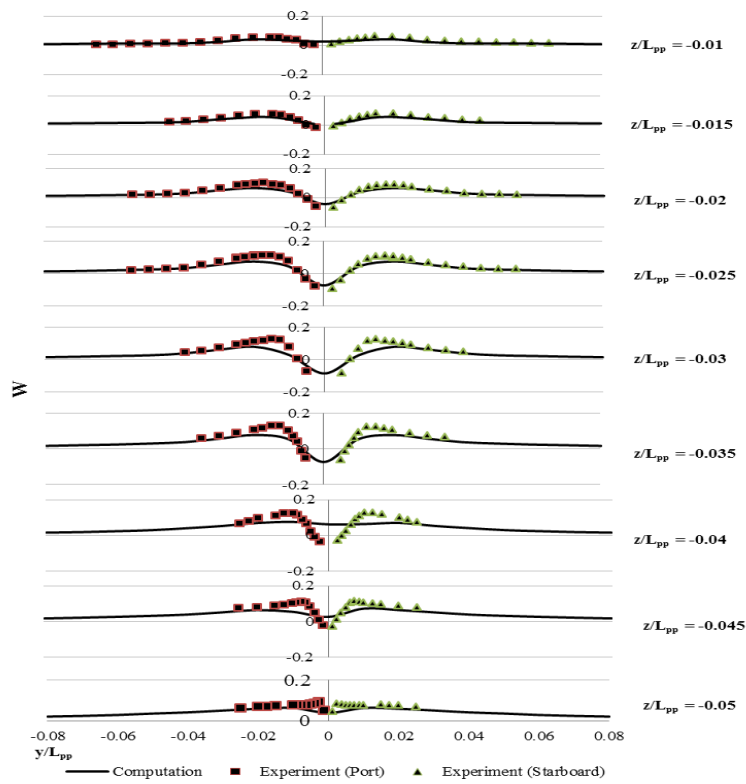


Figure 3-9 Comparison of W at $X=0.9875$ for each Z section

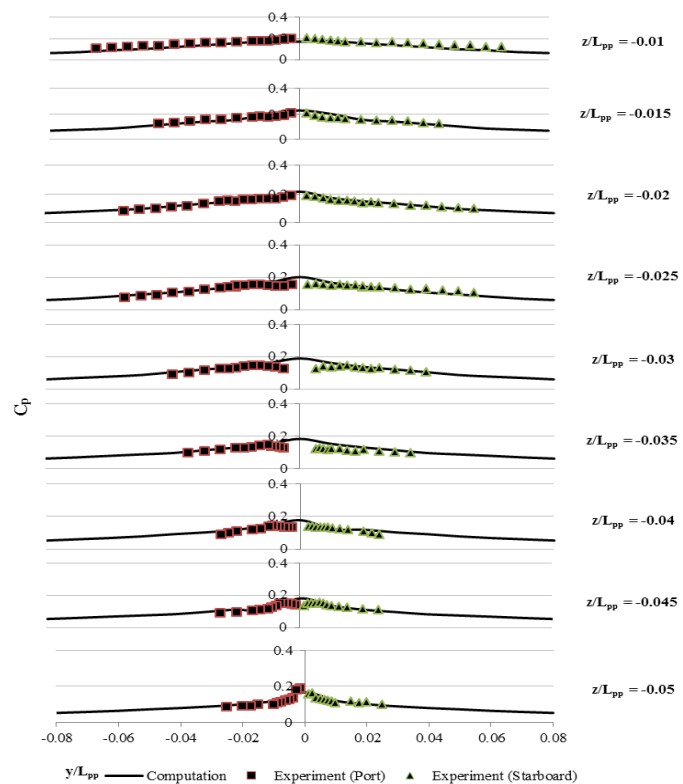


Figure 3-10 Comparison of C_p at $X=0.9875$ for each Z section

3.2 COUPLED COMPUTATION OF SHIP HULL AND PROPELLER

3.2.1 Convergence history and propulsive quantities

After the converged solution of the ship hull itself is obtained, it should be easy to couple with propeller performance program numerically. In order to prove the capability of the proposed propeller model, the primary concern is set to get good agreement with EFD data at its self-propulsion point. In that sense, the propeller revolution rate is fixed at model point $n_{rev}=7.8$ rps with advance coefficient of $J_s = 0.88$ throughout the computation. In the computation, the propeller program is called for every time step and there are 3 to 5 internal iterations in each time step. For the prevention of computational divergence, the amount of body-force which is treated in momentum equation is controlled by means of relaxation factor which is given by a small amount of 0.1 at the beginning and when the thrust and torque coefficient is converged in the specific time-steps, it is increased by an interval 0.1 and the procedure continues until the relaxation factor becomes 1. The computation at full relaxation factor is continued until the thrust and torque coefficients are converged.

The interactive procedure between the RANS solution and propeller-performance program is unnecessary for this model and the convergence history of the thrust and torque is shown in Figure 3-11. When the propeller starts working in the undisturbed wake, the thrust and torque coefficients are quite high and then decrease gradually as it runs more continuously because the propeller works harder in the undisturbed nominal wake field than in the effective wake. The final converged thrust and torque coefficients are 0.238 and 0.0416, both of which over-predict a little bit.

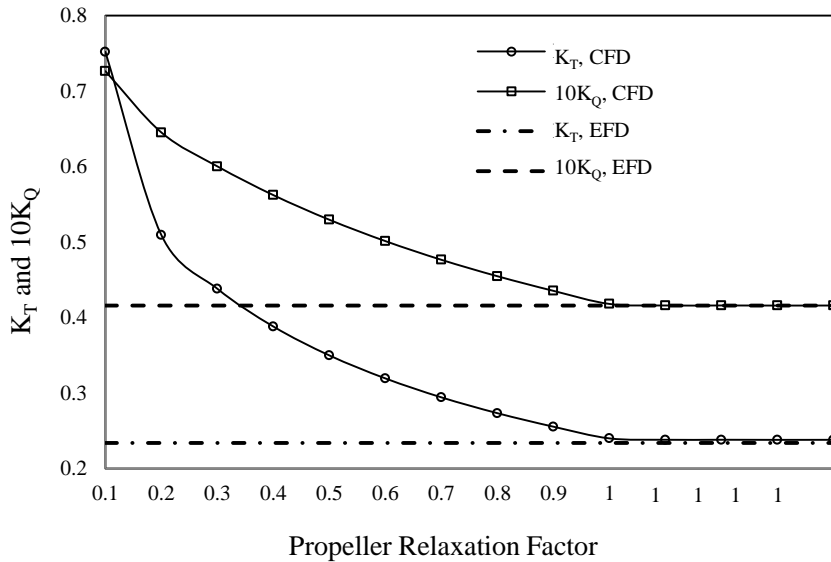


Figure 3-11 Convergence history of thrust and torque

Table 3-1 Comparison with EFD and other propeller models

Propeller Model	Thrust Coefficient	Torque Coefficient
	K_T	$10K_Q$
EFD	0.234	0.411
Vortex Lattice Method (Stern)	0.231	0.399
Kyushu University Model (Simonsen)	0.257	0.435
Blade Element Theory (Present work)	0.238	0.416

The results are compared with not only the EFD data as well as the other two models of the Vortex Lattice Model by Stern (et al., 1994) and Yamazaki model by Simonsen (et al., 2005) at the same advanced coefficient to understand the performance capability of the proposed propeller model more and these are summarized in Table 3-1. It shows that the closer results are obtained for both K_T and K_Q than Yamazaki Model. For comparing with Vortex Lattice Model, the similar results are obtained. In the present case and other two previous models, the original bare hull is used instead of the

modified hull with stern tube and the dummy hub, so more detailed discussion is not shown here.

The effective wake factor is calculated as in equation (32), where w is the wake fraction, on the basis of a thrust identity and J_a is defined as $J_a = \frac{U_a}{nDia}$ which is obtained from the open water characteristics curve of the same propeller by Togkoz (et al., 2013) and the propeller open water test result is shown in Figure A-1 of Appendix. J_s is corresponding to the thrust measured when the propeller is running behind the ship with the ship speed defined as $J_s = \frac{U_0}{nDia}$.

$$(1 - w) = \frac{J_a}{J_s} \quad (32)$$

The effective wake factor of the current work is 0.73 which is a little bit lower than EFD which shows 0.75 and this under-prediction would make sense as the thrust is over-predicted. More discussions on wake fraction and the thrust deduction factor which is related to the resistance forces and thrust are described in the section 3.2.3 based on various propeller loadings to understand the nature of the propeller better.

3.2.2 Analysis of wake field behind the rotating propeller

The flow field in the wake region which is the combination of potential, viscous and the wave wake is much complicated to manipulate and the propulsive performance of the propeller is much dependable on the nature of the wake. The propeller will not give right amount of thrust in the incorrect wake field and it is important to use a propeller model, which is located in the wake, to give right amount of suction on the upstream as well as right velocity distribution to the downstream for the rudder. The nominal wake field has been validated with experimental result and for proving the

proposed propeller model is working well, the wake field including the velocity components fields U, V, W as well as pressure coefficient C_p when the ship and propeller are coupled together is needed to analyze in detail not only on the upstream of the propeller but also on the downstream and should get close agreement with the experimental result.

In the current case, the propeller is located at $X = 0.9875$ and the main interest is the flow field of the upstream region at $X = 0.98125$ and the downstream region at $X = 1$. However, as the downstream region is mostly influenced by the effect of the presence of propeller, the flow nature at far downstream sections are chosen to study at $X=1.01875$ and $X=1.05$. The axial velocity contour and cross-flow vectors comparison with EFD is plotted for each location as shown in Figure 3-12 to Figure 3-21. In the upstream region, the velocity contour as well as the cross-flow vector shape shows good agreement with EFD though there is no stern tube in the computation. Analyzing the downstream part will give clear understanding of the flow nature of the propeller. At this section, the maximum axial velocity shape of 1.2 (Figure 3-14) is much close to the experimental result and it shows better result than that of Vortex Lattice Model by Stern (et al., 1994) and Yamazaki Model by Simonsen (et al., 2005) where the maximum axial velocity space is lower and narrower than EFD. The cross-flow vector field for the downstream part is also plotted and compared with EFD and the good agreement is achieved.

The difference of the axial velocity layouts between CFD and EFD become enlarged in the far downstream regions. In Figure 3-16 for the station $X=1.01875$, the highest velocity contour from the experiment is observed as 1.3 with large area wherein CFD gives maximum level 1.29 with very small area. In Figure 3-18 for the station $X=1.05$, the similar trend is observed. Moreover, in Figure 3-20, the gap becomes larger as the

CFD maximum level is only 1.26 while EFD becomes stronger. This dissipation behavior might be raised not only from the lack of hub and stern tube but also from the grid spacing. In the grid topology, the boundary layer grids are very fine near the hull body and exponentially expanded in the far region. The background grid is coarse and its purpose is to solve the free surface and to implement boundary conditions. So, for capturing the wake field coming out of the propeller injection, a wake refinement grid is inserted to adapt the fine propeller block and coarse background and boundary layer blocks. The refinement grid is very fine with minimum grid spacing 6.22×10^{-4} and the block ends at $X=1.10875$. In that place, the background and boundary layer blocks will have in the order of 10^{-3} grid spacing making the spacing difference 10 times between each block. Actually, this overset topology has been judged by the SUGGAR which automatically determines the coarse parts to cut it out as ghost cell. Although the overset part has passed the SUGGAR step successfully, logically, the interpolation between each block might have some problems. This fact should be taken into account on the dissipation of the computation in the far more downstream part in addition to the turbulence model or other numerical error.

It is not enough to judge by looking at the wake field trend pattern because it will be too general. So, the detailed flow field analyses are plotted comparatively with EFD data at section $X=0.98125$, 1.0 and 1.1, ranging $-0.05 \leq Z \leq -0.01$ shown in Figure 3-22 to Figure 3-33. The axial-velocity fields give good agreement generally but, for cross-flow velocity components in downstream, large cross-plane velocity components of EFD results are observed near the center plane due to the lack of strong hub vortex in CFD because the hub and boss cap are neglected i.e. V and W components are lower than experiment. In the experiment, when the propeller is rotating, the boss is also

rotating at the same revolution rate and this swirling effect will make V and W components stronger than the computation where the rotating hub is not included. The pressure field of the computation also gives lower near the center line because of the lack of the stern tube. This weak point will be re-computed by using the modified hull offset similar to experiment and the hub rotating with propeller in Chapter 4. However, apart from the weaker cross-flow components and corresponding pressure coefficient, the computation results are relatively reasonable with the better estimate than the other propeller models.

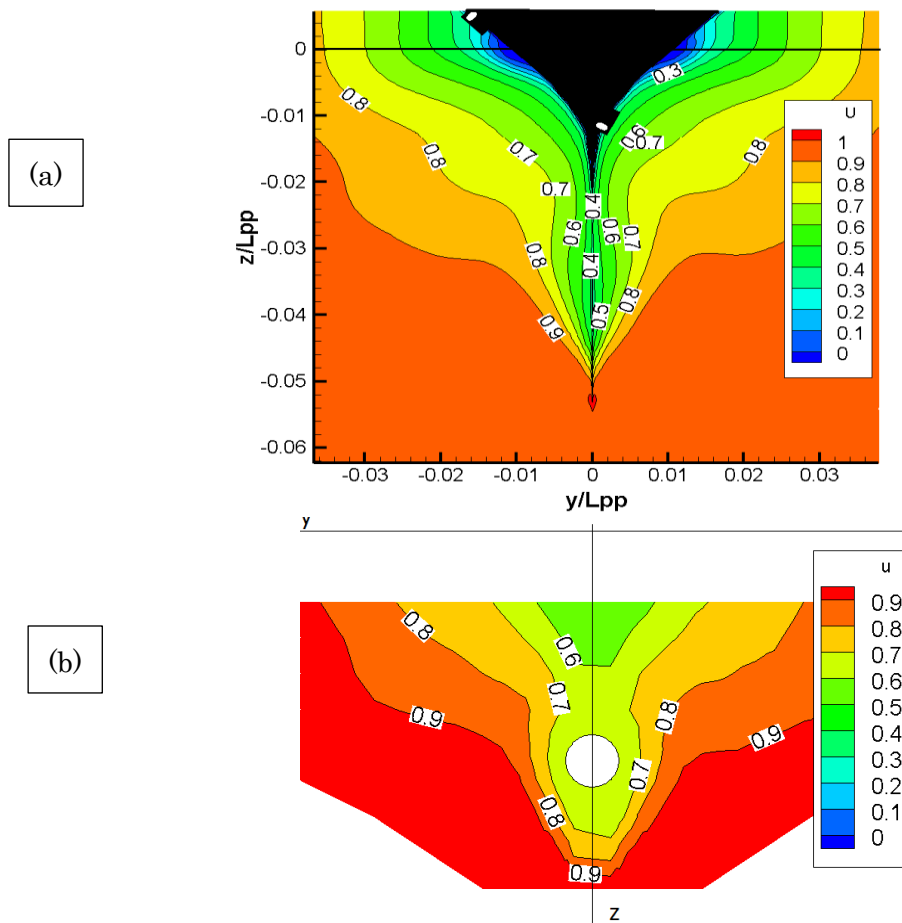


Figure 3-12 Comparison of axial velocity profiles between CFD (a) and EFD (b)
at $X=0.98125$ section

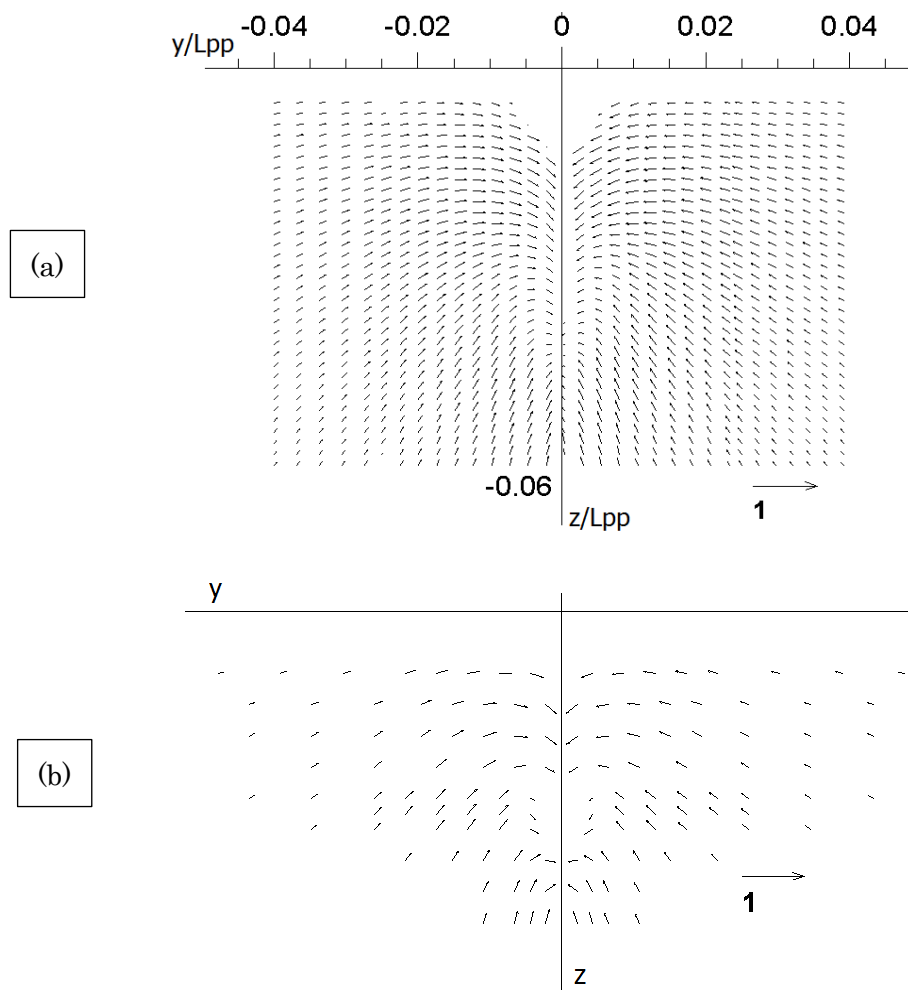
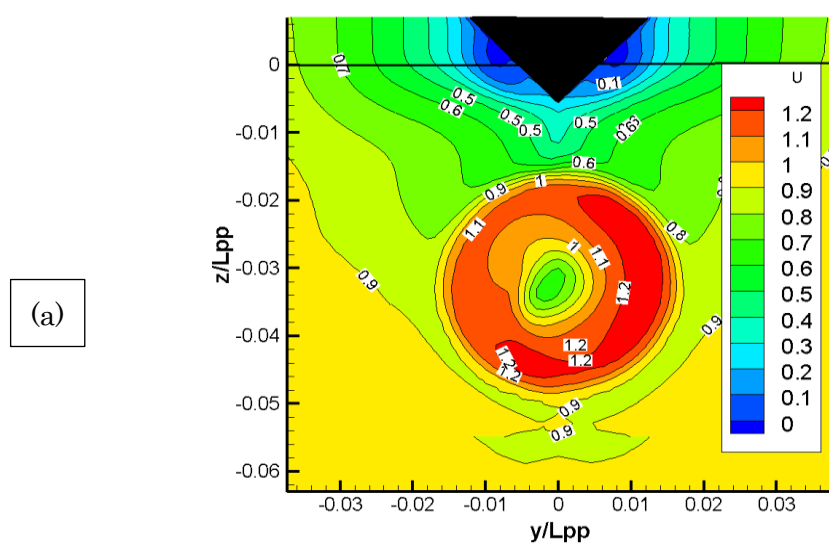


Figure 3-13 Comparison of cross-flow components between CFD (a) and EFD (b)
at $X=0.98125$ section



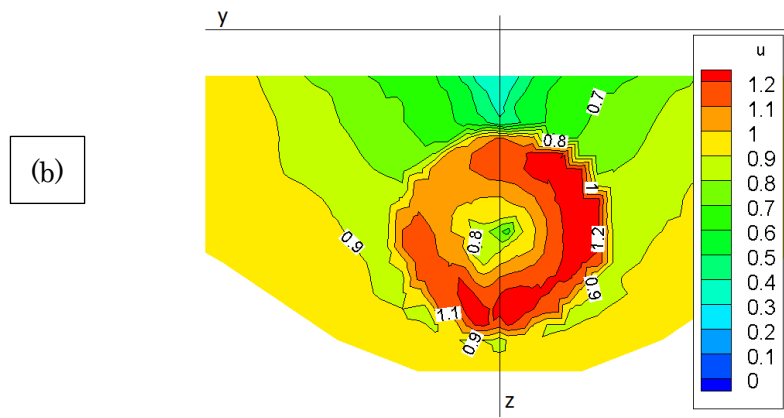


Figure 3-14 Comparison of axial velocity profiles between CFD (a) and EFD (b)
at X=1 section

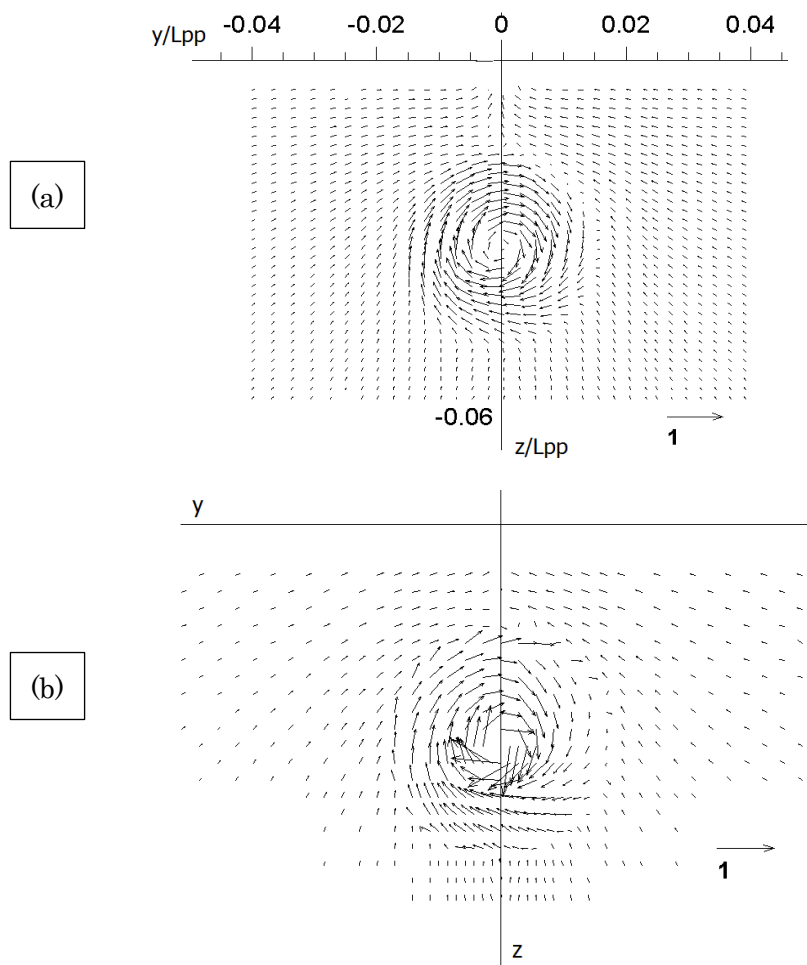


Figure 3-15 Comparison of cross-flow components between CFD (a) and EFD (b)
at X=1 section

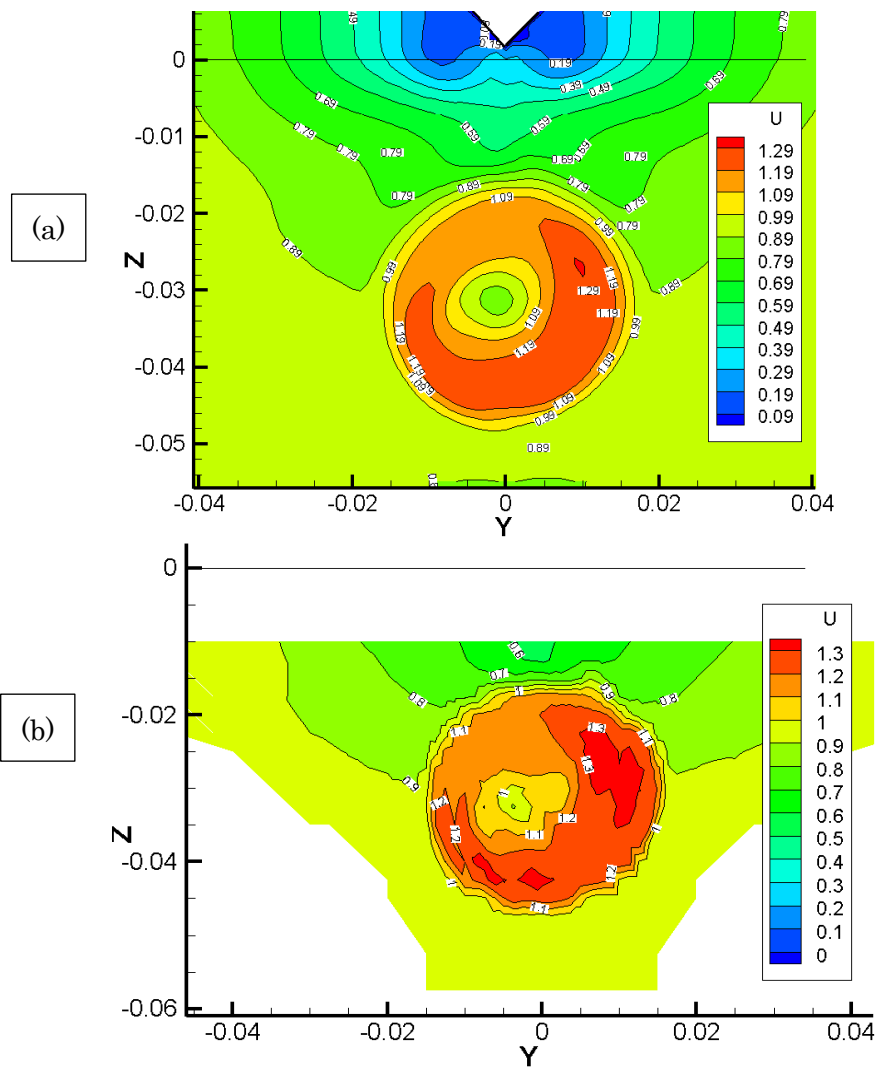
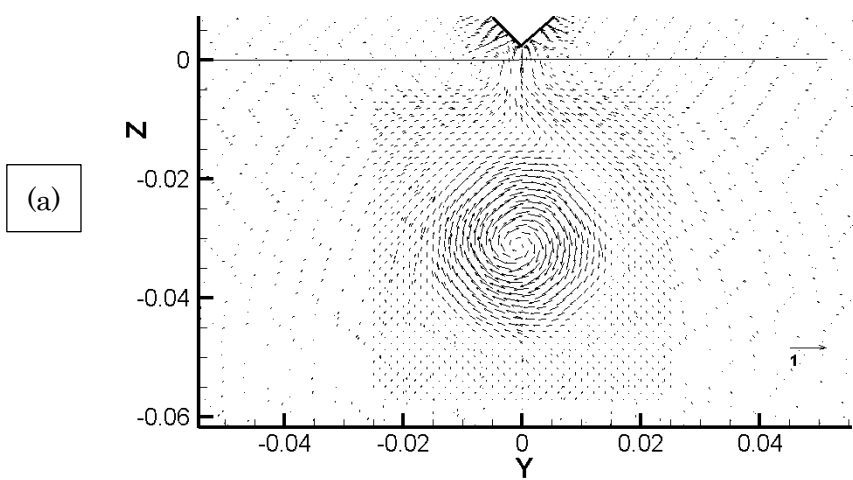


Figure 3-16 Comparison of axial velocity profiles between CFD (a) and EFD (b) at $X=1.01875$ section



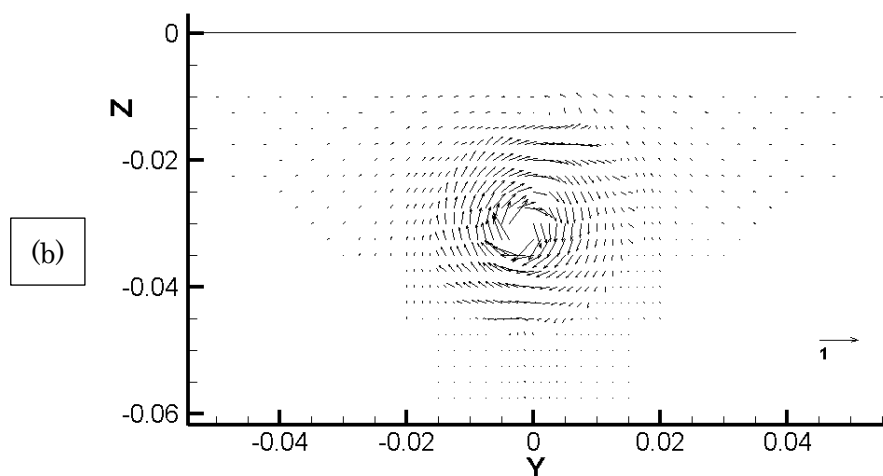


Figure 3-17 Comparison of cross-flow components between CFD (a) and EFD (b)
at $X=1.01875$ section

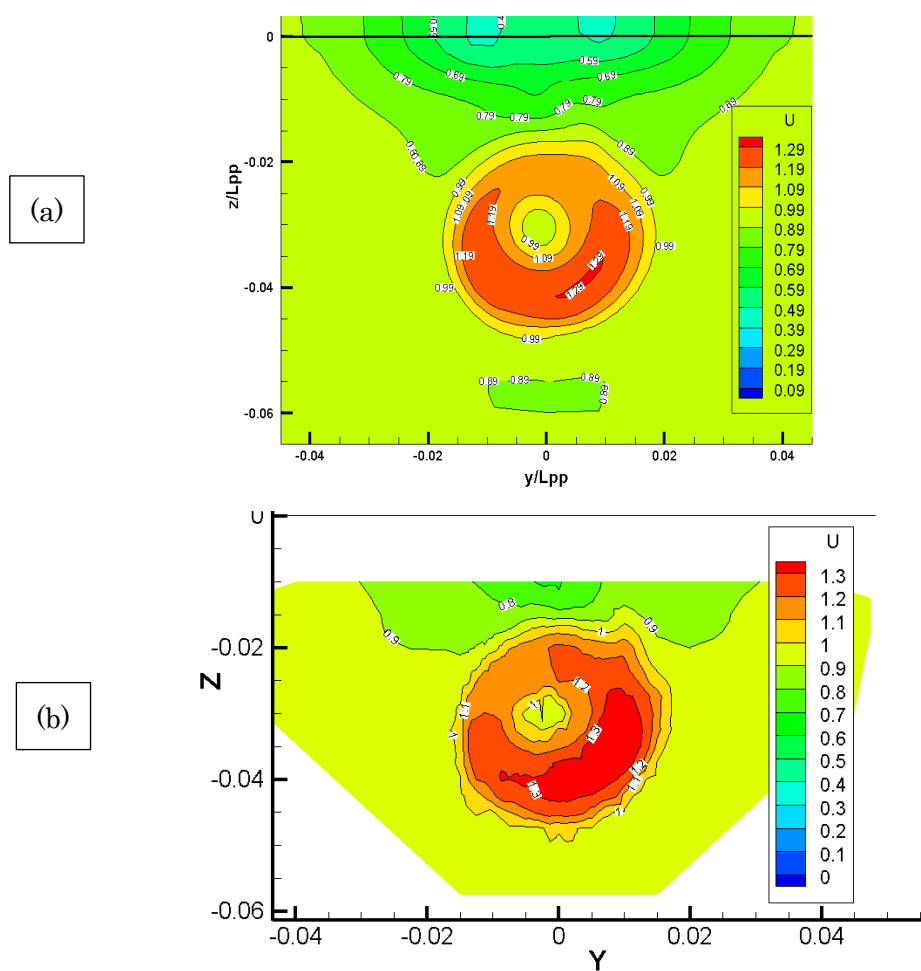


Figure 3-18 Comparison of axial velocity profiles between CFD (a) and EFD (b)
at $X=1.05$ section

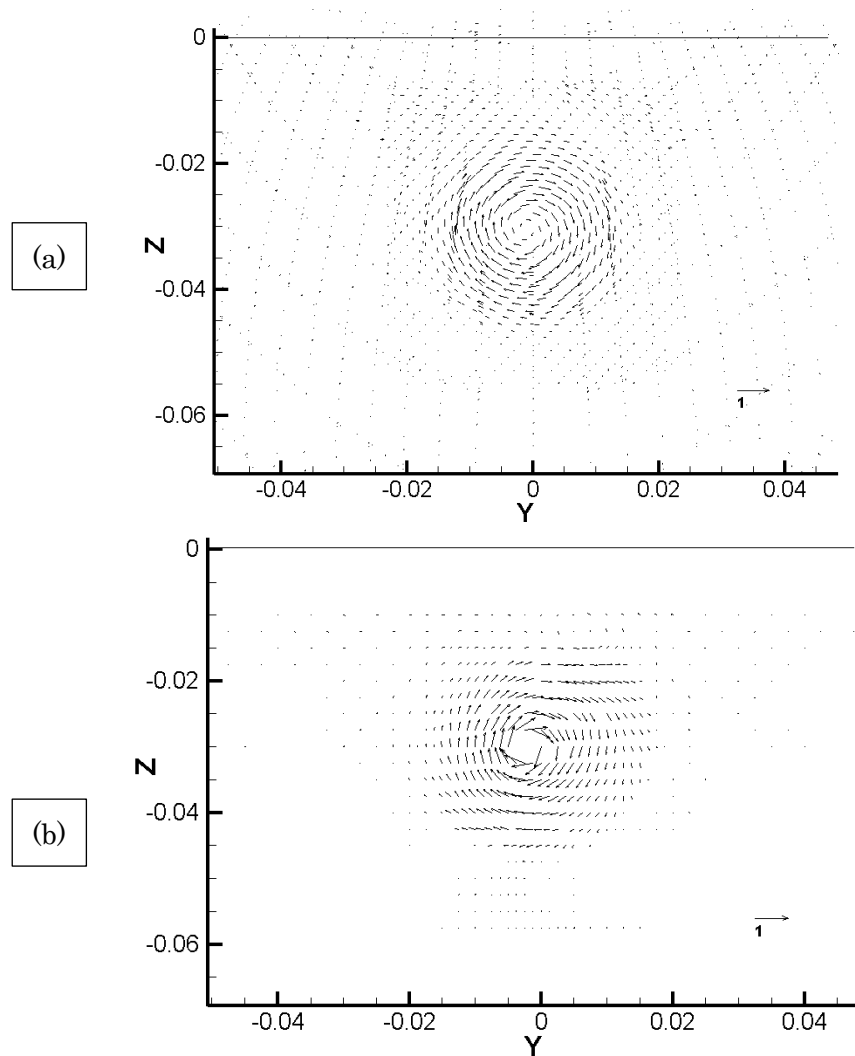
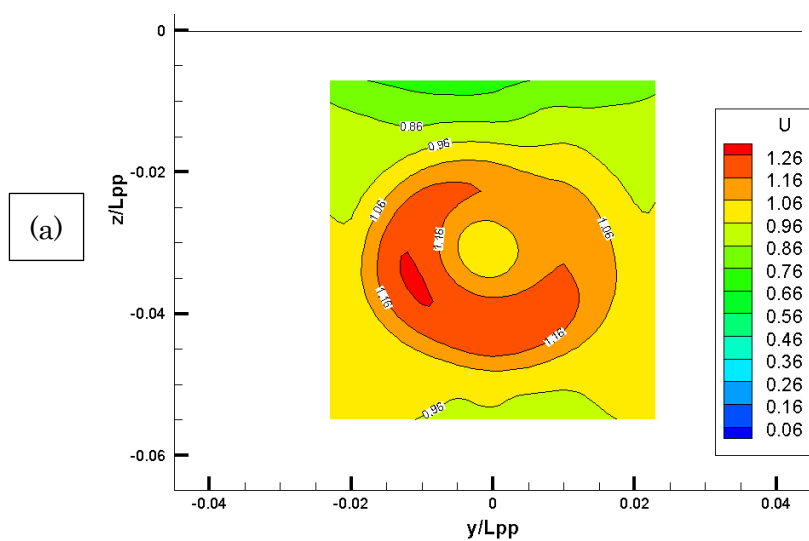


Figure 3-19 Comparison of cross-flow components between CFD (a) and EFD (b)
at $X=1.05$ section



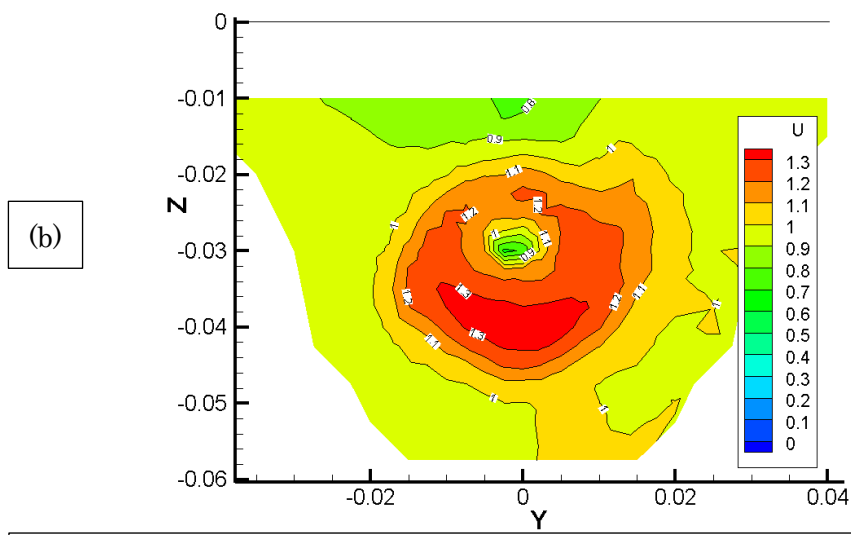


Figure 3-20 Comparison of axial velocity profiles between CFD (a) and EFD (b)
at $X=1.1$ section

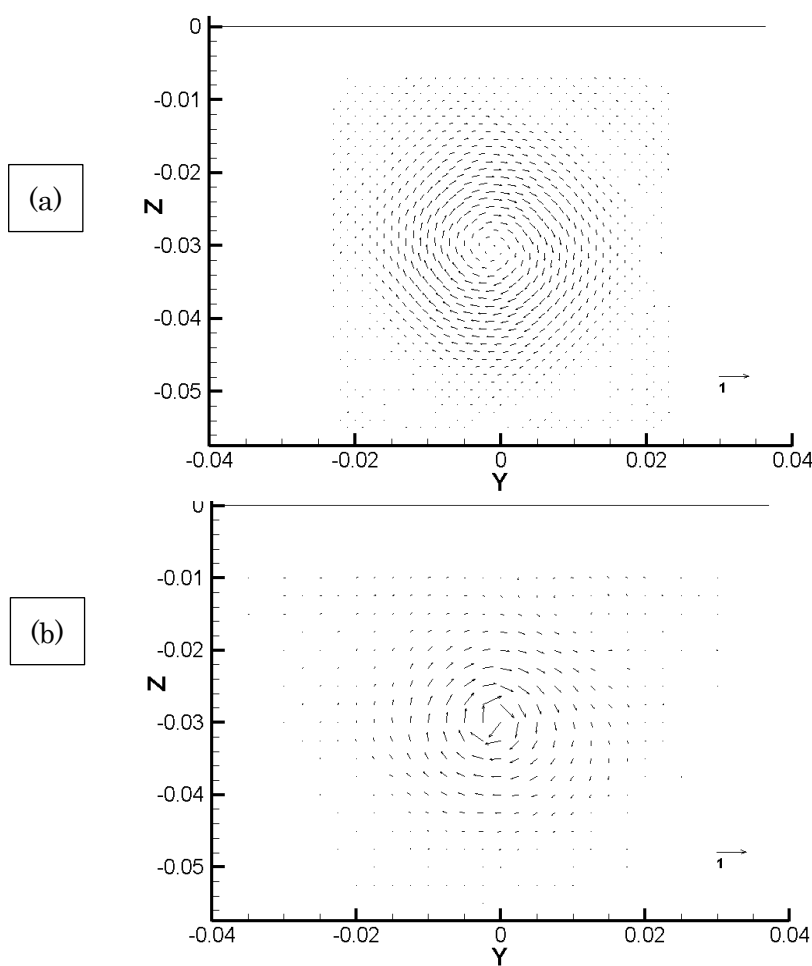


Figure 3-21 Comparison of cross-flow components between CFD (a) and EFD (b)
at $X=1.1$ section

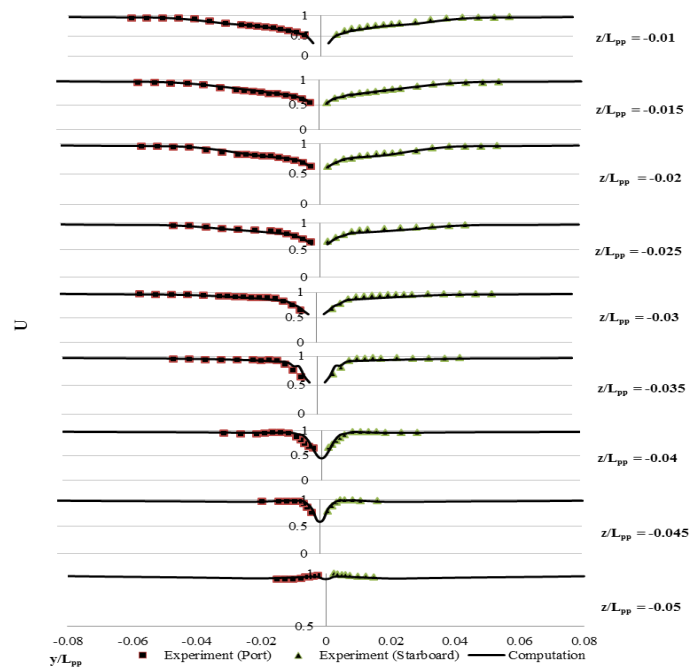


Figure 3-22 Comparison of U at $X=0.98125$ for each Z section

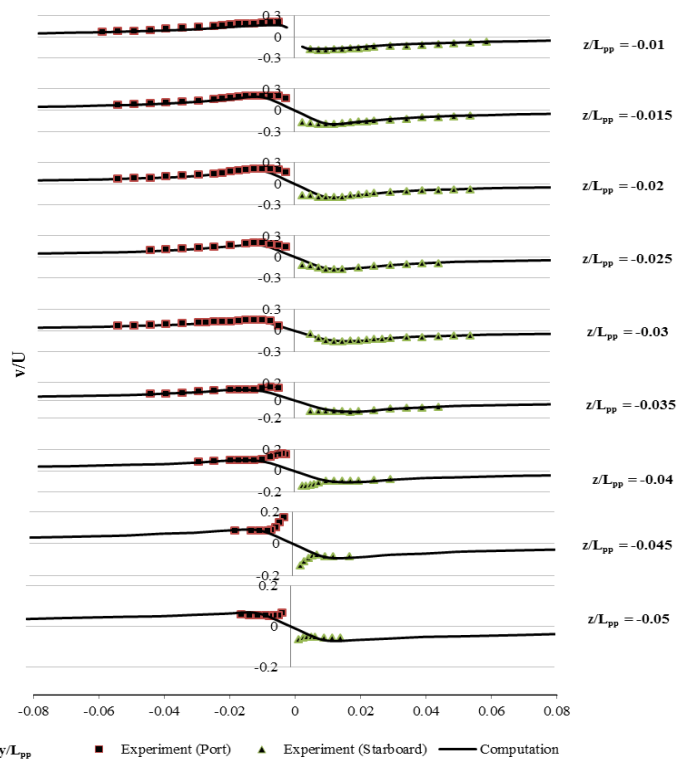


Figure 3-23 Comparison of V at $X=0.98125$ for each Z section

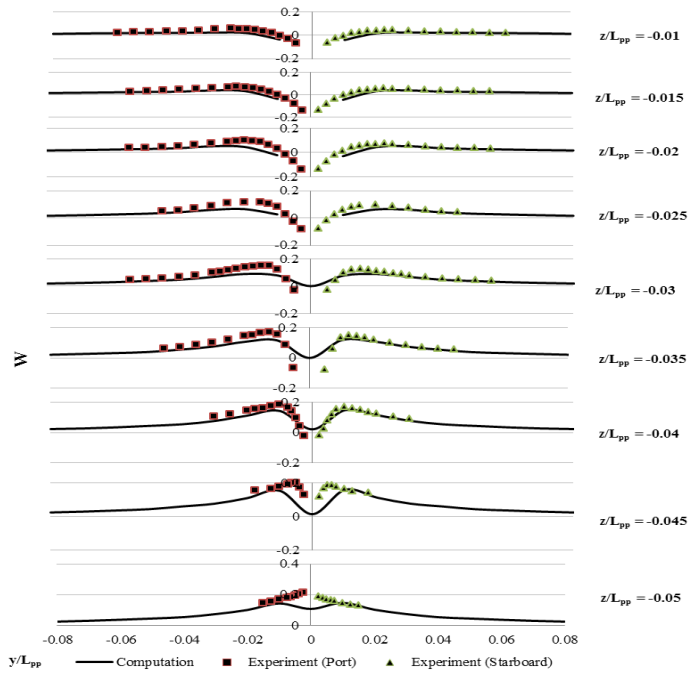


Figure 3-24 Comparison of W at $X=0.98125$ for each Z section

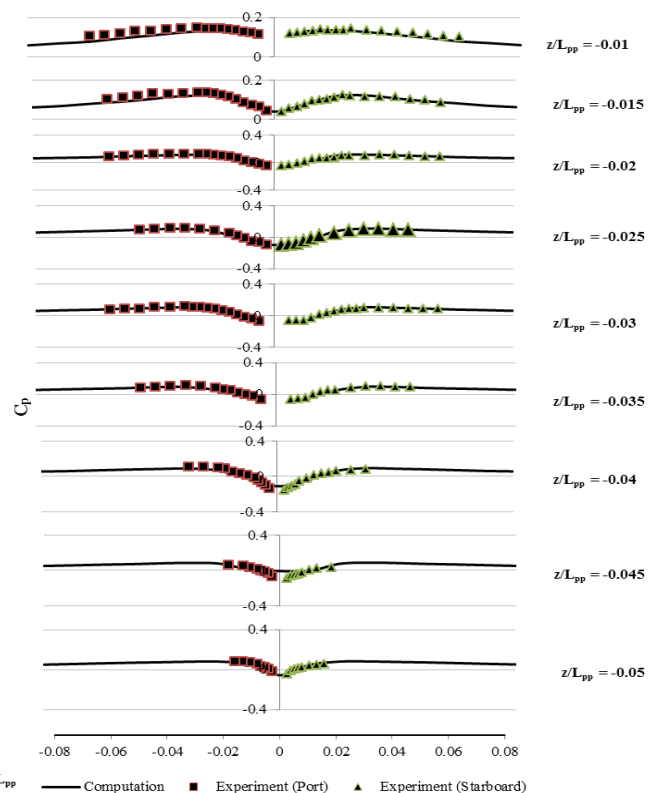


Figure 3-25 Comparison of C_P at $X=0.98125$ for each Z section

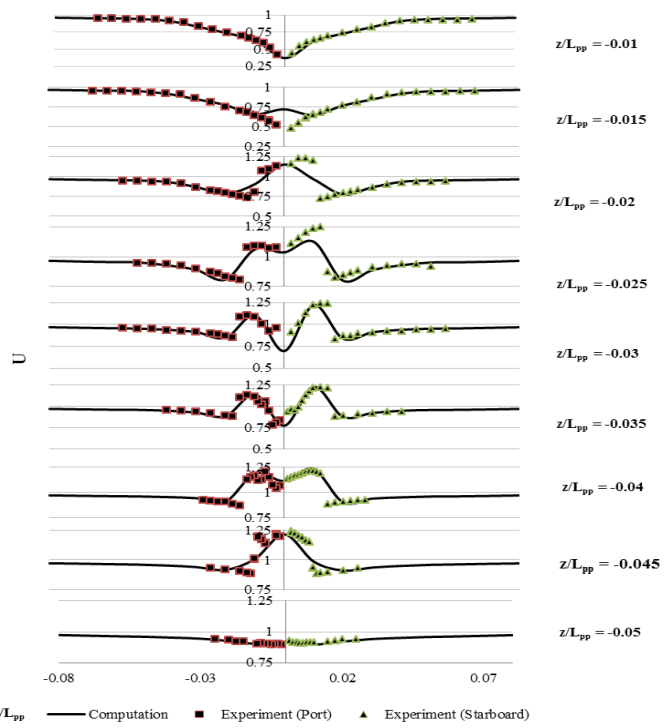


Figure 3-26 Comparison of U at $X=1$ for each Z section

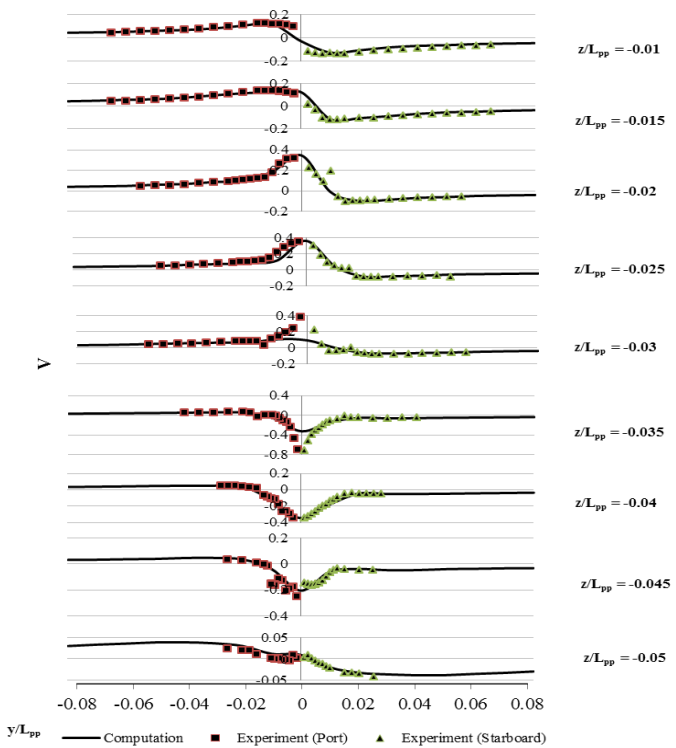


Figure 3-27 Comparison of V at $X=1$ for each Z section

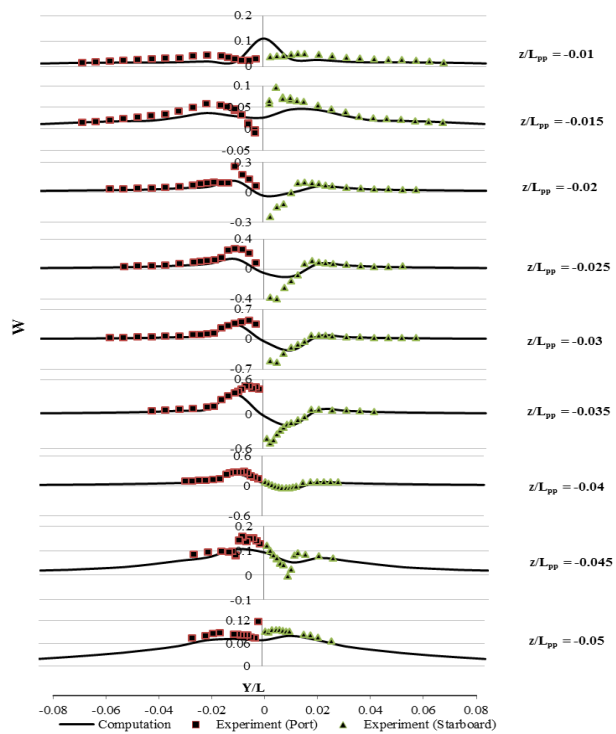


Figure 3-28 Comparison of W at $X=1$ for each Z section

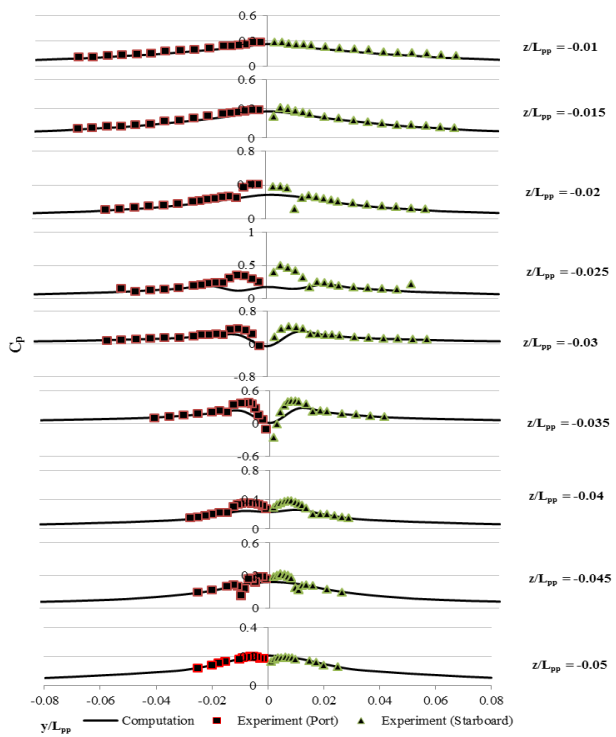


Figure 3-29 Comparison of C_p at $X=1$ for each Z section

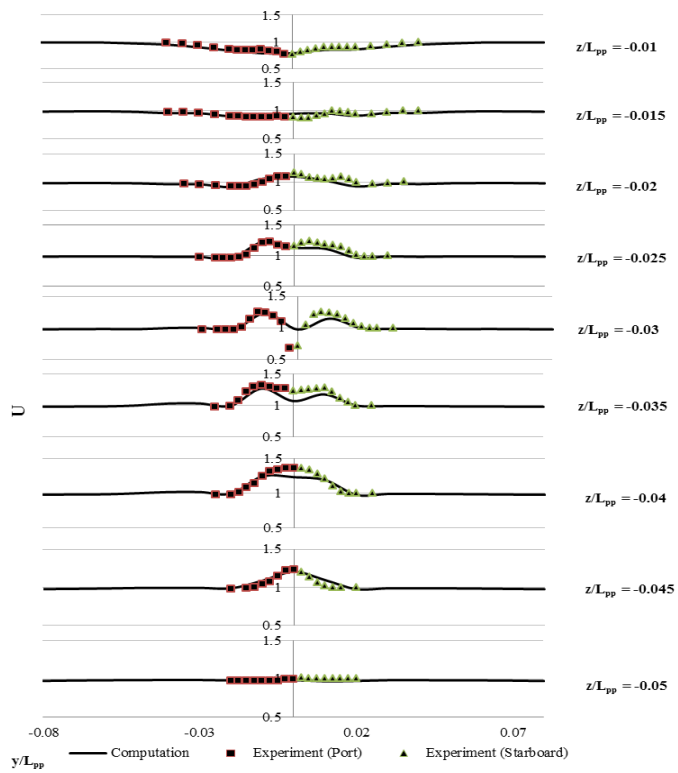


Figure 3-30 Comparison of U at $X=1.1$ for each Z section

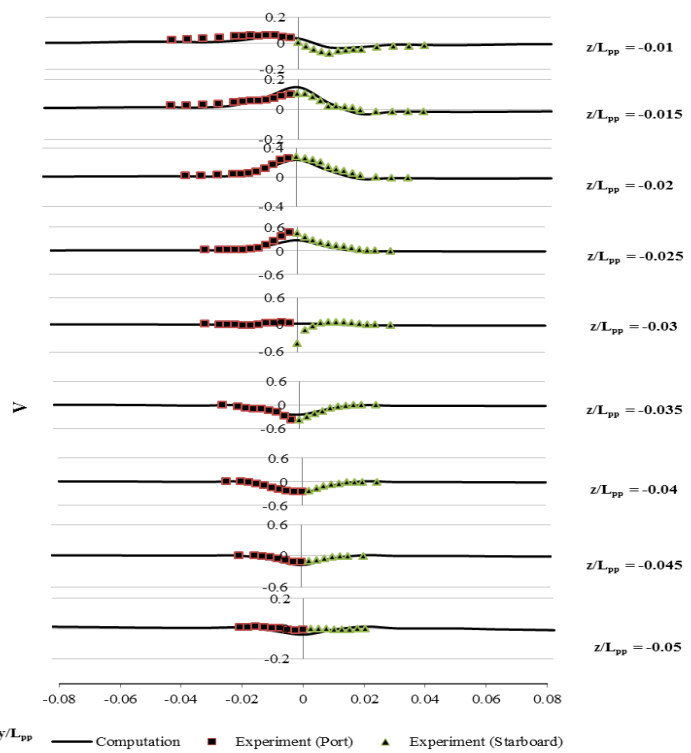


Figure 3-31 Comparison of V at $X=1.1$ for each Z section

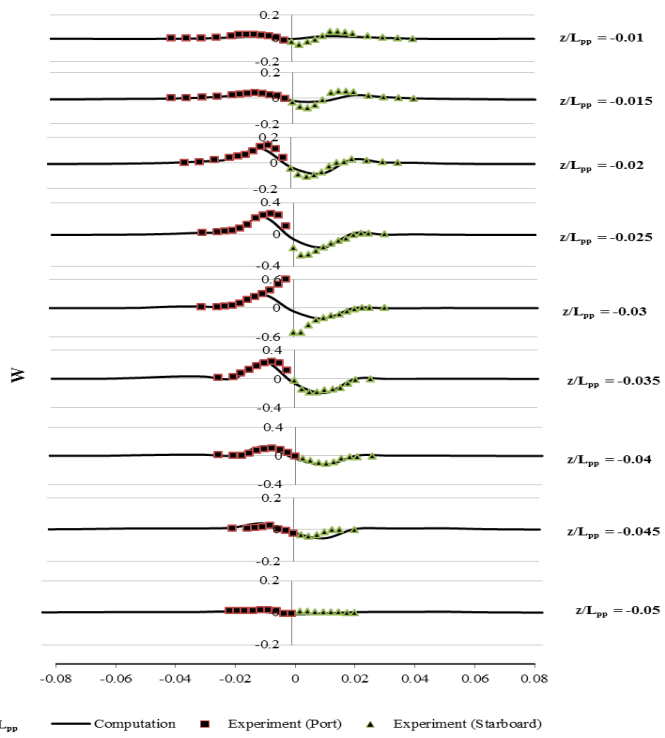


Figure 3-32 Comparison of W at $X=1.1$ for each Z section

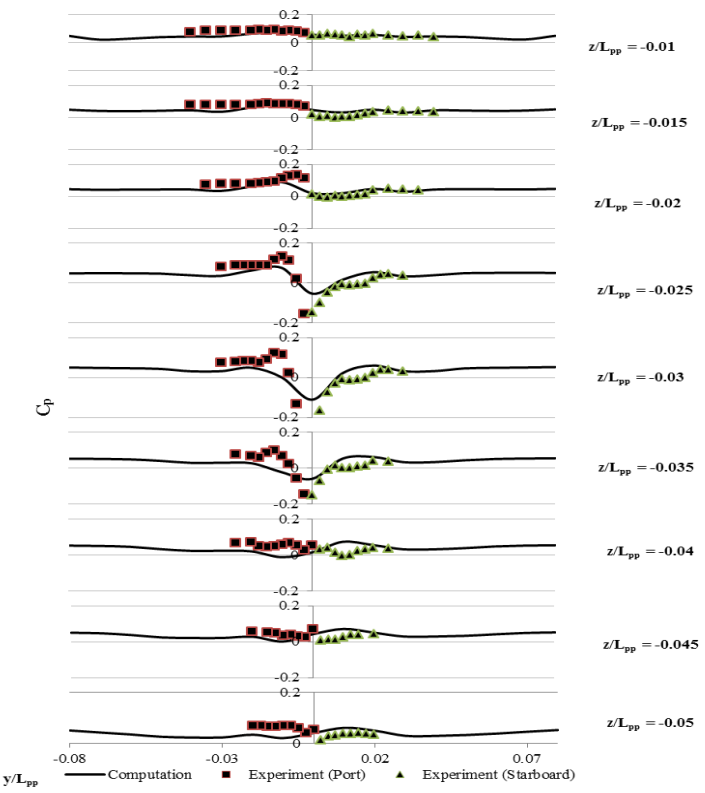


Figure 3-33 Comparison of C_P at $X=1.1$ for each Z section

3.2.3 Propeller hull interaction

Figure 3-34 and Figure 3-35 show the difference in axial-velocity contours ΔU between the with- and without-propeller conditions for regions upstream at $x = 0.98125$ and downstream of the propeller at $x = 1$. The axial-velocity difference shows the velocity changes because of the effect of propeller so that it is important to study its behavior. For upstream part, ΔU is larger near the center plane of the hull in regions of low momentum fluid where the flow undergoes largest axial acceleration. For downstream part, ΔU has the effect of propeller body force and large ΔU is observed because of the accelerated flow behind the propeller and the largest is near the hull center plane. ΔU is generally large in the starboard side than the port side due to the tangential component of the hull wake. ΔU is studied for each z section with EFD data. At $Z = -0.02$, as it is still near the hull, the boundary layer is thick and ΔU shape is broad whereas for $Z = -0.045$, the boundary layer is thin and ΔU is narrow, peaked. Generally, most of the data trends are similar to the EFD data with a bit lower ΔU near the center plane.

When the ship is towed without propeller, the pressure field is high near the stern region, making an additional forward force which is consequently reduced the resistance. So the surface-pressure contour near the stern is an interest to know the effect of propeller. This behavior is clearly shown in Figure 3-36. The high pressure contour level in without-propeller condition becomes somewhat lower in with-propeller case. As there is no stern tube on the hull, the pressure contour at the end of the stern is different with EFD where the negative pressure occurs in the above and positive pressure in the below of the stern tube due to the boundary layer effect which is shown

in Figure 3-37. The pressure difference is computed by subtracting the with-propeller from the without-propeller and that explains the propeller effect on the hull. In order to see the propeller effect more clearly, the surface pressure is plotted at each Z section along the hull at the stern region in Figure 3-38, comparing the data between with- and without-propeller conditions and the propeller effect is distinctly clear to see. The surface pressure of the port and starboard side are similar so that only port side data are illustrated.

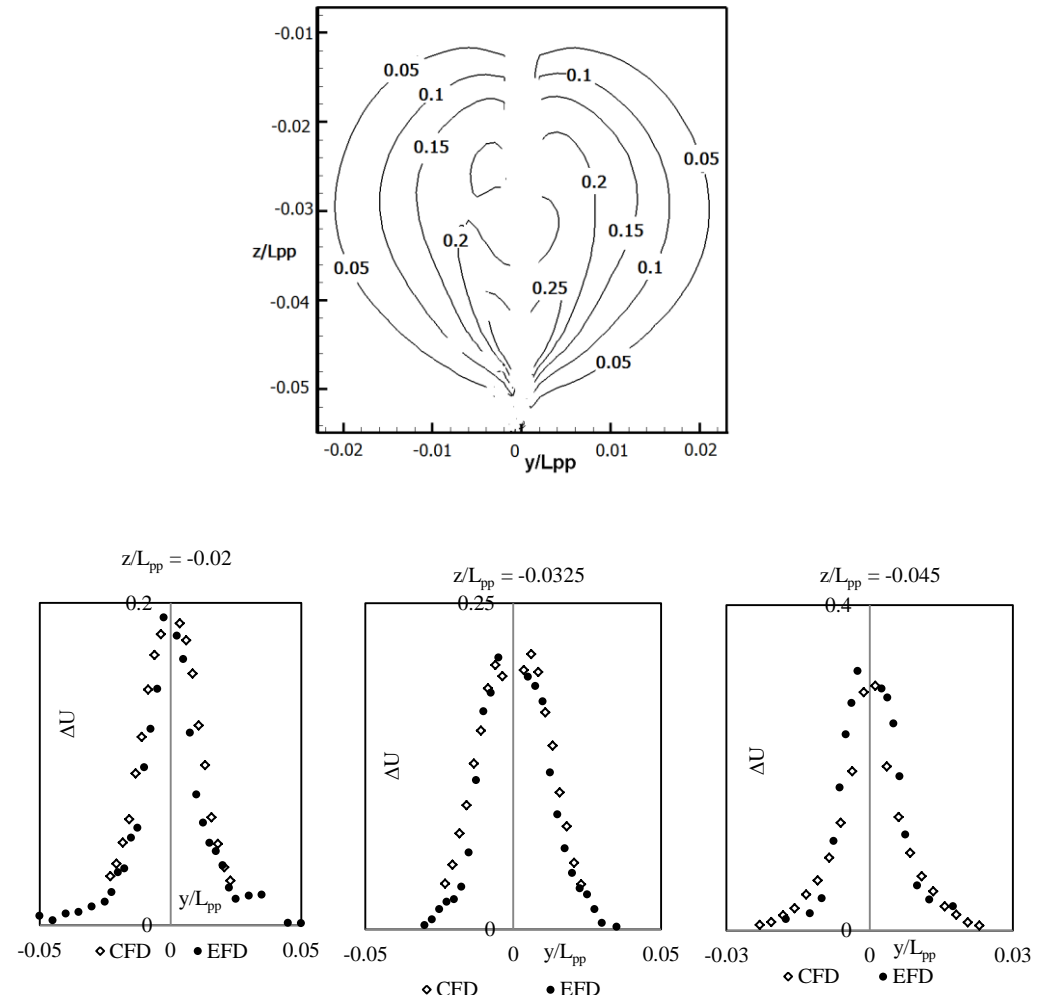


Figure 3-34 Axial-velocity difference ΔU between the with- and without-propeller conditions for upstream of propeller

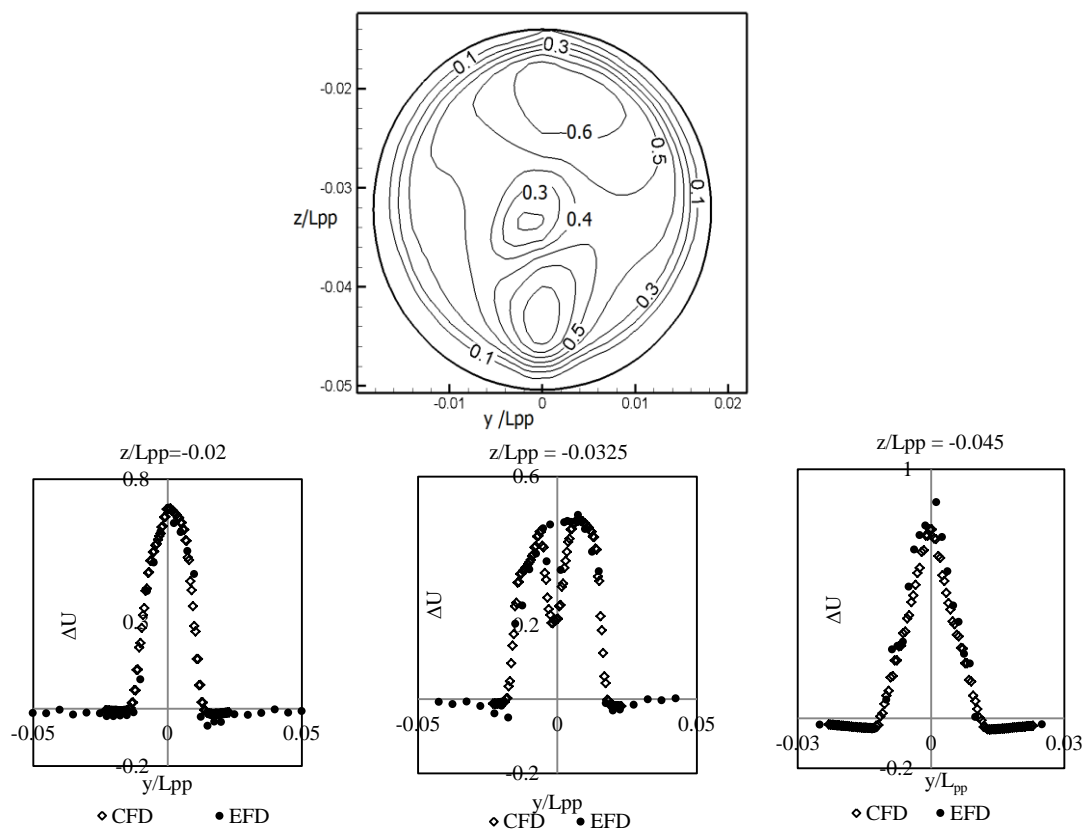
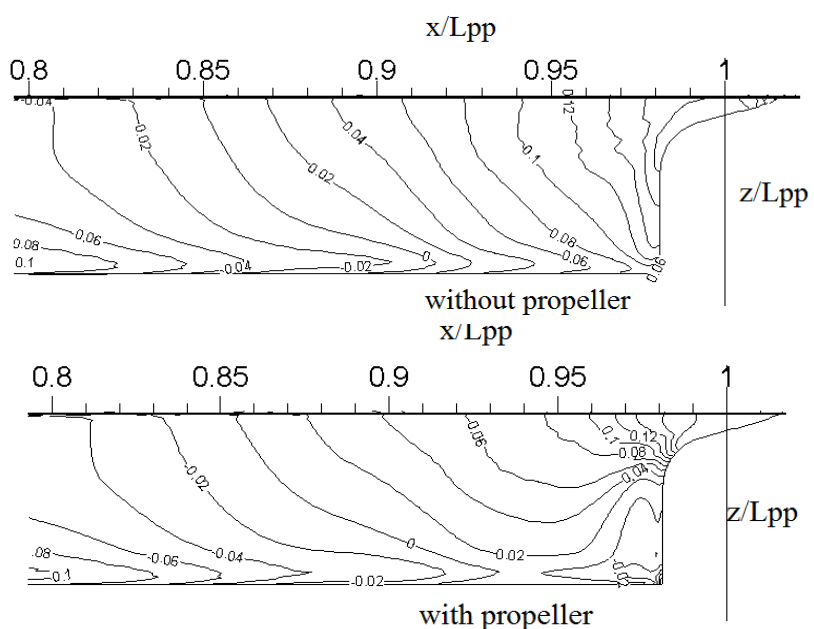


Figure 3-35 Axial-velocity difference ΔU between the with- and without-propeller conditions for downstream of propeller



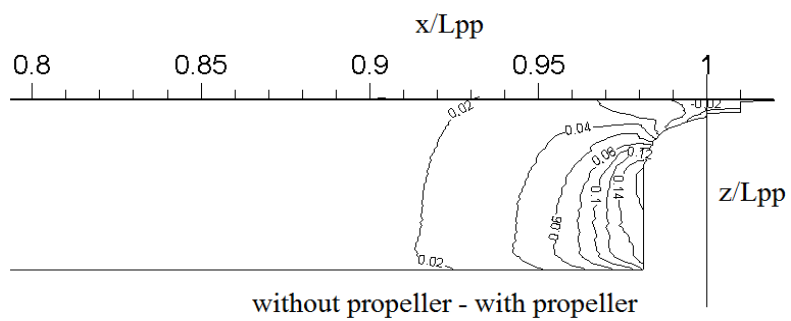


Figure 3-36 Surface-pressure distributions: pressure contours (CFD)

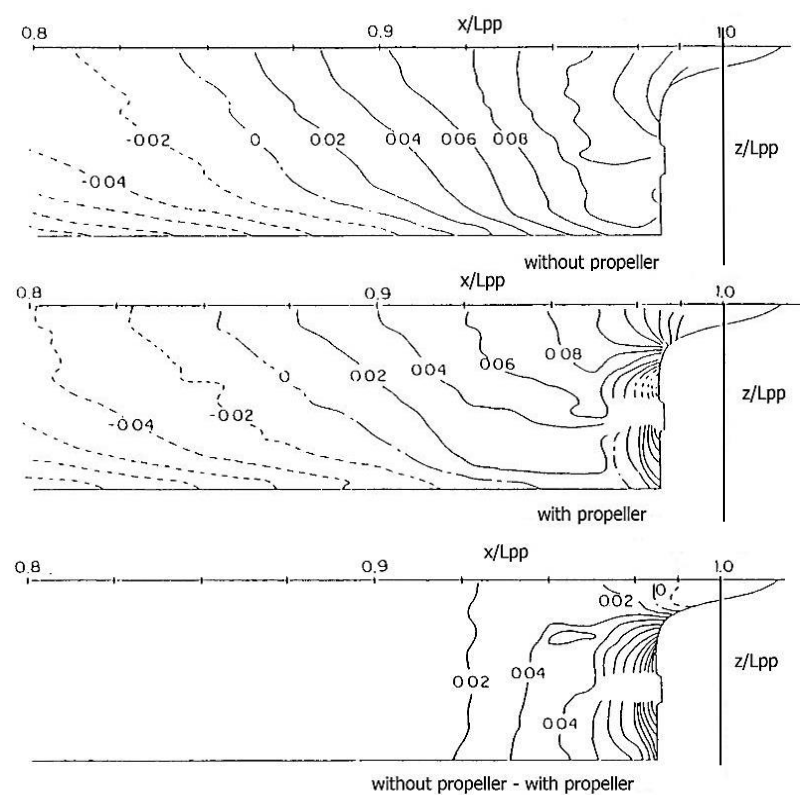
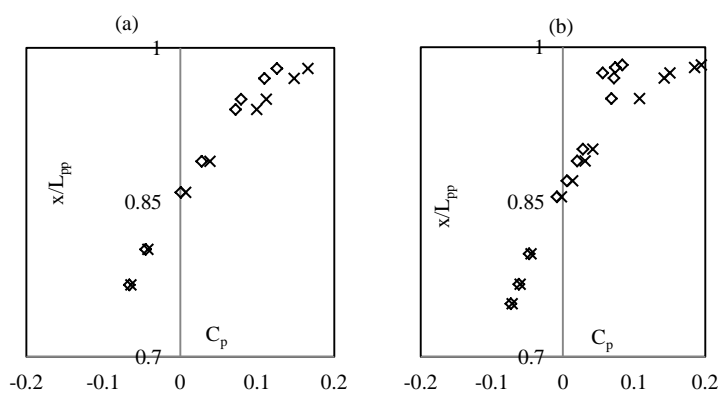


Figure 3-37 Surface-pressure distributions: pressure contours (EFD)



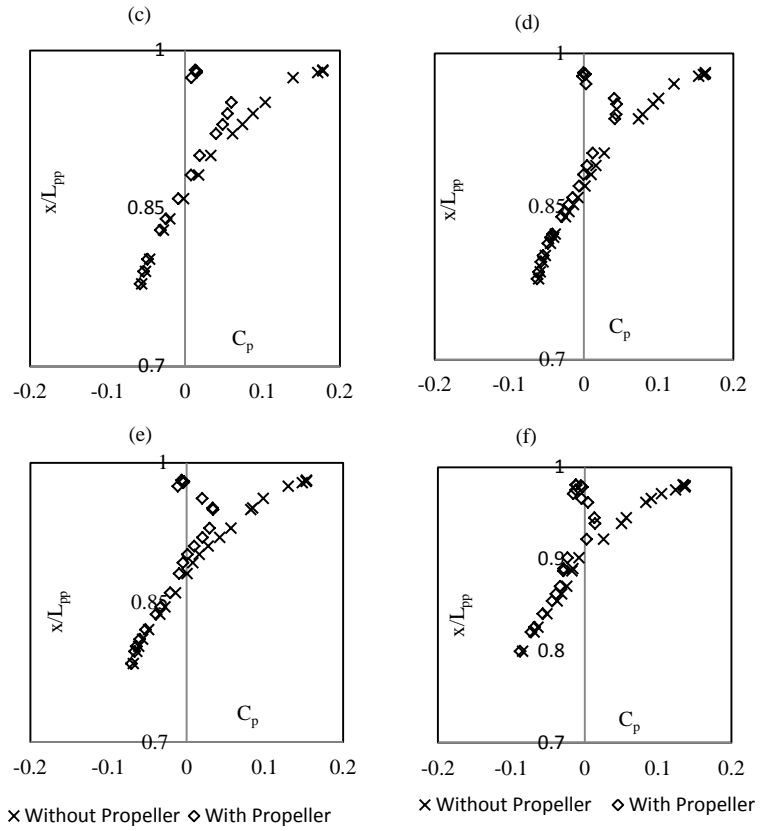


Figure 3-38 Surface-pressure distributions: stream-wise variation (a) $Z=-0.008$ (b) $Z=-0.016$ (c) $Z=-0.023$ (d) $Z=-0.031$ (e) $Z=-0.038$ (f) $Z=-0.046$

3.3 COMPUTATION OF LOAD-VARYING TEST

The propeller model has been computed for fixed number of revolution and the propulsion quantities as well as the flow field has been studied in comparison with EFD data with the validation in good agreement. The proposed propeller model becomes an interesting tool to use for load varying test which is mostly treated in present by the axisymmetric prescribed body-force method based on the Hough and Ordway circulation distribution. To check this capability, the propeller is necessary to rotate on various numbers of revolutions from low loading to higher loadings continuously with the precise configuration of the thrust and torque force.

In the current work, the advanced coefficients based on ship speed J_S are set at 1.05 (6.5 rps), 1.02 (6.7 rps), 0.93 (7.4 rps), 0.88 (7.8 rps) and 0.87 (7.9 rps) of which 0.88 case has been computed and proved in the above sections. So, the other four cases will be computed similarly starting from the converged nominal solution of bare hull and using the body-force relaxation factor as a control function and the computation is performed until the thrust and torque coefficients are converged. This is known as the load varying test and these results are plotted in Figure 3-39 and the comparison of the result is shown in Table 3-2.

Table 3-2 Propulsive quantities at various loadings

J_S	CFD		EFD	
	K_T	$10K_Q$	K_T	$10K_Q$
1.05	0.189	0.358	0.182	0.345
1.03	0.196	0.367	0.189	0.350
0.93	0.225	0.401	0.215	0.394
0.88	0.238	0.416	0.234	0.411
0.87	0.242	0.420	0.233	0.421

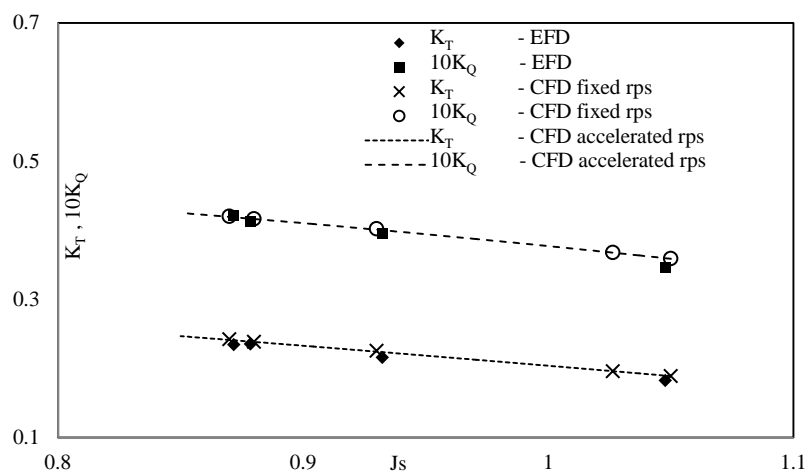


Figure 3-39 Thrust and torque coefficients of load varying test

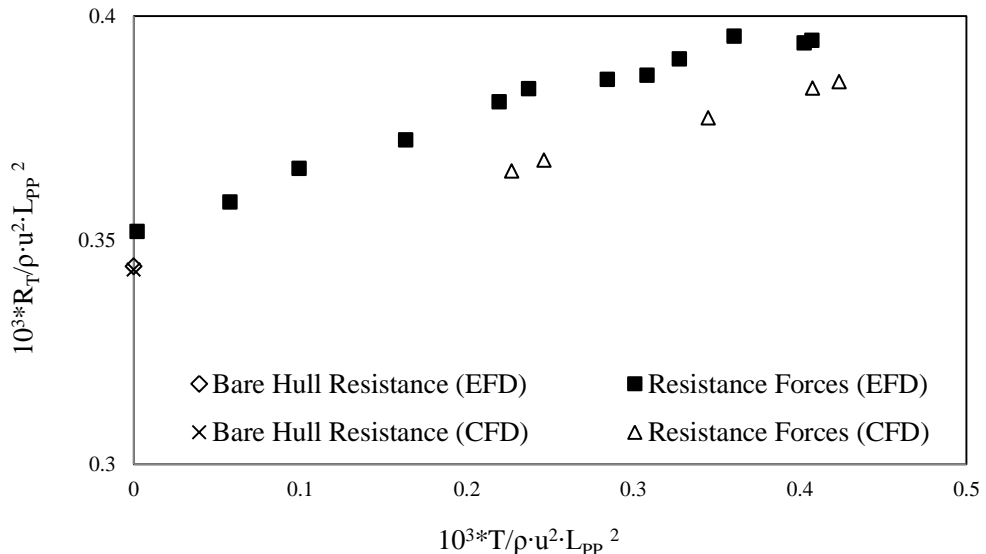


Figure 3-40 Total resistance comparison of bare hull and with propeller case

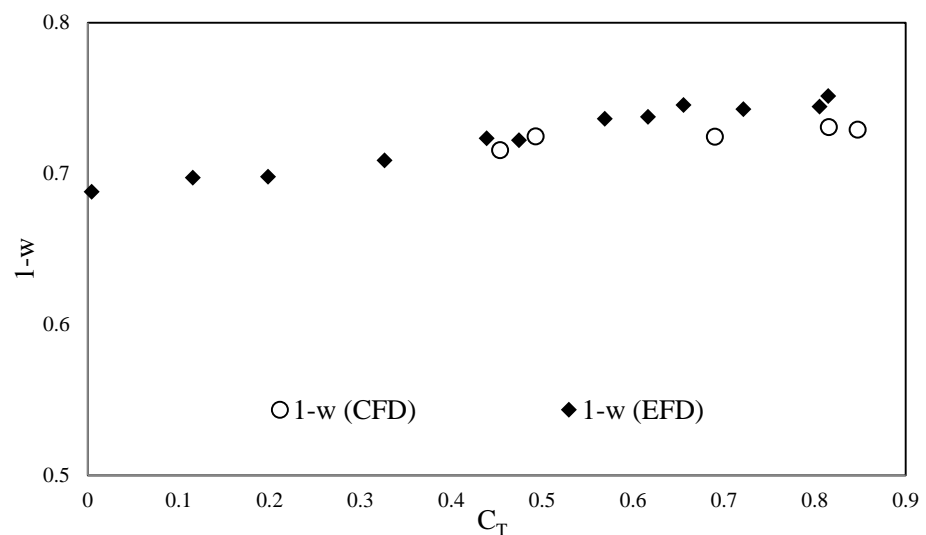


Figure 3-41 Wake fractions with respect to the loading coefficients

In load-varying test, the propeller is turned on at low number of revolution which is then increased to higher loading gradually and the computation is required to be able to handle the case with accurate estimation of the thrust and torque while the loading is

increased. So, firstly, the propeller is set to run at $J_S = 1.05$ until converged, then, the number of revolution is increased gradually in each time step in a small interval and computed until $J_S = 0.85$ and the result is represented by line illustration in Figure 3-39. Surprisingly, the line passes all dotted points that mean the propeller can predict the right thrust and torque while the loading is increasing gradually. So, the proposed propeller model has a capability to work for various propeller loadings even with the side forces by the inflow velocity components of V and W that is restricted in the axisymmetric body-force model which is widely used for load varying test these days.

Figure 3-40 shows the total resistance on various propeller loadings comparing with the experiment. The bare hull resistances of CFD and EFD are plotted at $T = 0$ with good agreement. In EFD, the resistance forces are a bit higher than the bare hull resistance that is the effect of the propeller which makes the pressure in the stern region lower and increase the total resistance. The higher the loadings are, the higher the total resistance is. In CFD, the similar slope is observed where the value is lower than EFD. It is reasonable to explain this feature as hub and cap are neglected in the computation that means there is blank region in the hub and some of the flow passes through this place while the propeller is working and that phenomenon reduces the total resistance. Because of this effect, the thrust deduction factor is a bit hard to compute. But, the two slopes of resistance forces are similar and the propeller is evident at its good working ability. Moreover, the computation is carried out at fixed condition and experiment is carried out at free condition so that the detail comparison error is not valid to account. The wake fraction based on loading coefficient, $C_T = \frac{2T}{\pi^2}$ is shown in Figure 3-41 and all values are lower than EFD data as the propeller over-predicts at all cases as shown in Table 3-2.

CHAPTER 4: WITH-HUB COMPUTATION OF S60

4.1 OVERVIEW OF COMPUTATIONAL CONDITION

In Chapter 3, the computation of without-hub case has been studied and some weak facts have been pointed out. In this chapter, in order to know the effectiveness of the proposed propeller model, S60 ship hull will be modified in the stern to fit the hub grid and the computation will be carried out in with-hub condition. The hull form is modified in the stern with the stern tube similar to the experiment and the grid is generated based on this offset. The hub grid is generated as separate blocks and the hub surface mesh is brought to overlap on the ship hull surface. The overlapping part is finished by using SUGGAR which is run by Dr. Ping-Chen Wu as it is the confidential computing code owned by IIHR. The detailed information of the overset grid and its size can be referred to Chapter 2. All the boundary conditions mentioned in Table 3-1 are applied with the additional rotating boundary condition of the hub surface. When the propeller is working, the hub rotates with the same rate and this boundary condition type is not included in CFDSHIP-Iowa so that the condition is implemented manually in the code. The boundary condition is implemented to the hub surface at the same revolution rate of propeller and the illustration of the rotational vectors on the hub surface is shown in Figure 4-1.

The computational procedure is the same as Chapter 3 where the computation for the bare hull itself is carried out with sufficient time steps to get a converged solution to solve the nominal wake field which is important to be in proper condition for the propeller model and the propeller model will be coupled with the converged bare hull

solution. All the steps of the analyses of the flow field as in Chapter 3 will be repeated again and the details of the comparison not only between with- and without-hub but also between with-hub and EFD will be presented in the following sections.

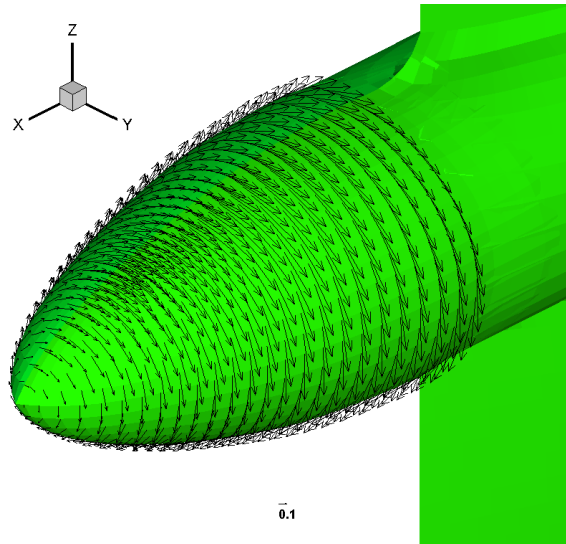


Figure 4-1 Rotational boundary condition on the hub surface

4.2 PROPULSIVE QUANTITIES AND FLOW FIELD ANALYSES

The analysis of the flow field especially in the wake region is presented in this section. At first, the result of the converged solution of the bare hull will be discussed and compared with EFD flow field at the propeller plane which is shown in Figure 4-2. The axial velocity distribution is extracted after the converged solution is obtained and the circle marks the propeller disc area with the small white circle inside that represents the hub. The wake inside the circle is mainly analyzed as the propeller quantities will be computed inside that disc area and good agreement with EFD is achieved especially at the center line where such pattern could not be observed in the computation in Chapter 3.

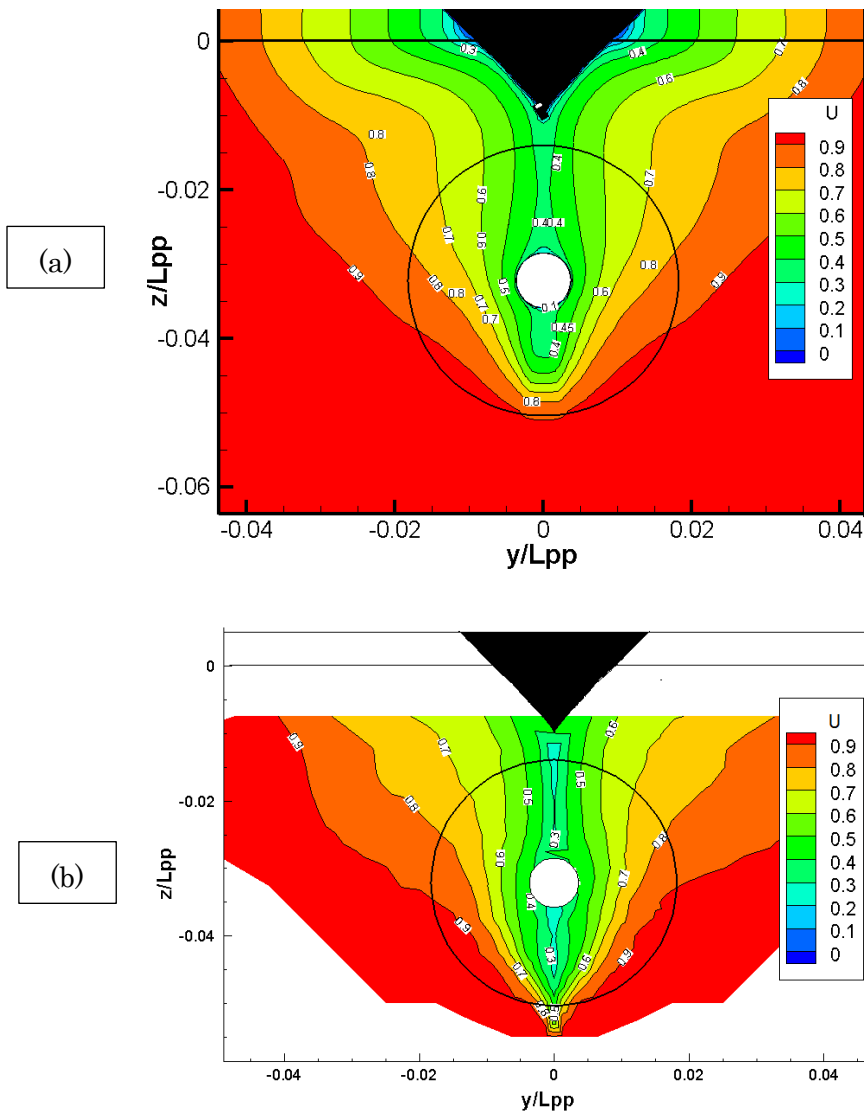


Figure 4-2 Comparison of axial velocity profiles between CFD (a) and EFD (b)
at $X=0.9875$ section

After the bare hull result is validated, the propeller model is turned on and coupled with converged RANS solution. The computation with the propeller is carried out using the grid shown in Figure 2-1 with the hub at the propeller number of revolution of 7.8 rps when using 4m model and 0.14564m diameter propeller. The no-slip rotational boundary condition as shown in Figure 4-1 is applied to the hub with the same number of revolution.

The body-force is calculated on the propeller block at the propeller plane $X = 0.9875$ and it is distributed in X direction throughout the propeller block covering the propeller blades positions. These body force values are inserted in the momentum equation and the coupling process is carried out with the RANS code. For the prevention of numerical divergence, the body-force relaxation factor is used by setting small value at the beginning of the time step and increasing it gradually to the full relaxation factor. The computation is continued until the thrust and torque coefficients are converged. The converged thrust coefficient is 0.240 and torque coefficient is 0.042 which is a bit higher than without-hub computation.

The effective wake factor is calculated as in equation (32) and the definition has been explained in Chapter 3. The effective wake factor of the current work is 0.727 which is a little bit lower than EFD which shows 0.75 as well as than previous computation, 0.73 as the thrust and torque are over predicted. The thrust deduction factor, which expresses the effect of the suction of the propeller on the hull, is defined by equation (33) where R_{T0} is the bare hull resistance, R_T is the resistance with propeller and T is the thrust of the propeller. The thrust deduction factor $(1 - t')$ of the computation gives as 0.873 which is very close to EFD, 0.86. The further discussion for self-propulsion coefficient is skipped here, because the resistance and propulsion tests were done for sinkage and trim free condition and velocity measurement and computation were done for fixed even keel condition.

$$t' = \frac{R_T - R_{T0}}{T} \quad (33)$$

For the flow field analyses, many stations will not be chosen to study like the procedure in Chapter 3. As the downstream part at $X=1$ is the outflow of the propeller, it is important to analyze to know whether the propeller model could give right injection

or not and this station will be mainly discussed here. So, the computed flow field is extracted at $X= 1$ and the result is compared not only with the EFD data but also with the previous solution where the computation is without hub and without stern tube to understand the effect of the hub.

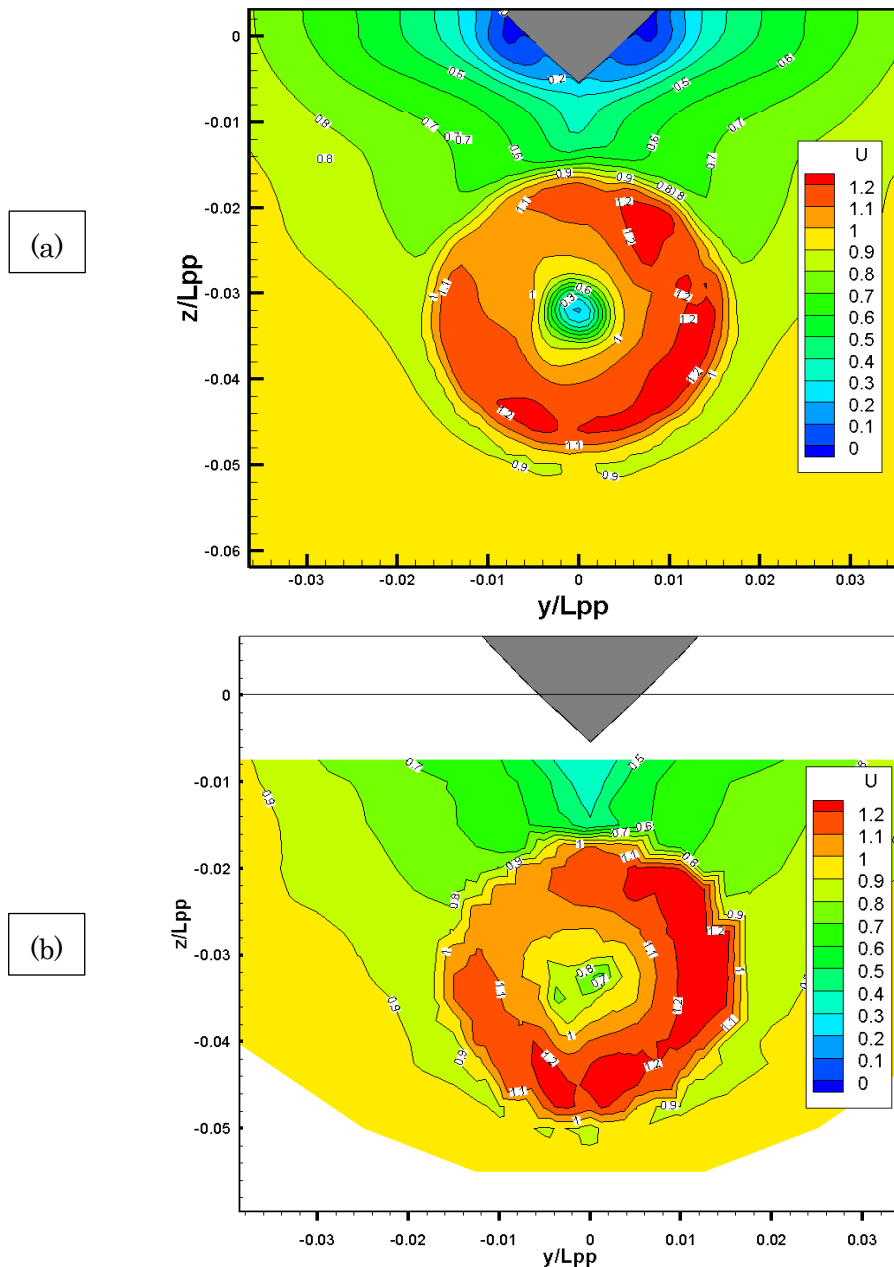


Figure 4-3 Comparison of axial velocity profiles between CFD (a) and EFD (b) at $X=1$ section

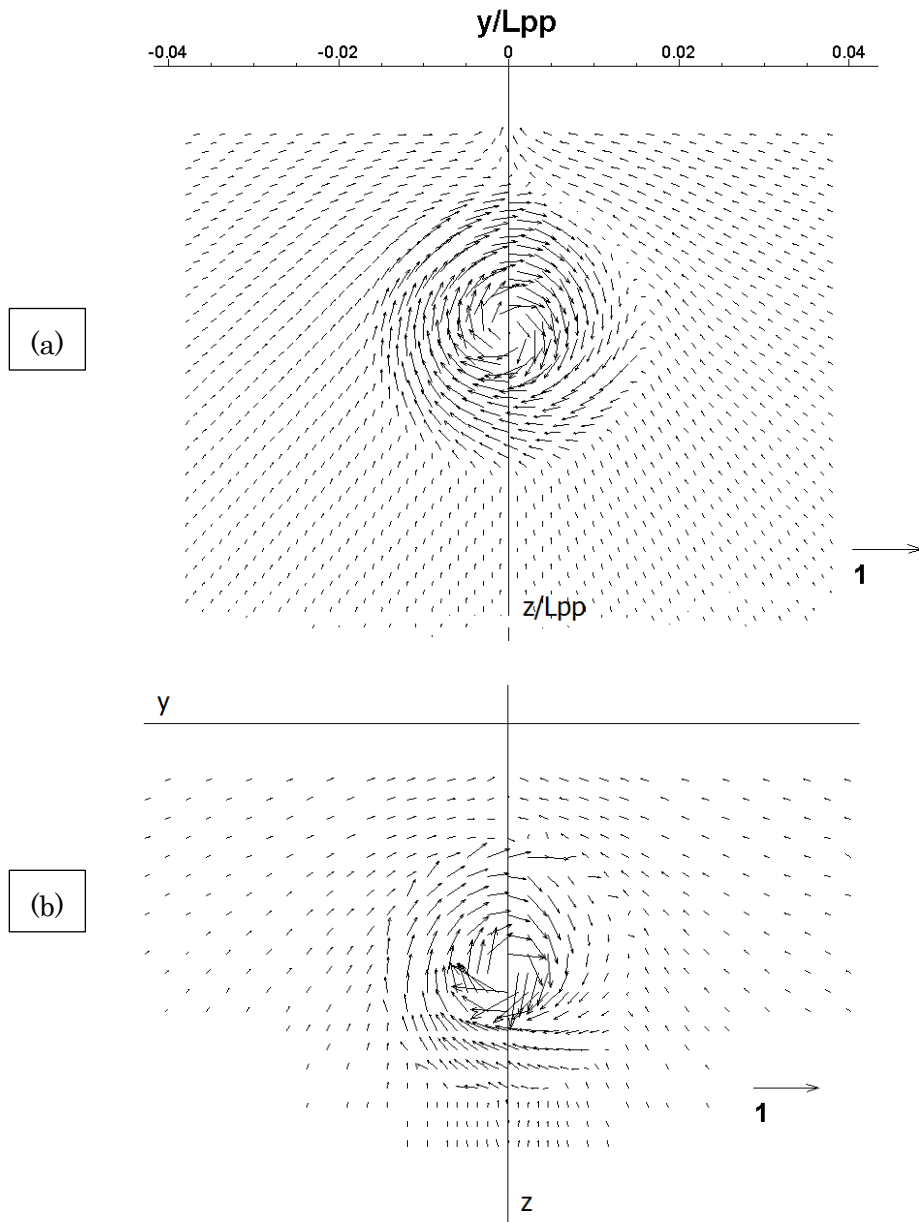


Figure 4-4 Comparison of cross-flow components between CFD (a) and EFD (b) at $X=1$ section

In Figure 4-3 and Figure 4-4, the comparison of the axial velocity field and cross-flow components at $X=1$ is illustrated. By comparing with the previous computation, the condition with hub gives closer agreement in contour pattern. For example, by comparing to Figure 3-14(a), the contour level 1.1 of Figure 4-3 (a) is much closer to

EFD and the pattern near the shaft axis shows the effect of presence of the hub clearly which could not be observed in the previous computation. The other regions do not have much difference and show good agreement. For the cross-flow components, the vector lengths are almost same on the propeller region but near the shaft axis, the computation shows a bit shorter shape that is caused by the dissipation in numerical computation. But, the vectors in Figure 4-4 (a) seem longer than Figure 3-15 (a) so that Figure 4-5 is drawn to see the effect of hub in the computation. In Figure 4-5, the cross-flow vectors are drawn with the red color for without-hub computation and black arrow for present case. It is distinct that the black vectors are longer than the red especially near the shaft axis that shows the effect of the vortex by the rotating hub. Generally, the computation with hub gives much stronger cross-flow velocity fields than without-hub but it is still weaker than EFD. The reason of this dissipation may be raised from the turbulence model or the overset grid part.

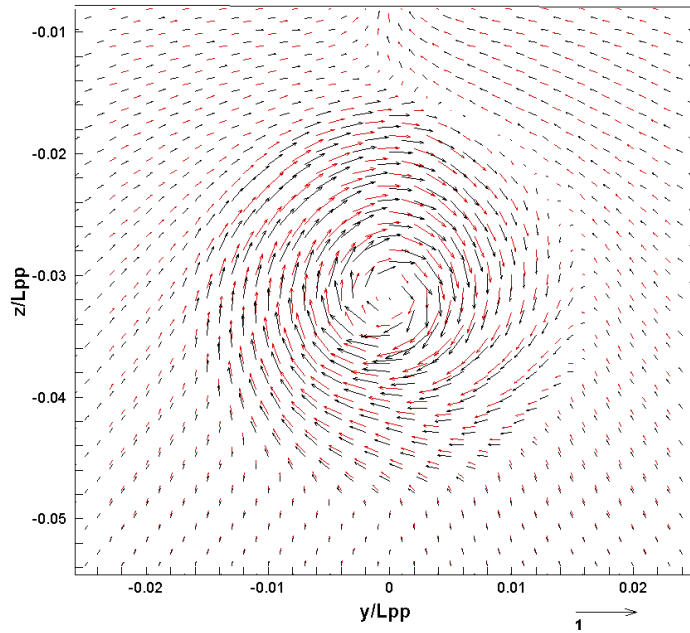


Figure 4-5 Comparison of cross-flow components of the computation between with-hub and without-hub conditions at $X=1$ section

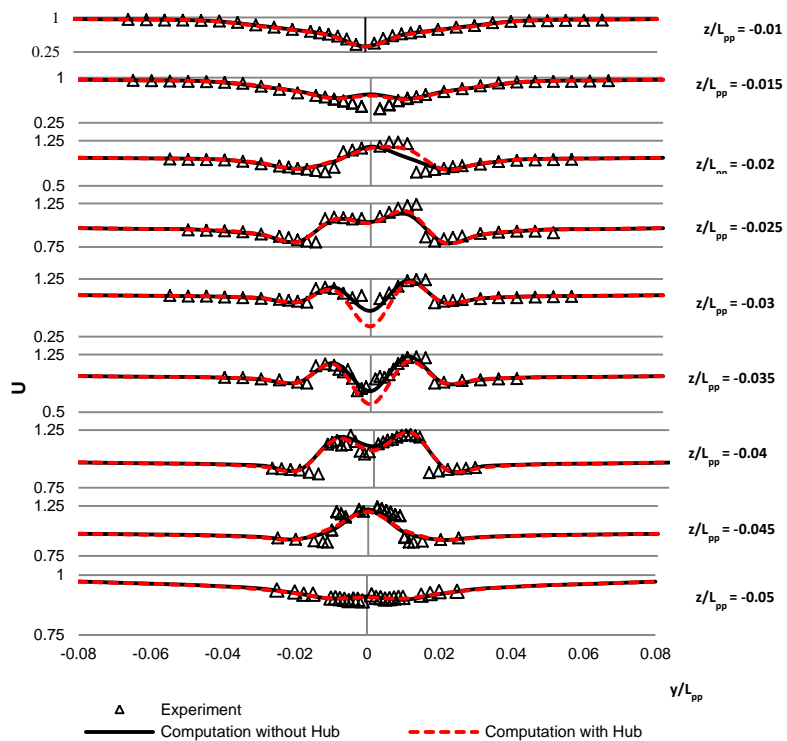


Figure 4-6 Comparison of U at $X=1$ for each Z section

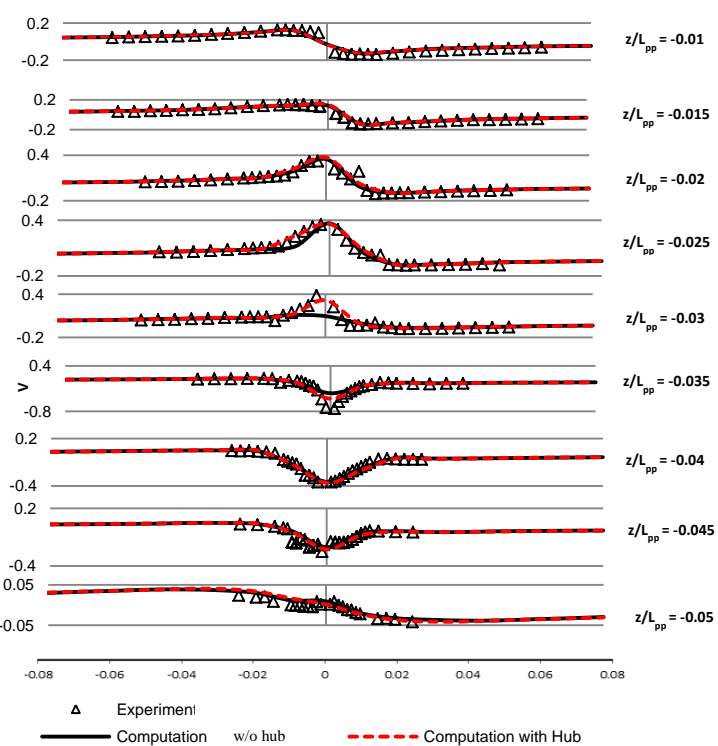


Figure 4-7 Comparison of V at $X=1$ for each Z section

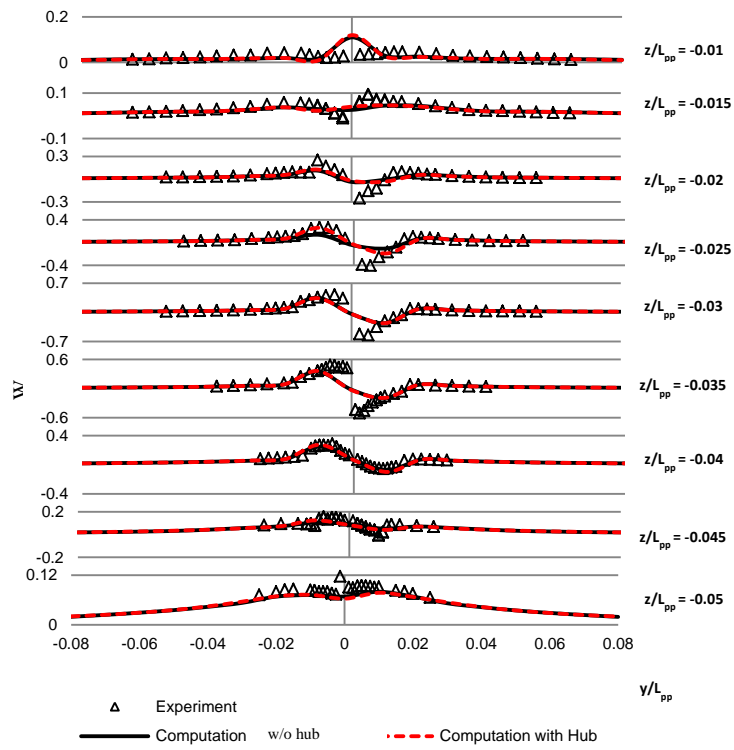


Figure 4-8 Comparison of W at $X=1$ for each Z section

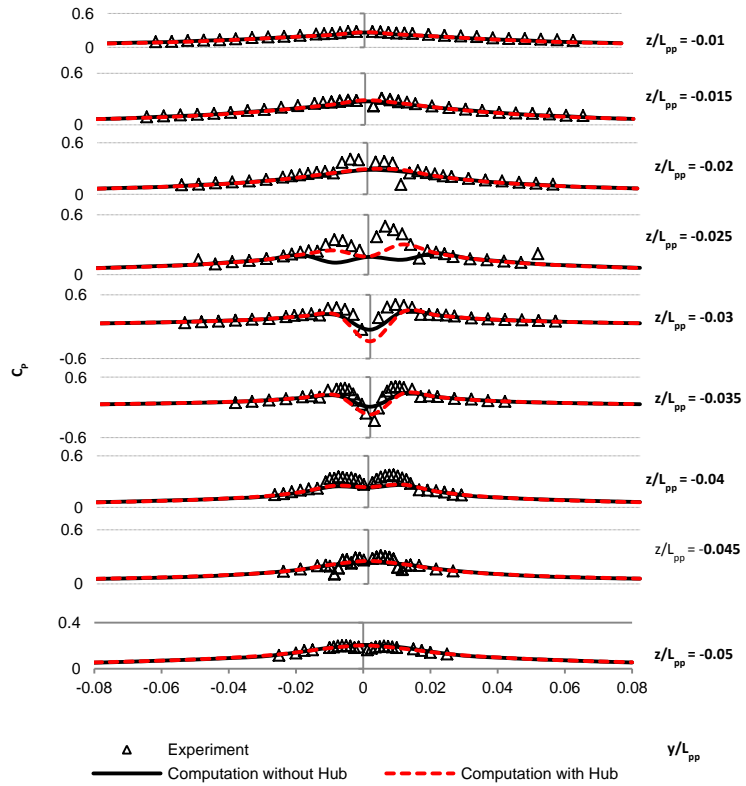


Figure 4-9 Comparison of C_p at $X=1$ for each Z section

The detailed comparison of the flow field is plotted in Figure 4-6 to Figure 4-9 between the computation with-hub, without-hub and EFD for with-propeller condition. The results of the present computation are almost same with the previous computation but the effect of hub could be observed especially in cross-flow component V . In Figure 4-7, the red dotted line shows closer to EFD at $Z = -0.03$ and -0.035 which is around the hub. At $Z = -0.025$, the current computation shows better agreement. The major difference could not be observed for component W except a better agreement at $Z = -0.025$. There are also some better results of pressure coefficient C_p at $Z = -0.025$ and -0.035 in Fig.12 and axial velocity U at $Z = -0.02$ section in Figure 4-6 and but for axial velocity comparison, it shows with-hub condition less agreement though the peak values are still same with EFD. This might be caused by the thick boundary layer effect of the rotating hub and the turbulence model to deal with these effects. Also in Figure 4-3, the axial velocity is very low at the shaft center position too. As the wake field is much complicated and the rotating effect is also included in this work, some other turbulence models will need to be switched to find reasonable agreement.

The surface-pressure distribution for this case is shown in Figure 4-10 which can be compared with the experimental distribution in Figure 3-37. The high pressure region near the stern of the hull without propeller is reduced by the interaction of propeller behind the ship. The high pressure contour level in without-propeller condition becomes somewhat lower in with-propeller case. In with-propeller case, the negative pressure could be observed at upper part of the stern tube which is closer to experiment. This pattern could not be observed in the previous computation. But, the shape of pressure contribution between CFD and EFD is a bit different that might also relate to

the turbulence model. The pressure difference which is computed by subtracting the with-propeller from the without-propeller explains the propeller effect on the hull and good agreement is observed between CFD and EFD. The surface pressure of the port and starboard side are similar so that only port side data are illustrated.

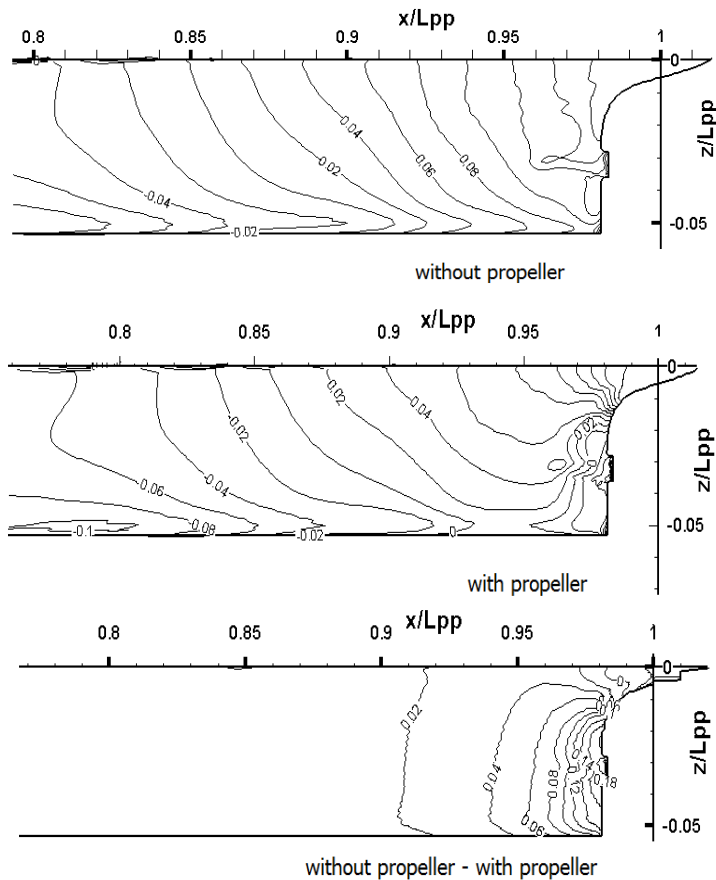


Figure 4-10 Surface pressure distribution of CFD results

As this chapter is extended to see whether the propeller model is working well with the hub or not and the changes that can be raised from the hub. So, the detailed analyses of every topic as in Chapter 3 will not be discussed here. All the explanations and discussions in Chapter 3 and Chapter 4 can convince that the proposed model is quite effective.

CHAPTER 5: COMPUTATION OF KVLCC2 MODEL

5.1 OVERVIEW OF COMPUTATION

After the general merchant ship hull form S60 has been studied with the proposed propeller model, it is essential to understand the capability of the model in other types of hull form, too. Another test case is carried out using the tanker model known as KVLCC2. The ship was originally designed by Korea Research Institute for Ships and Ocean Engineering to be used as a test case for CFD predictions. The ship offset has been once re-modified at the stern contour of the ship slightly by Professor Hino (Hino et al., 2005) and the modified hull form is known as KVLCC2M. In this thesis, the original hull form KVLCC2 will be employed.

The real ship is not constructed for KVLCC2 and the detailed principle dimensions and information are described in Table 2-4. Several research institutes (INSEAN, NMRI, etc.) employ the model as the study case with different scale ratios. The model used in Osaka University Towing tank is with 1/100 scale ratio and the computation will be carried out based on this model. The flow field of nominal wake and effective wake will be mainly studied in bare hull computation and with propeller case. In the experiment carried out in Osaka University, different types of rudder including normal rudder and special types fitted with energy saving devices are used. However, the computation could be carried out only for the normal rudder case only due to the time consumption for the grid generation around the complex geometry with special typed rudders and these will be left as the future work and will be excluded in this thesis.

The computation parameters are set according to the setting of experiments. The

Froude number is 0.142 and the carriage speed is set at 0.795 ms^{-1} so that the Reynolds number is 2.05×10^6 . The experiment is carried out at the full load condition for sinkage and trim condition. The non-dimensionalized forward trim is $z_a / L_{PP} = 0.000344191$ and aft trim is $z_f / L_{PP} = -0.00192805$. The trim condition illustration is shown in Figure 5-1 which shows the trim by bow with trim angle, 0.13 degree. All the grid blocks except the background and wake refinement blocks are constructed according to this trim condition.

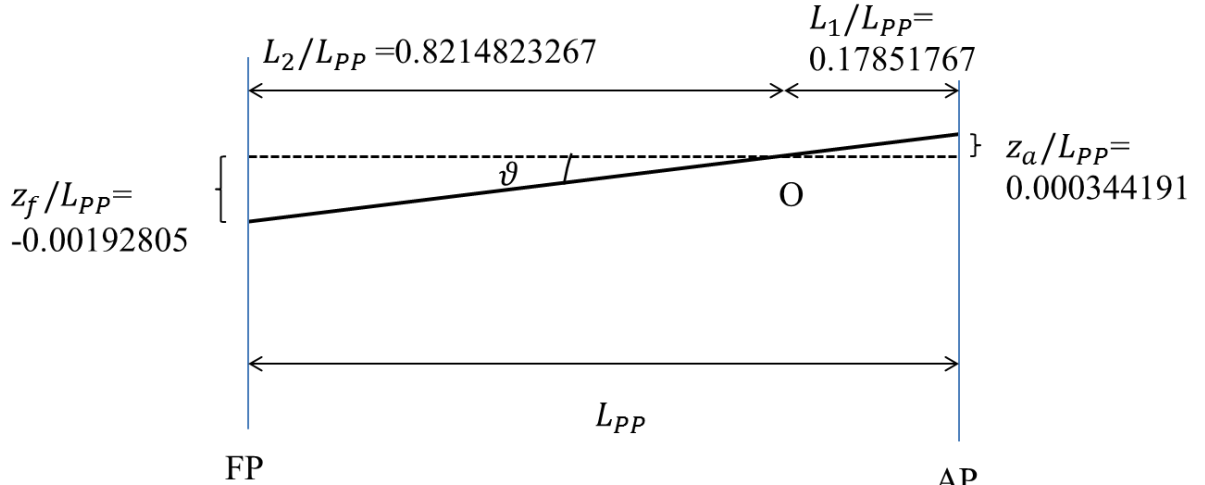


Figure 5-1 Trim position of KVLCC2 model experiment

The propeller model is explained in section 2.4. The same procedure is carried out similar to S60 model where the bare hull computation is carried out to get the converged nominal wake solution and then, the propeller model is switched on and the body-force magnitude is controlled by means of body-force relaxation factor from 0.01 to 1 gradually. At the relaxation factor 1, after the thrust and torque coefficients are converged to some specific value, the solution is believed to converge and the

computation is stopped. The comparison of thrust and torque coefficients between CFD and EFD is listed in Table 5-1. In this case, the torque coefficient of the experiment is said to be something strange and the thrust coefficients will be mainly compared. A very good agreement can be observed in both with-rudder and without-rudder cases. The thrust deduction factor is computed for the with-rudder case only which is 0.794. As KVLCC2 is tanker shape and the wake field is wide so that the effective wake factor is lower and it gives 0.5428. EFD data are not available yet currently.

Table 5-1 Comparison of propulsive identities

	K_T	K_Q	$1 - t'$	$1 - w$
Without Rudder				
EFD	0.19493	0.026604		
CFD	0.1985	0.022096		
With Rudder				
EFD	0.198303	0.022821		
CFD	0.2031	0.02216	0.794	0.5428

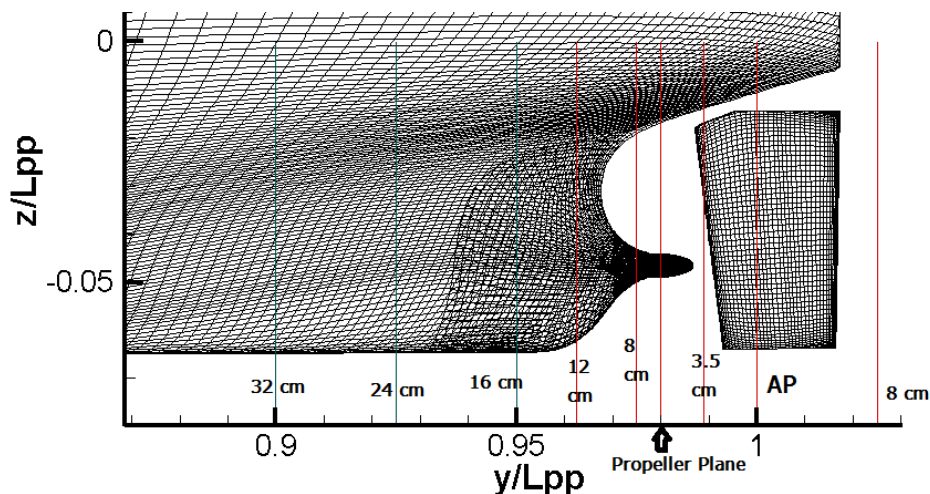


Figure 5-2 Positions of the measurements

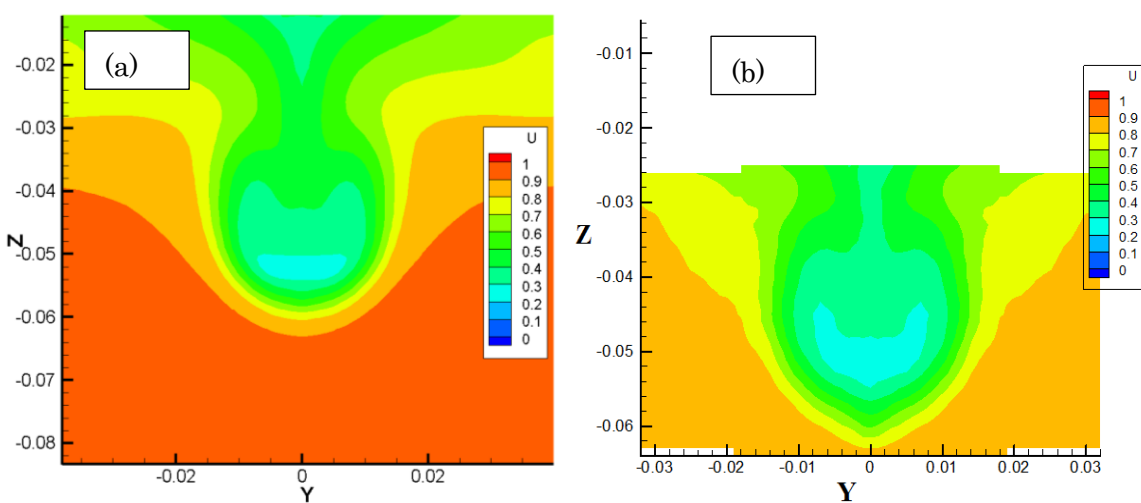
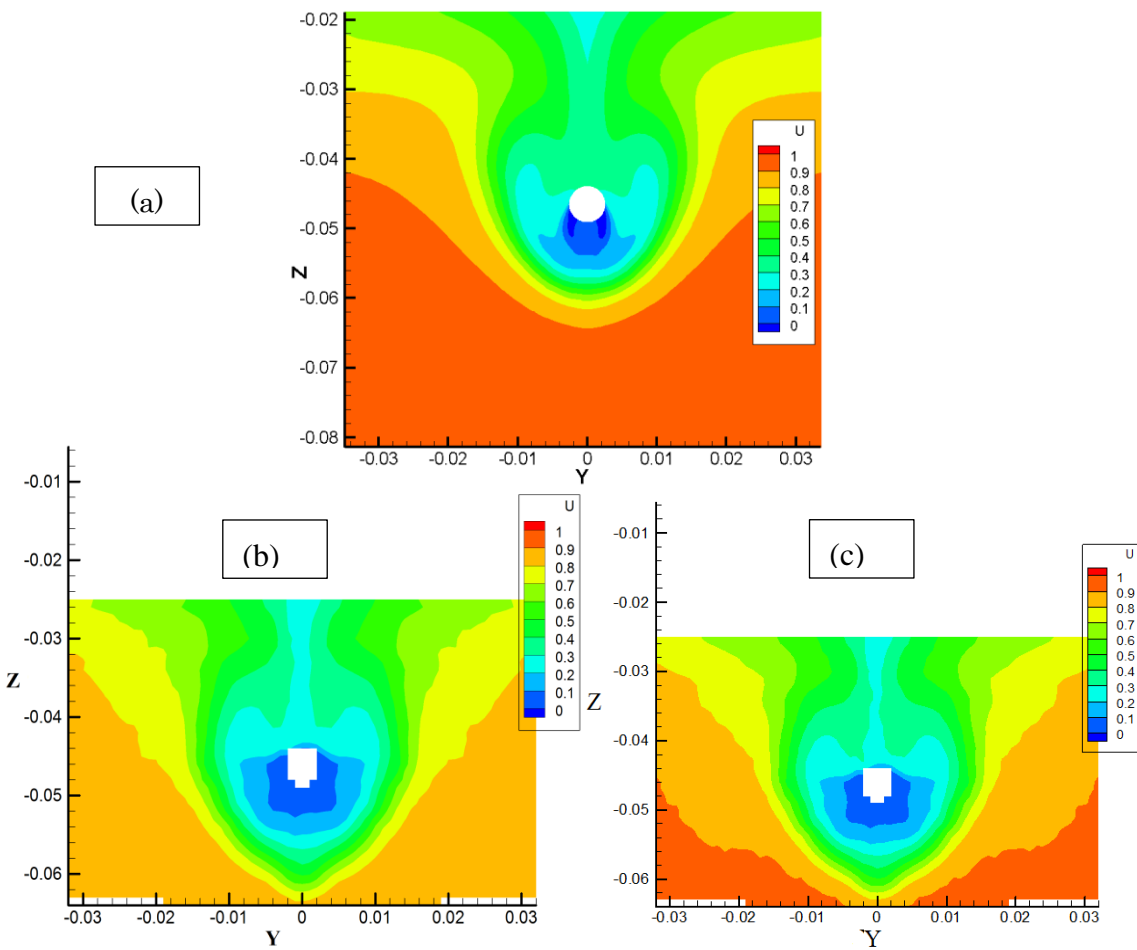
The experiments were carried out two times in different seasons by the PIV

measurements as a captive test. The propeller revolution rate is set at the self-propulsion point of the model with 16.5 rps with full load condition and with 11.1 rps for the ship point. In EFD, the laser position to measure the flow field is set at several specific locations and the computation flow field is extracted at the same sections. The information of the location where measurement was taken is shown in Figure 5-2 in non-dimensional form where the stations in red line will be compared with EFD and discussed in this chapter while the stations in dark green will be illustrated in Appendix B for references. According to the measurement of the model, the propeller plane is located at $X=0.98$ and AP is at $X=1$. The other locations are 12 cm forward of AP, 7.6 cm forward of AP, 3.5 cm forward of AP and 8 cm aft of AP. The solutions at these sections will be mainly discussed in this chapter.

5.2 NOMINAL WAKE FIELD ANALYSES

The bare hull computation without propeller is carried out first to understand the nominal wake field. It should be noted that in the experiment, the rudder and propeller are not fitted for this case but the dummy boss cap is fitted and the computation is carried out in the same condition. The computation of local flow predictions for KVLCC2 model has been evaluated by many institutes and the evaluation has been carried out from many submitted papers in the Gothenburg 2010 workshop on CFD in Hydrodynamics. In this case, the laser measurement is located at 5.6 cm forward of AP ($X=0.9825$) and at AP ($X=1$) and the computational flow field is extracted at these stations. The comparisons between CFD and 1st EFD data are shown in Figure 5-3 and Figure 5-4.

By referring to the several results published in the Gothenburg 2010 workshop assessment (Lars Larsson et al., 2010) using SHIPFLOW 4.3 by CHALMERS, FLUENT6.3.26 by MARIC, SURF by NMRI, NavyFOAM by NSWCCD-ARLUM and even using the same computation code CFDSSHIP-IOWA V4.0 by IIHR, the current computation gives a very good agreement. For $X=0.9825$ section, the hook-shape of iso-axial velocity contours is well produced which is very similar to other computation results. However, the flow field of EFD is a bit different and it is lower than the computation with clear difference at the highest contour level colors. This is because the model speed is changed slightly while the experiment is carried out and it is said that the current solution can be corrected and the corrected flow field will be like Figure 5-3 (c). The corrected flow field has good agreement with the computation. The comparison of nominal wakes at AP is shown in Figure 5-4 with original EFD data. Here also, the original EFD result is lower than the computation. The issue of EFD correction will be discussed in Section 5.6 again. Although the propeller plane of KVLCC2 is considered to be located at $X=0.9825$, according to the model in Osaka University, it is actually located at $X=0.98$. The EFD measurement is not available at this station but for the computation, the station is important for the propeller model and it is illustrated in Figure 5-5. For the upstream part of the propeller, the laser measurement at the station $X=0.975$ is available and the comparison is shown in Figure 5-6. In both CFD and EFD, good agreements are achieved in the axial velocity flow field as well as cross-flow components. The patterns of each contour level are quite similar to each other and the two vortices could be observed on each side of the hub in both results. As the advantage of CFD, the detailed flow field where the laser could not capture in EFD could be revealed clearly.



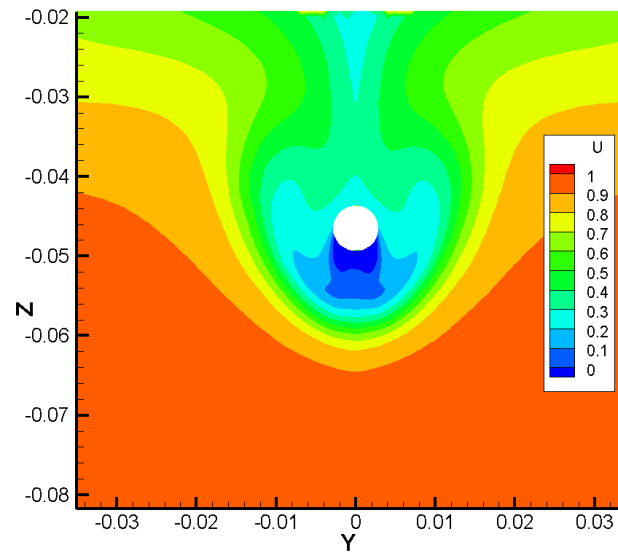
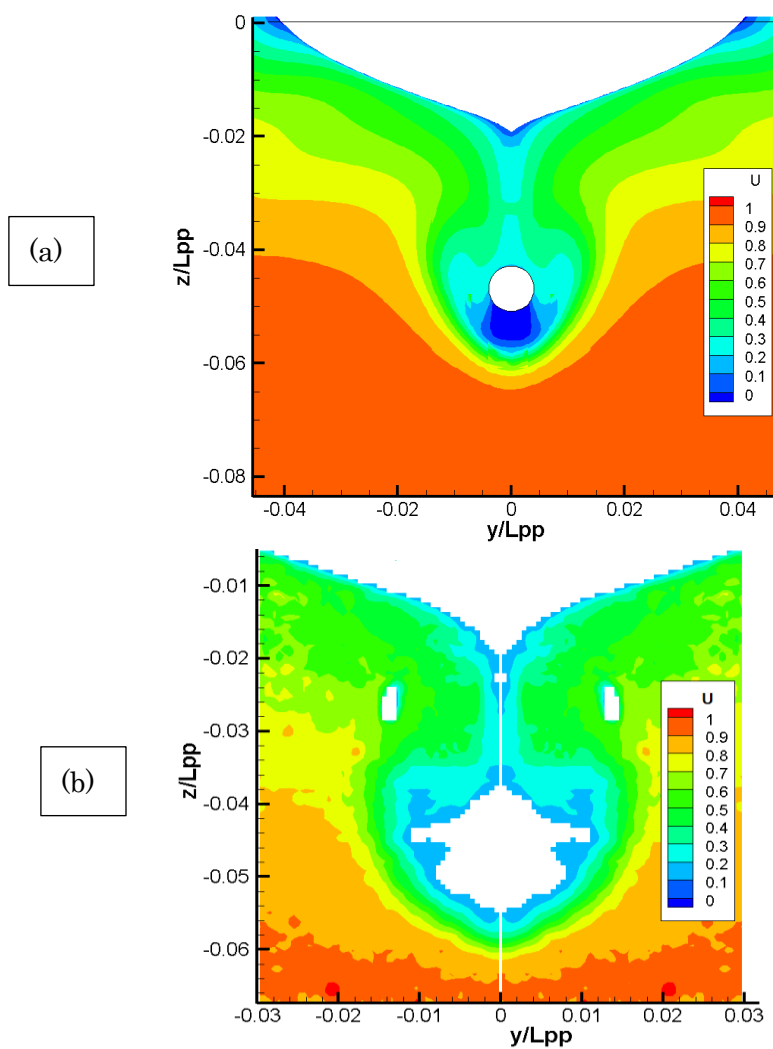


Figure 5-5 Computational output of the axial velocity layout at $X=0.98$



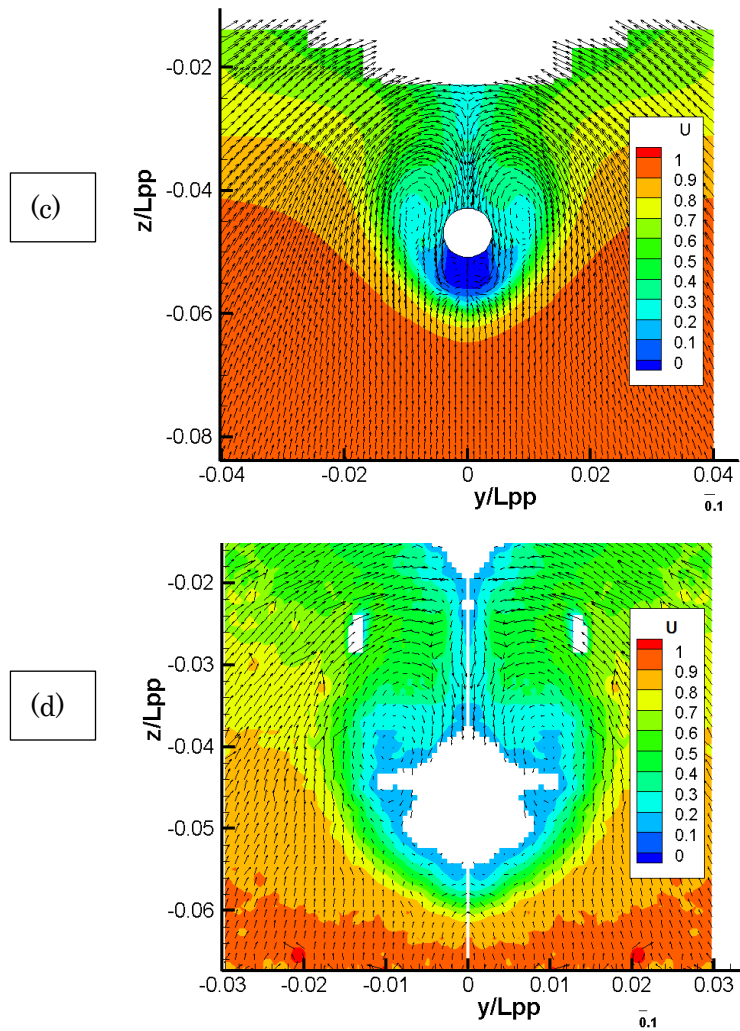


Figure 5-6 Comparison of axial velocity (a) CFD (b) EFD and cross-flow components (c) CFD (d) EFD at $X=0.9625$ section

5.3 WAKE FIELD ANALYSES AT THE MODEL POINT

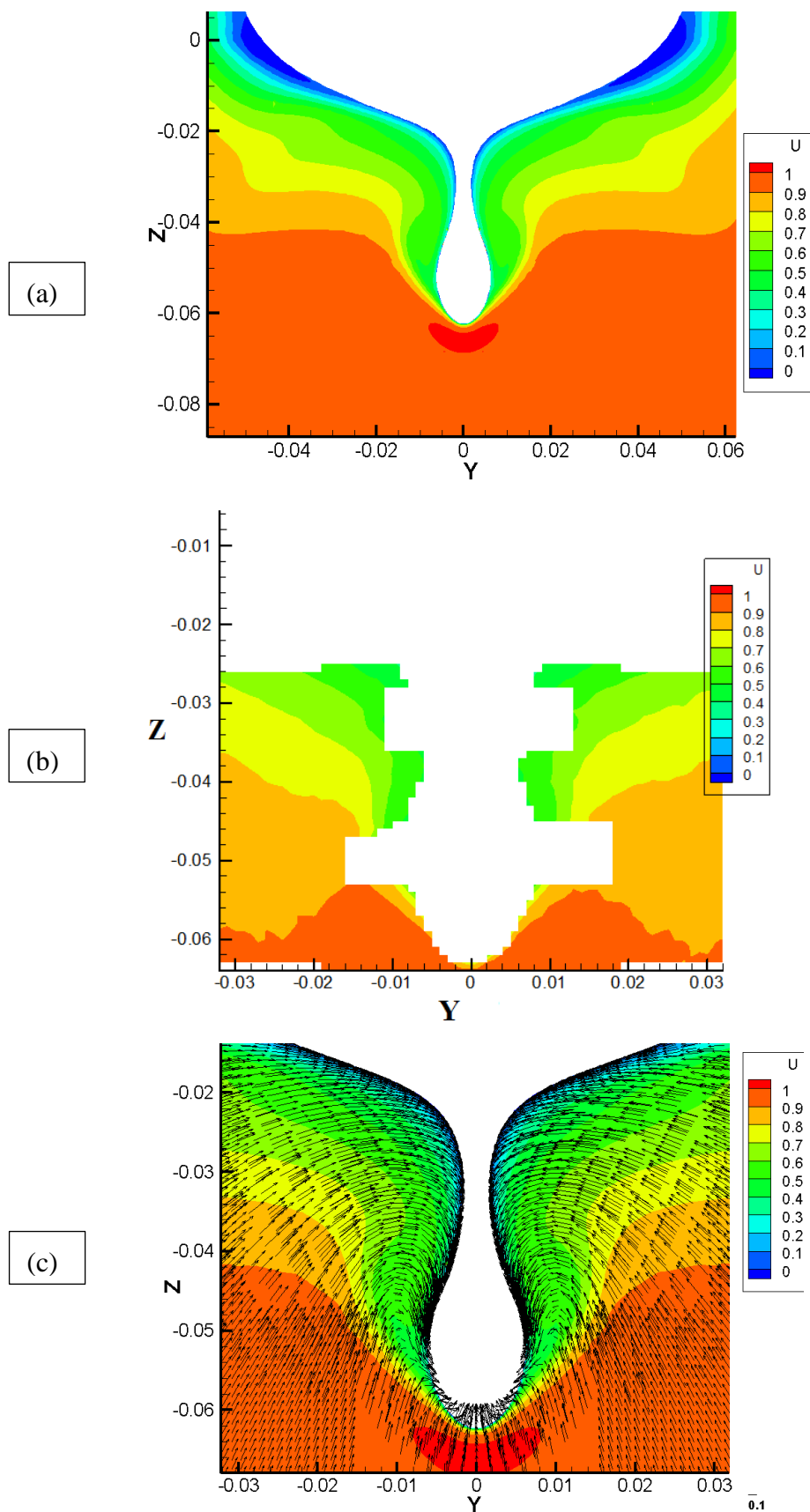
5.3.1 Without-rudder case

For the wake behind the rotating propeller, the rudder is not fitted at first and the computation is carried out with propeller only as the wake field is easier to analyze.

The propeller model used is explained in section 2.4. KVLCC2 propeller has variable pitch and the pitch distribution is shown in Figure 2-6. The three sections are analyzed for this case; 12 cm forward of AP (Figure 5-7), 3.5 cm forward of AP (Figure 5-8) and AP (Figure 5-9).

In all of these illustrations, the axial velocity field patterns are generally very similar to the experimental results. In EFD, some of the white parts are where the laser cannot catch the flow field. For the section 12 cm forward of AP ($X=0.9625$) which is the upstream part of the propeller, the computation generally gives good agreement. The highest contour level 1 below the hull can be seen in the CFD but not in EFD. And the contour level 0.9 pattern becomes different in the far more region from the center line ($Y=0$). The comparison of section 3.5 cm forward of AP ($X=0.9890625$) which is the downstream part of the propeller is shown in Figure 5-8. The contour patterns are in good agreements between the two solutions but, EFD gives higher velocity fields while CFD is low in terms of highest contour level. EFD has the highest contour level 1.6 with much wider area and CFD has only level 1.5 with narrower space. Moreover, in CFD, the lowest contour level 0 can be observed at the shaft center line ($Z=-0.04688$) which means there is no flow at that region which is not found in EFD. The cross-flow vectors are in similar patterns in both solutions.

For the flow field far more downstream of the propeller at $X=AP$, the similar case is observed that CFD is lower. In this case, EFD gives high accelerated contour level 1.6 for the full region of propeller disc but CFD still gives level 1.5 with lower values near the shaft center line. The cross-flow components got the same feature with similar shapes but with weaker vector length in CFD. It is not quite clear of the reason why CFD gives dissipated solutions which will be discussed in the next section.



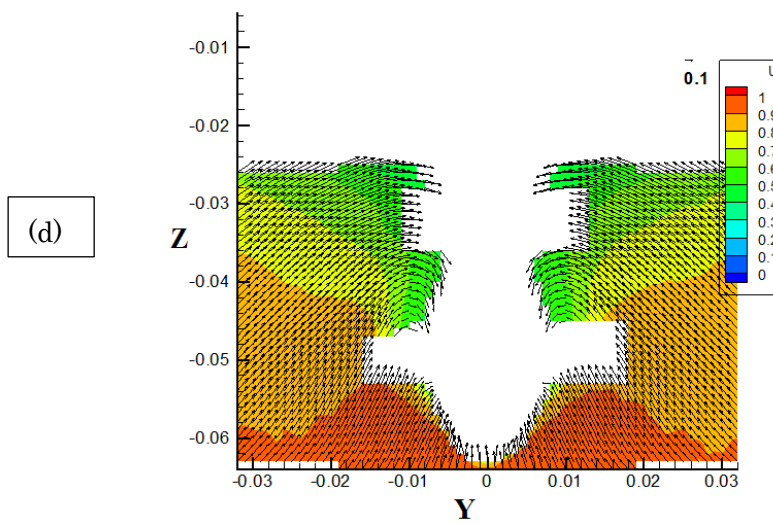
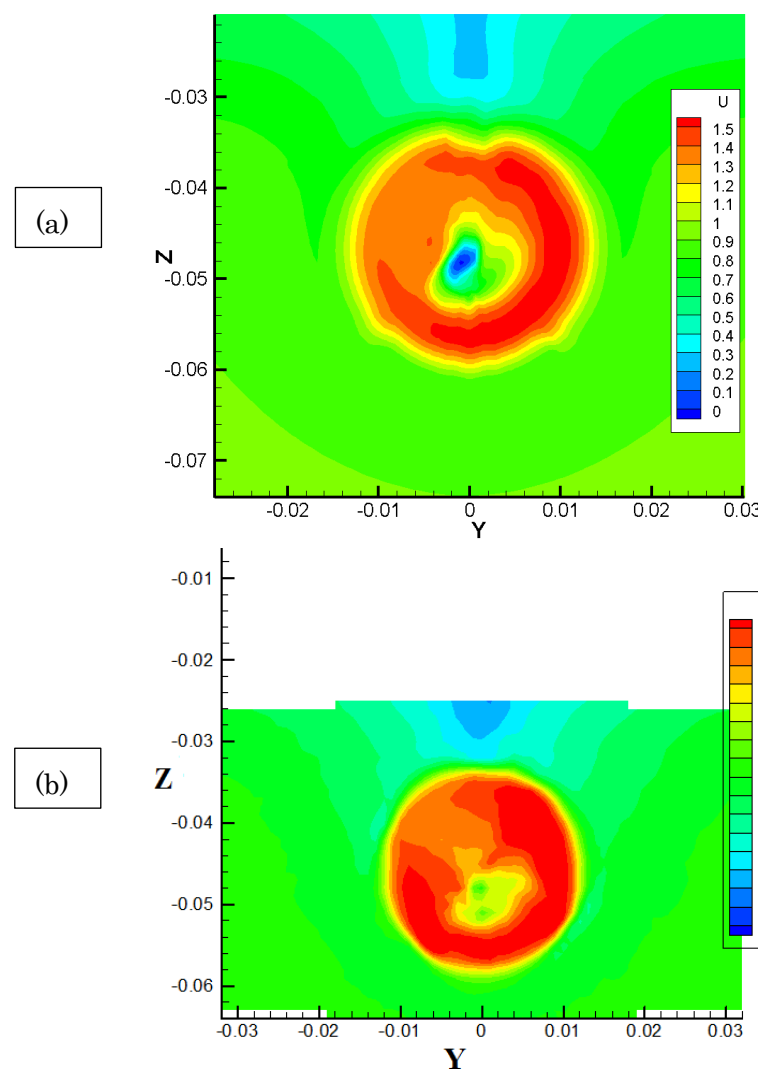


Figure 5-7 Comparison of axial velocity (a) CFD (b) EFD and cross-flow components (c) CFD (d) EFD at $X=0.975$ section for without-rudder case



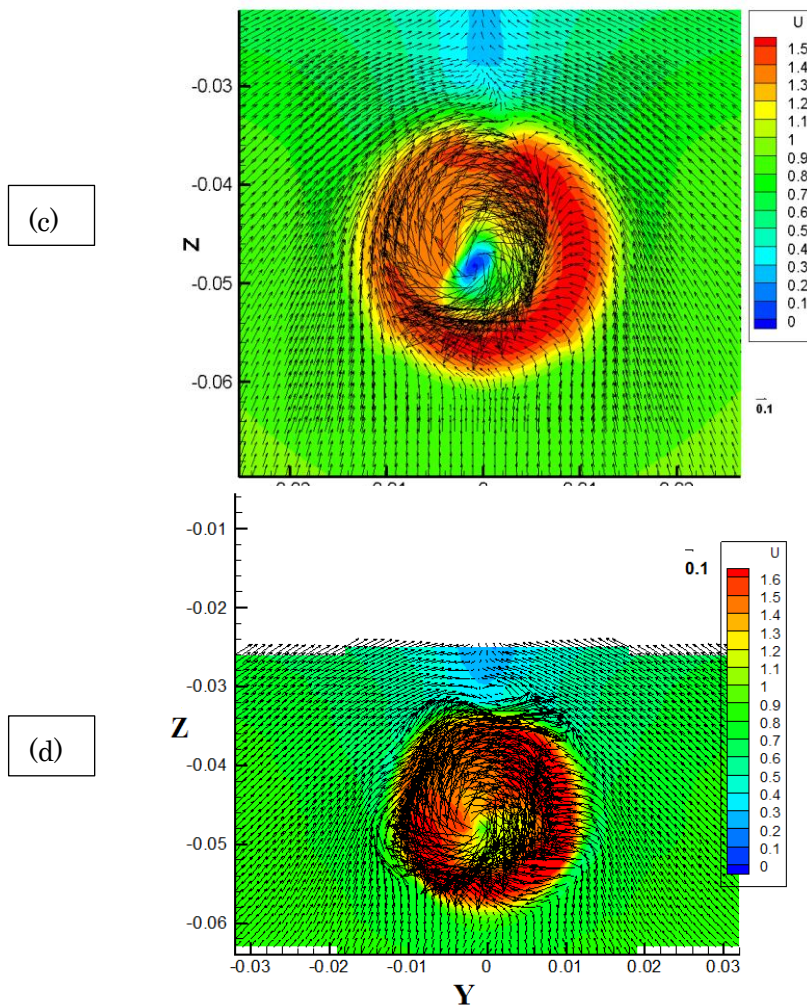
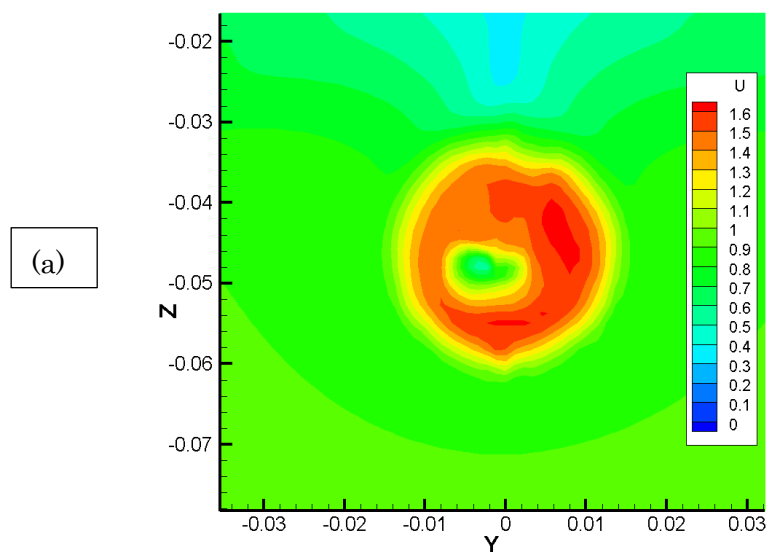


Figure 5-8 Comparison of axial velocity (a) CFD (b) EFD and cross-flow components (c) CFD (d) EFD at $X=0.9890625$ section for without-rudder case



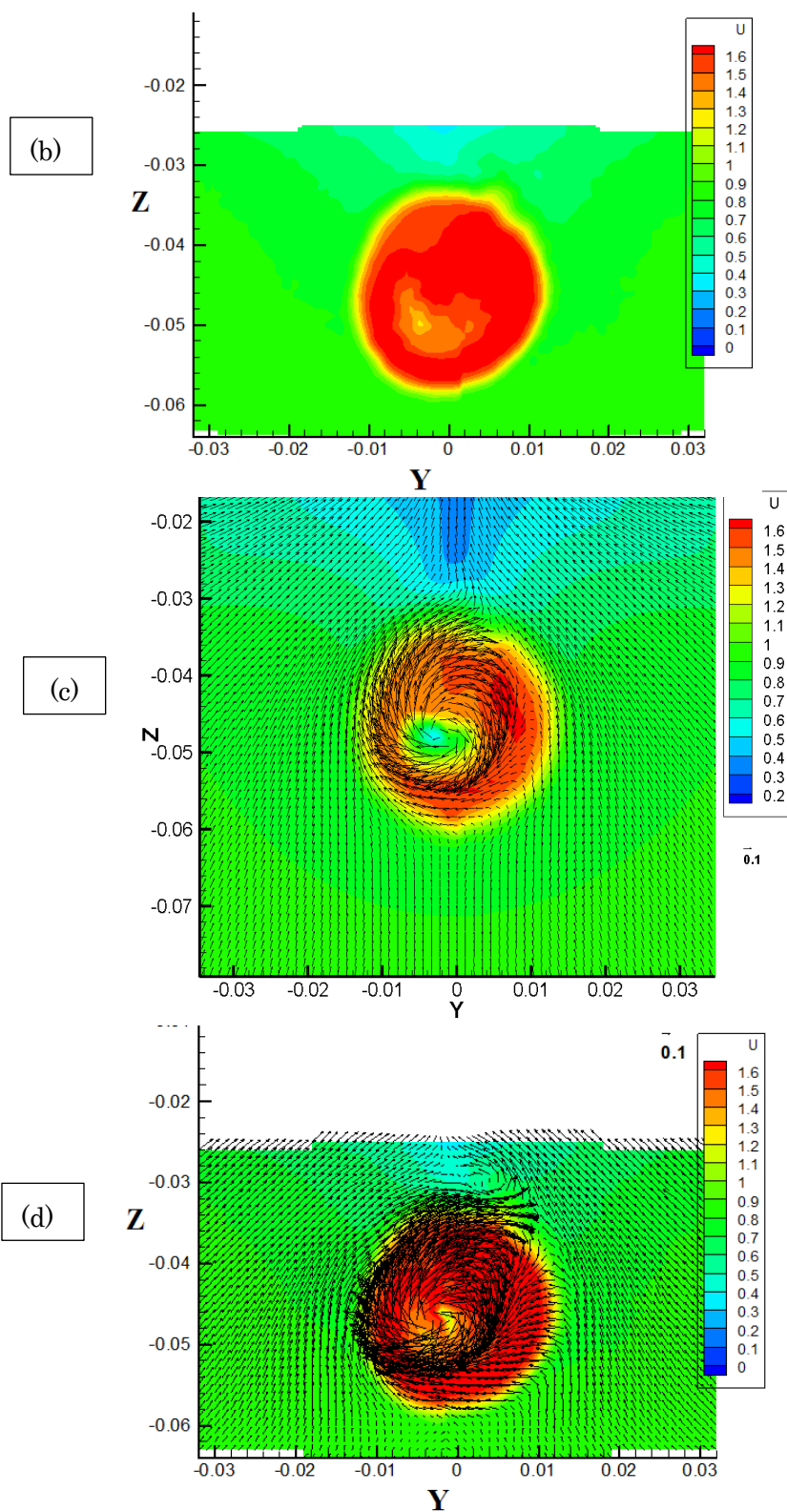


Figure 5-9 Comparison of axial velocity (a) CFD (b) EFD and cross-flow components (c) CFD (d) EFD at $X=1$ section for without-rudder case

5.3.2 With-rudder case

In this section, the rudder is fitted and the computation is repeated again. Here, only the normal rudder could be generated for the grid domain and the analyses will be based on this solution. The detailed information for the grid of rudder is explained in Section 2.3. As the main purpose of this research is to understand the behavior of the propeller theory, the rudder will be set at zero drift angle and no rudder forces will be accessed and discussed. For the analysis, totally 5 sections are selected to analyze the flow field; 12 cm forward of AP ($X=0.9625$), 8 cm forward of AP ($X=0.975$), 3.5 cm forward of AP ($X=0.9890625$), AP ($X=1$) and 8 cm aft of AP ($X=1.025$) and are illustrated from Figure 5-10 to Figure 5-14 respectively.

For the section $X=0.9625$, the same behavior with Section 5.3.1 is observed that the EFD data without correction is somewhat lower than the CFD solution especially for the highest contour level. But for the section $X=0.975$, the EFD results of the second time experimental data is used and good agreements are observed (the experiments are carried out two times of which only section 0.975 data are available for the model point from the second EFD results and all EFD data for other stations are taken from the original data). The trends of each contour level are quite similar and the cross-flow components give same patterns with similar strength. For the position $X=0.9890625$ which is just next the propeller plane on the downstream part, the axial velocity contour shapes are much close to each other. There is some rudder part for this position that can be seen as the white part in CFD and the laser cannot measure the data for that part in EFD. Similar to the without-rudder case, the highest contour level of CFD is one step lower than EFD and the lowest velocity profile is captured at the shaft center

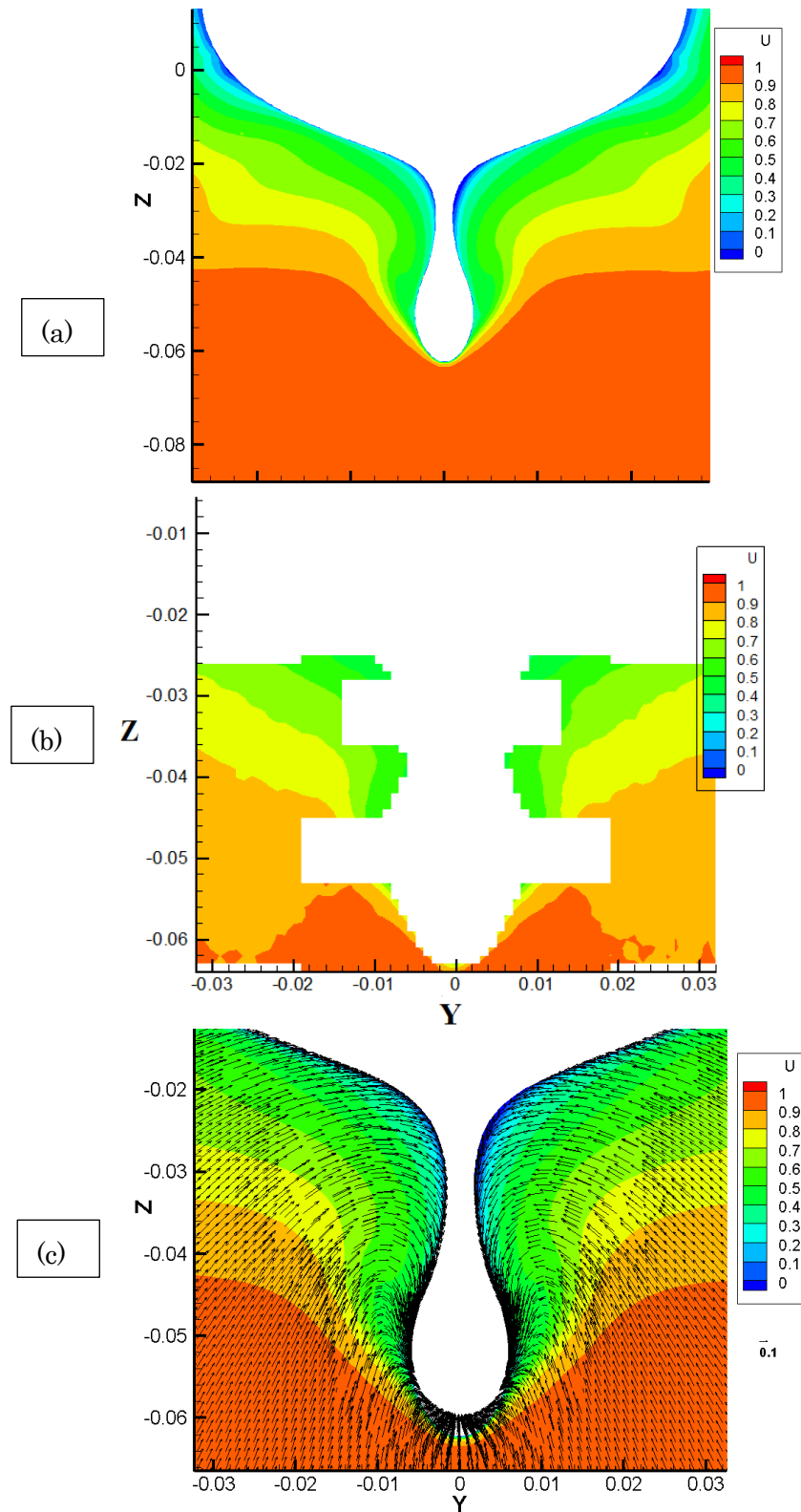
line position in CFD.

At the aft perpendicular position (AP), a very good agreement is achieved in terms of the shape. CFD can capture more detailed flow field near the rudder surface and EFD cannot capture in that place. The vortex can be seen on the port side of the rudder in CFD which makes sense for the right-handed propeller. The cross-flow components structures of the two results are also close enough. For the complete comparison, another far downstream section is selected at $X=1.025$ where the EFD can give full flow field layout. Again the two solutions give close layout where the vortex can be seen and its position which is shifted a bit to the left side of the center line ($Y=0$) is exactly identical in both solutions. But, the flow field of CFD is lower with weaker corresponding cross-flow components than EFD that is the main weak point of the computation for this tanker model.

For the better understanding, the far downstream section which is the position, where the effect of combined flow field from the hull, propeller and rudder can be observed, is analyzed at each vertical position ($Z=-0.03, -0.035, -0.04, -0.045, -0.05, -0.055$ and -0.06) and the comparison is made between CFD and EFD and illustrated in Figure 5-15. In each figure from Figure 5-15 (b) to Figure 5-15 (h), the patterns are much close between the two solutions with comparatively lower results of CFD. This figure clearly confirms the dissipation of computation. Up to here, CFD gives much lower results in the comparison with the first experiment so that more assessments should be needed to compare with the second experiment that will be discussed in Section 5.4.

The surface pressure distribution is illustrated in Figure 5-16 which clearly shows the interaction between ship, propeller and rudder. The figure is drawn for the

computation with rudder. The high pressure field in without-propeller condition is reduced by the suction effect of propeller which is shown by the pressure difference.



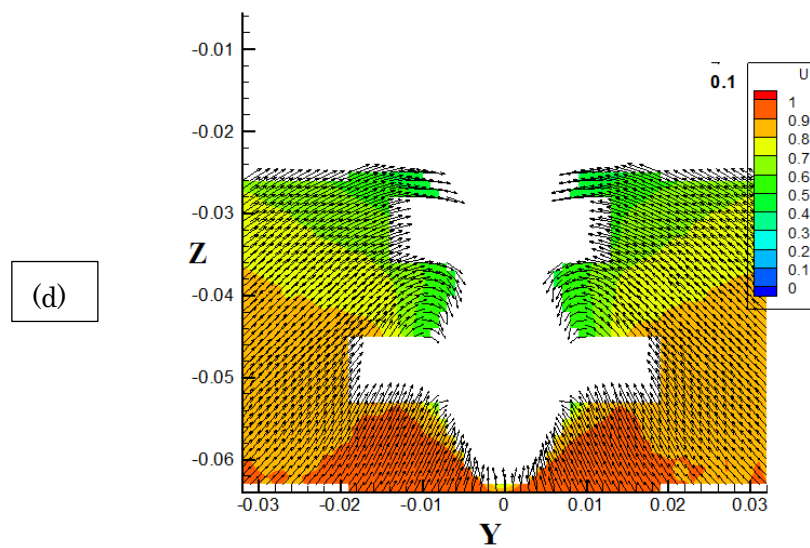
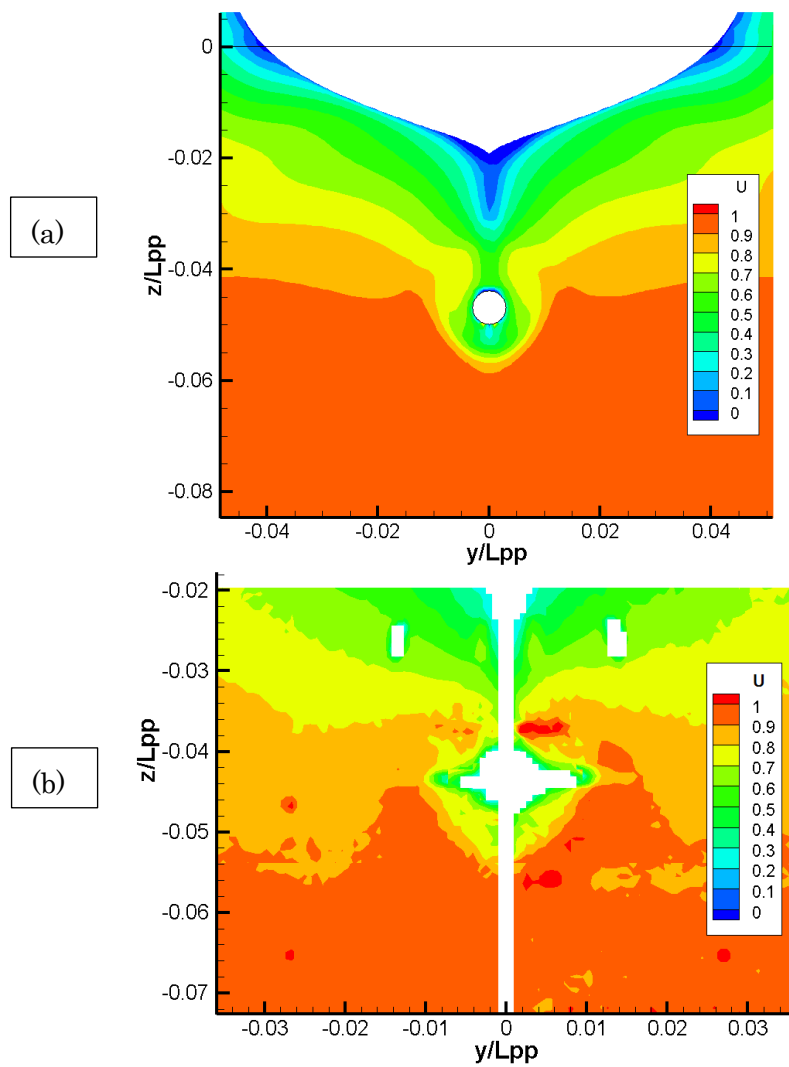


Figure 5-10 Comparison of Axial Velocity (a) CFD (b) EFD and cross-flow vectors (c) CFD (d) EFD at $X=0.9625$ for with-rudder case



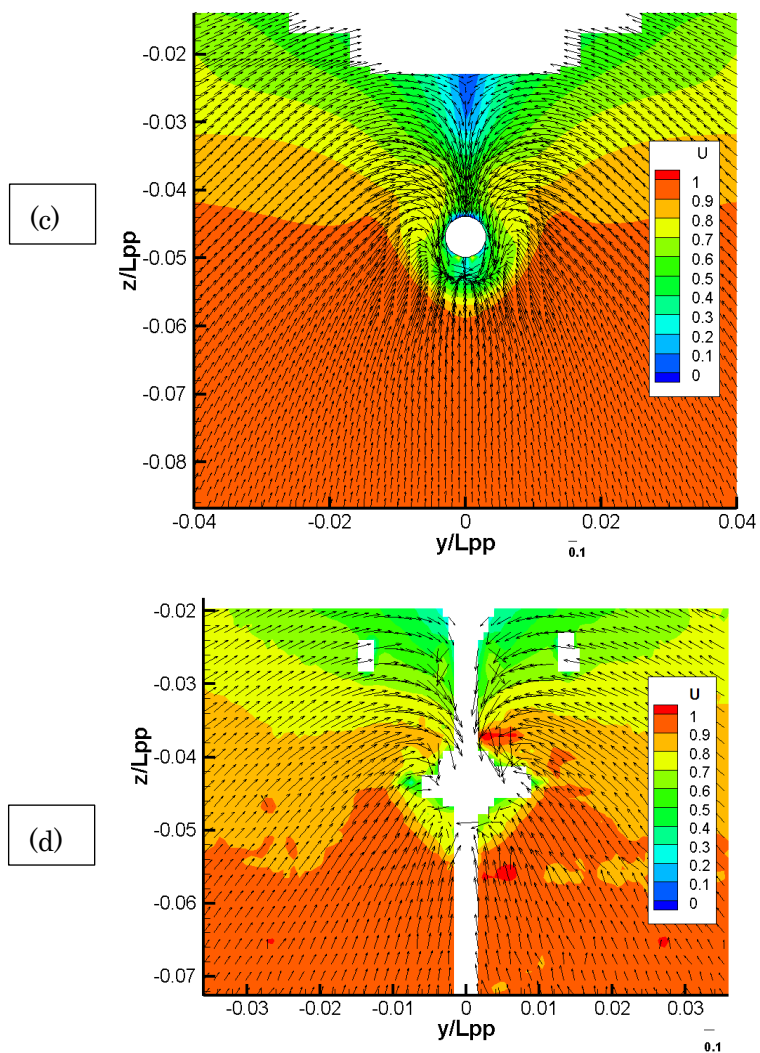
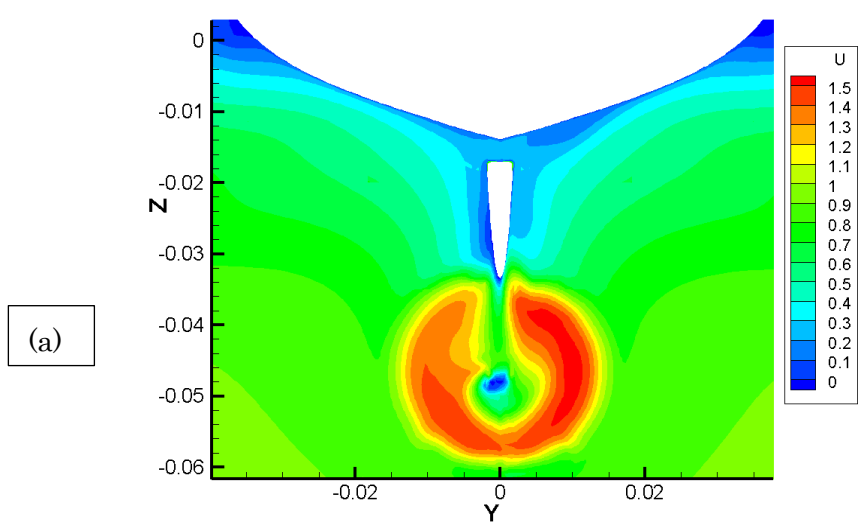


Figure 5-11 Comparison of Axial Velocity (a) CFD (b) EFD and cross-flow vectors (c) CFD (d) EFD at $X=0.97625$ for with-rudder case



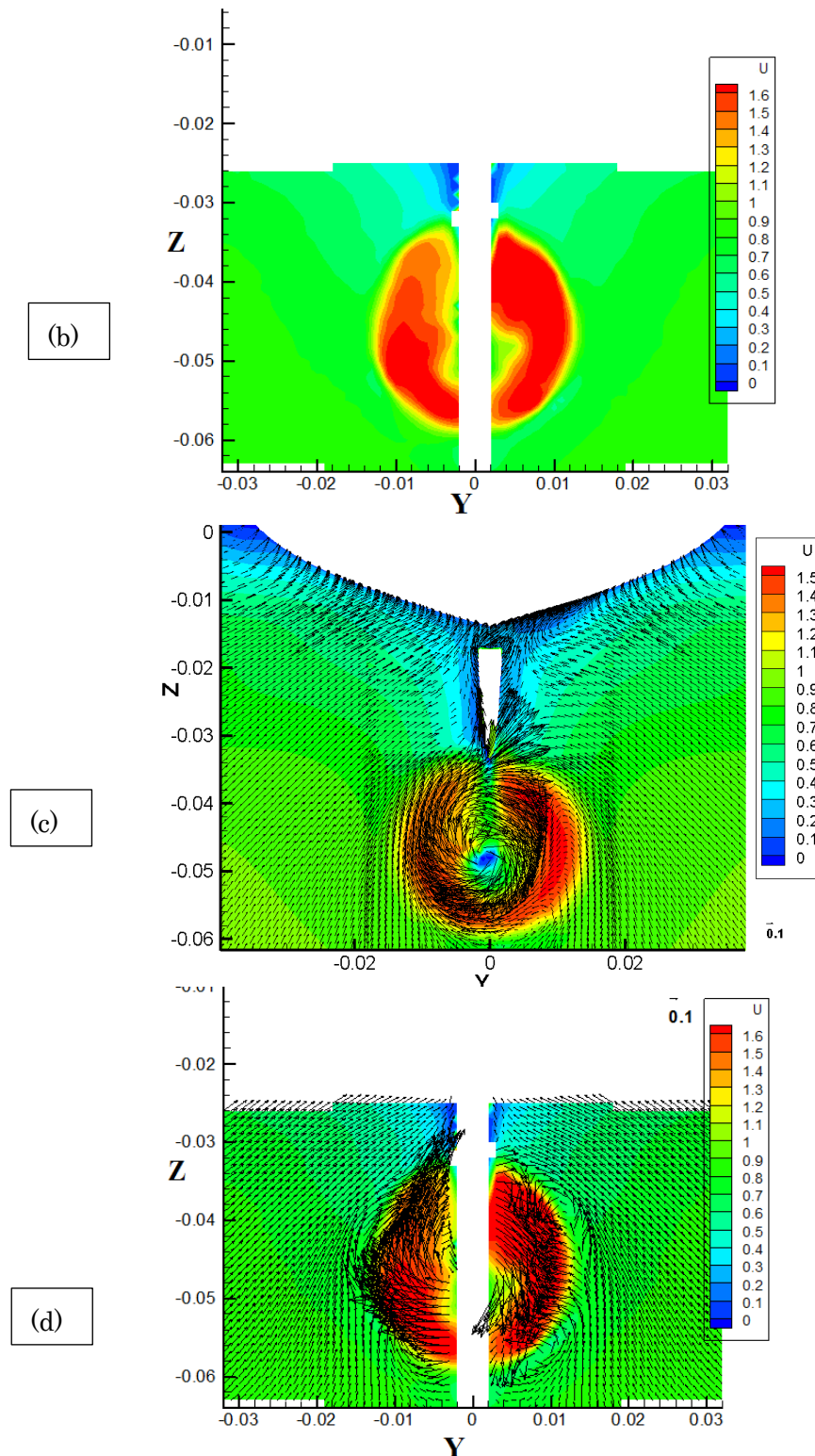
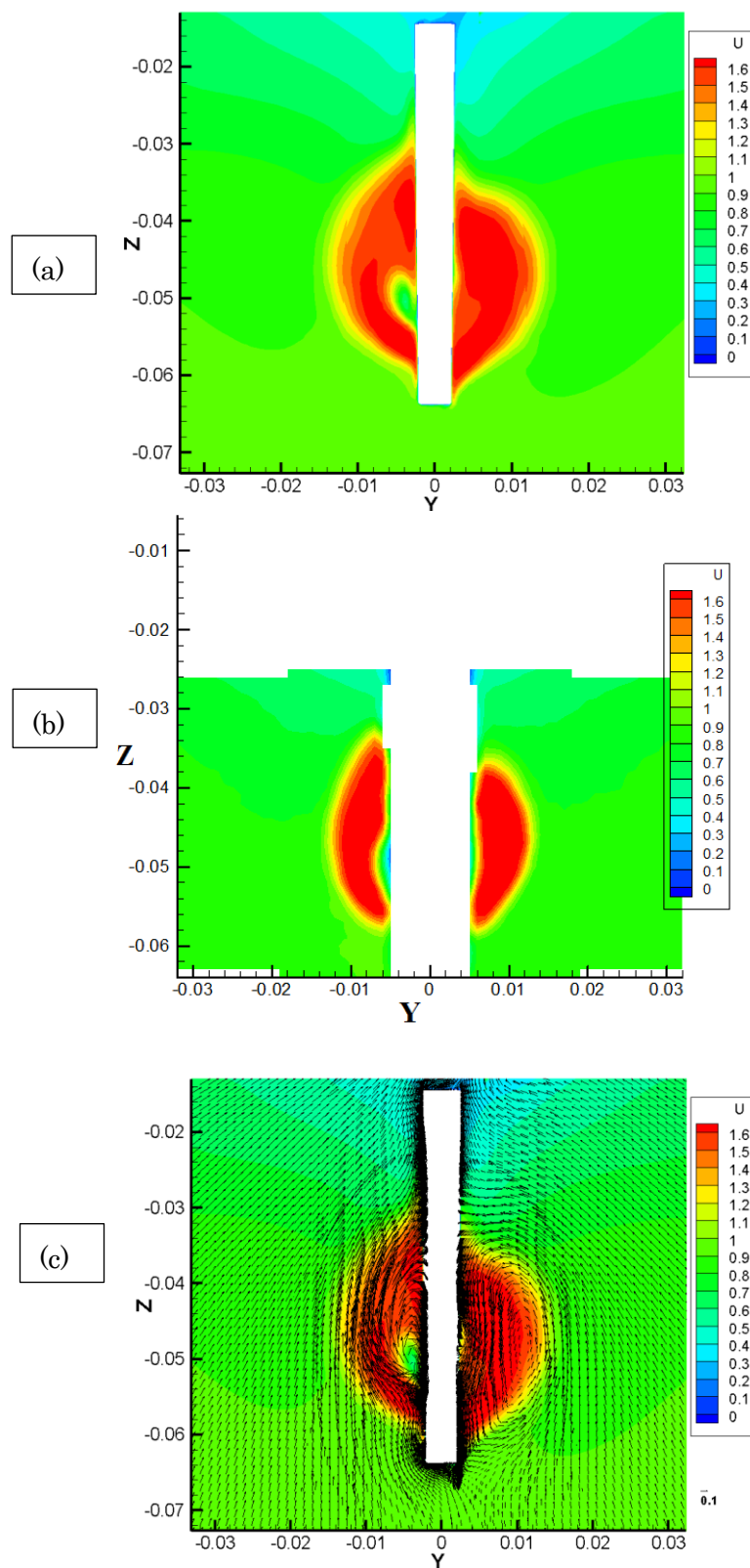


Figure 5-12 Comparison of Axial Velocity (a) CFD (b) EFD and cross-flow vectors (c) CFD (d) EFD at $X=0.9890625$ for with-rudder case



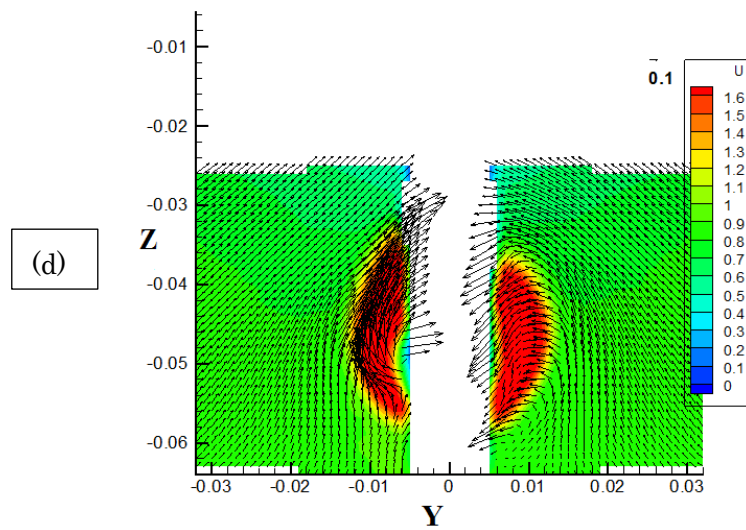
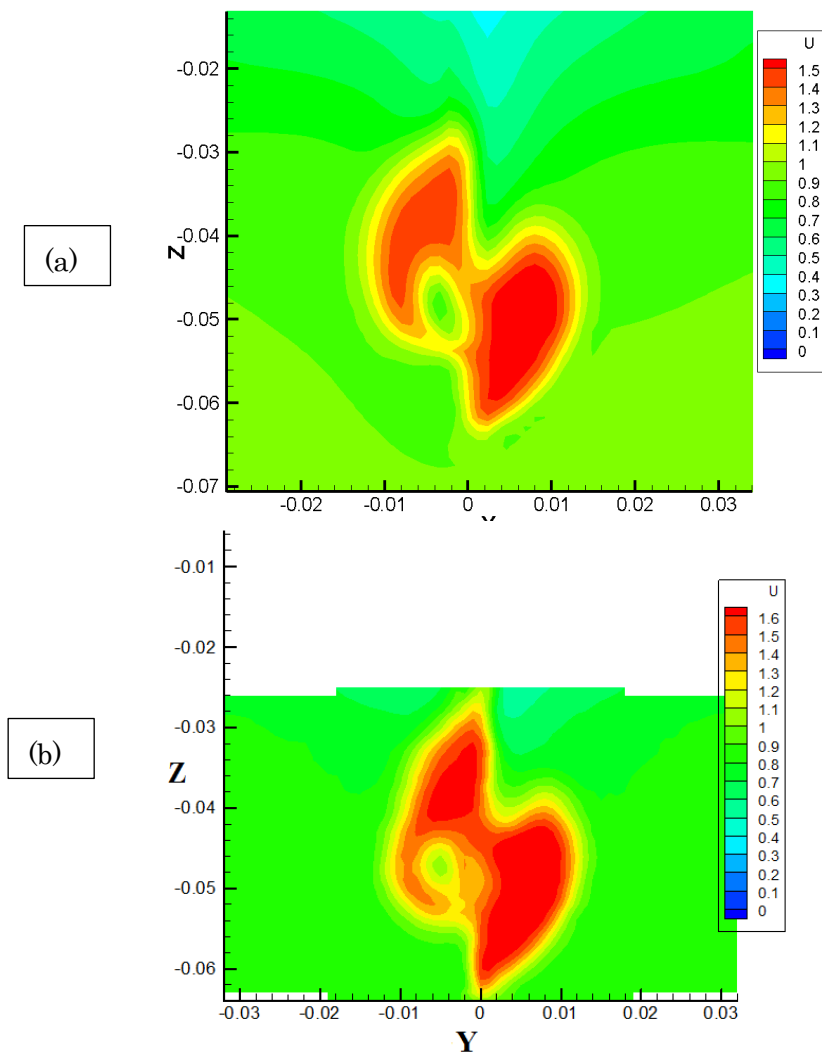


Figure 5-13 Comparison of Axial Velocity (a) CFD (b) EFD and cross-flow vectors (c) CFD (d) EFD at $X=1$ for with-rudder case



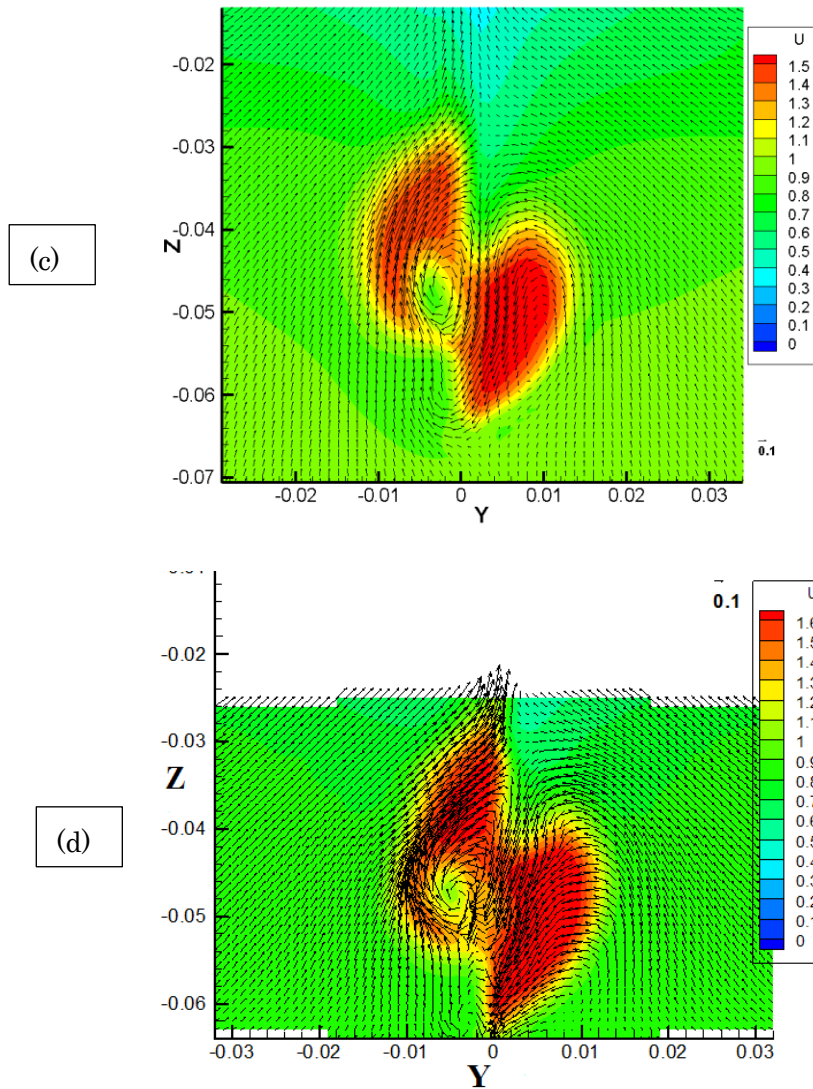
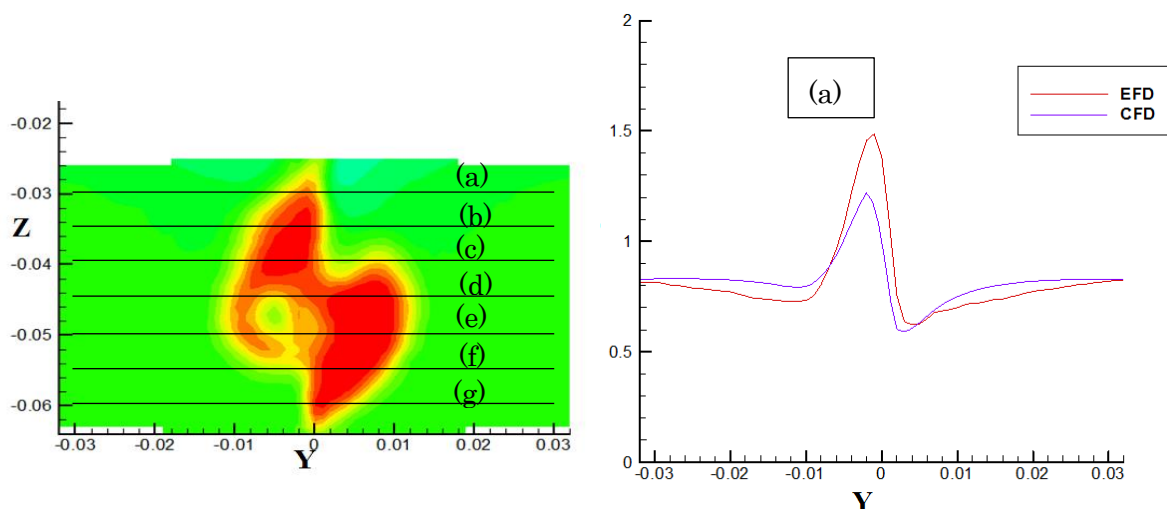


Figure 5-14 Comparison of Axial Velocity (a) CFD (b) EFD and cross-flow vectors (c) CFD (d) EFD at $X=1.025$ for with-rudder case



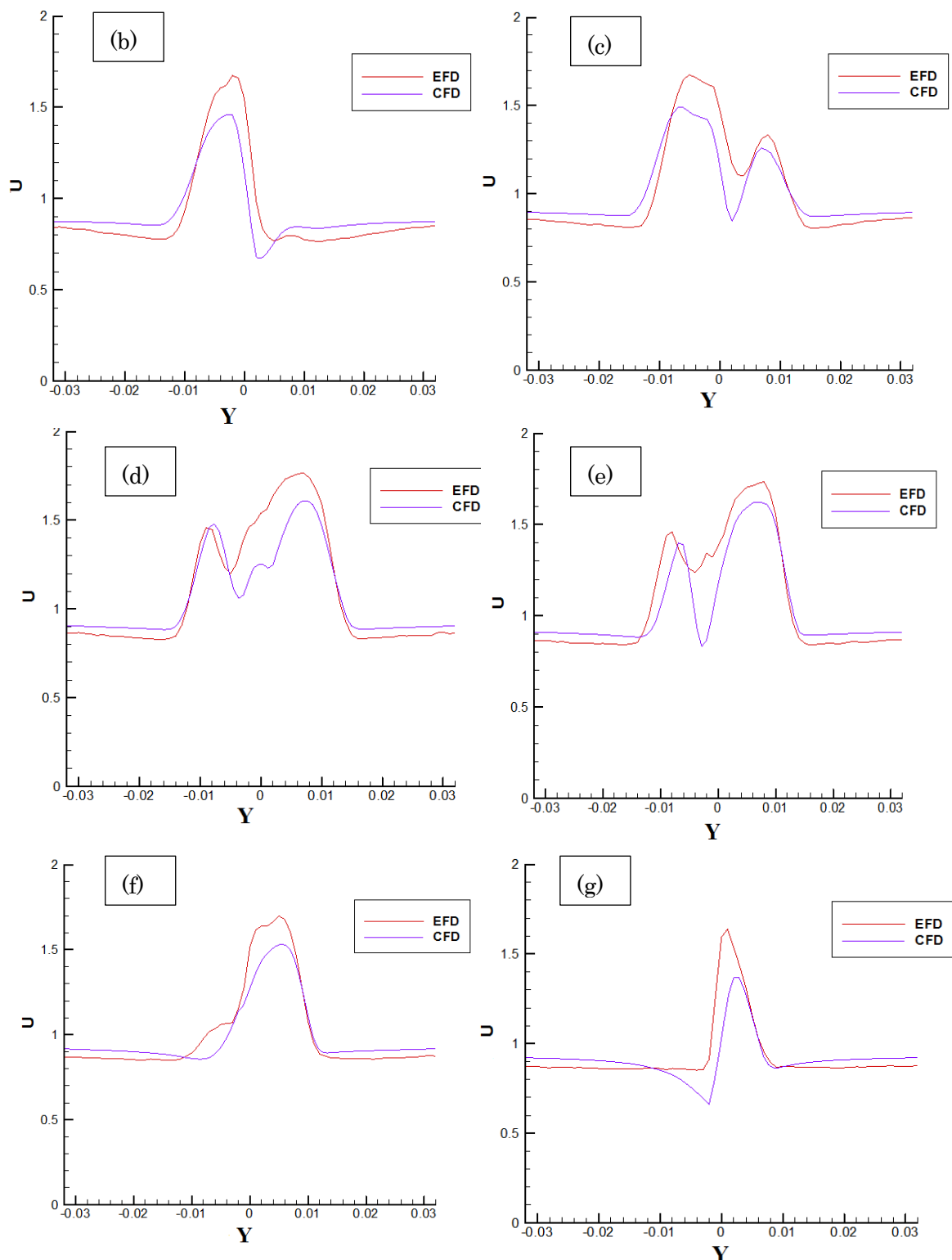


Figure 5-15 Comparison of axial velocity between CFD and EFD at $X=1.025$ for each vertical position (a) $Z=-0.03$ (b) $Z=-0.035$ (c) $Z=-0.04$ (d) $Z=-0.05$ (f) $Z=-0.055$ (g) $Z=-0.06$

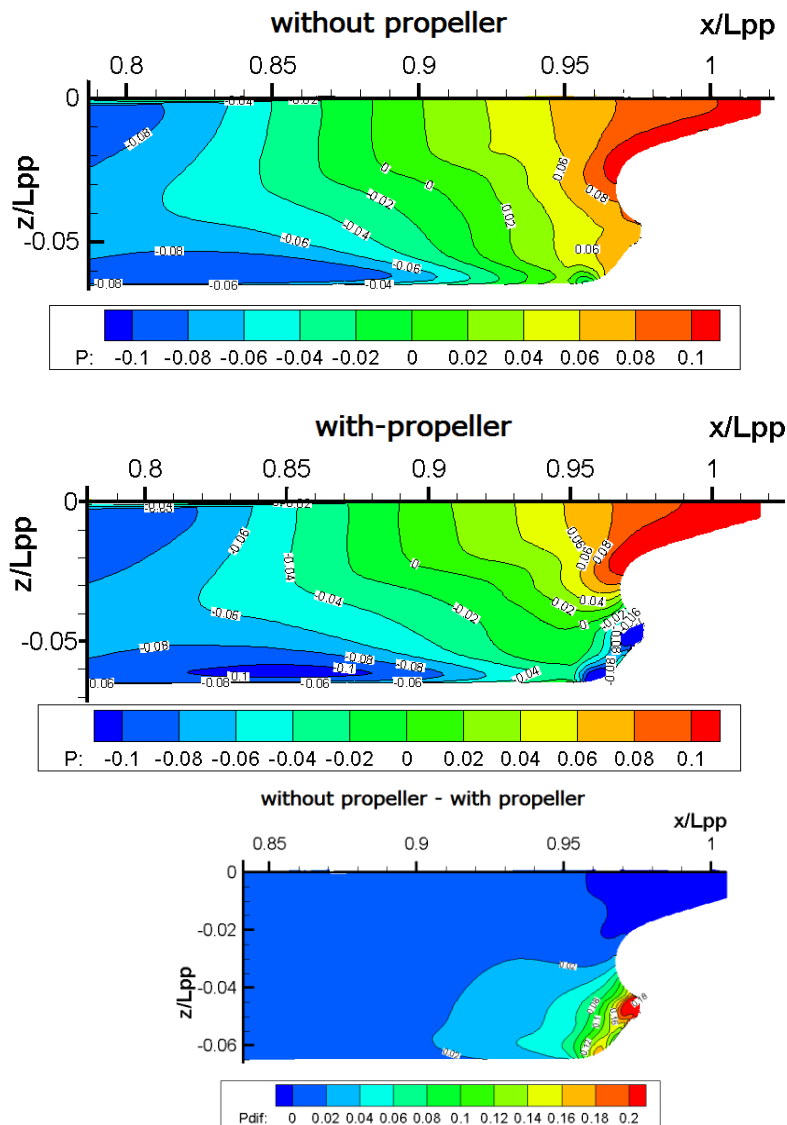


Figure 5-16 Surface pressure distribution of KVLCC2 for with-rudder case

5.4 WAKE FIELD ANALYSES AT THE SHIP POINT

In Section 5.3, the analysis is made for the model point and compared with first experiment. But, much of the flow fields are under predicted by the CFD than EFD.

So, it should be compared with the second EFD data but in the second time, the data are almost for the ship point and just for the with-rudder case so that the computation is set at lower rps for the ship point at 11.1 rps. And the flow fields are extracted at $X=1$, 1.01875, 1.025 and the comparisons are illustrated in Figure 5-17, 5-18, 5-19 and the discussions are focused on the results.

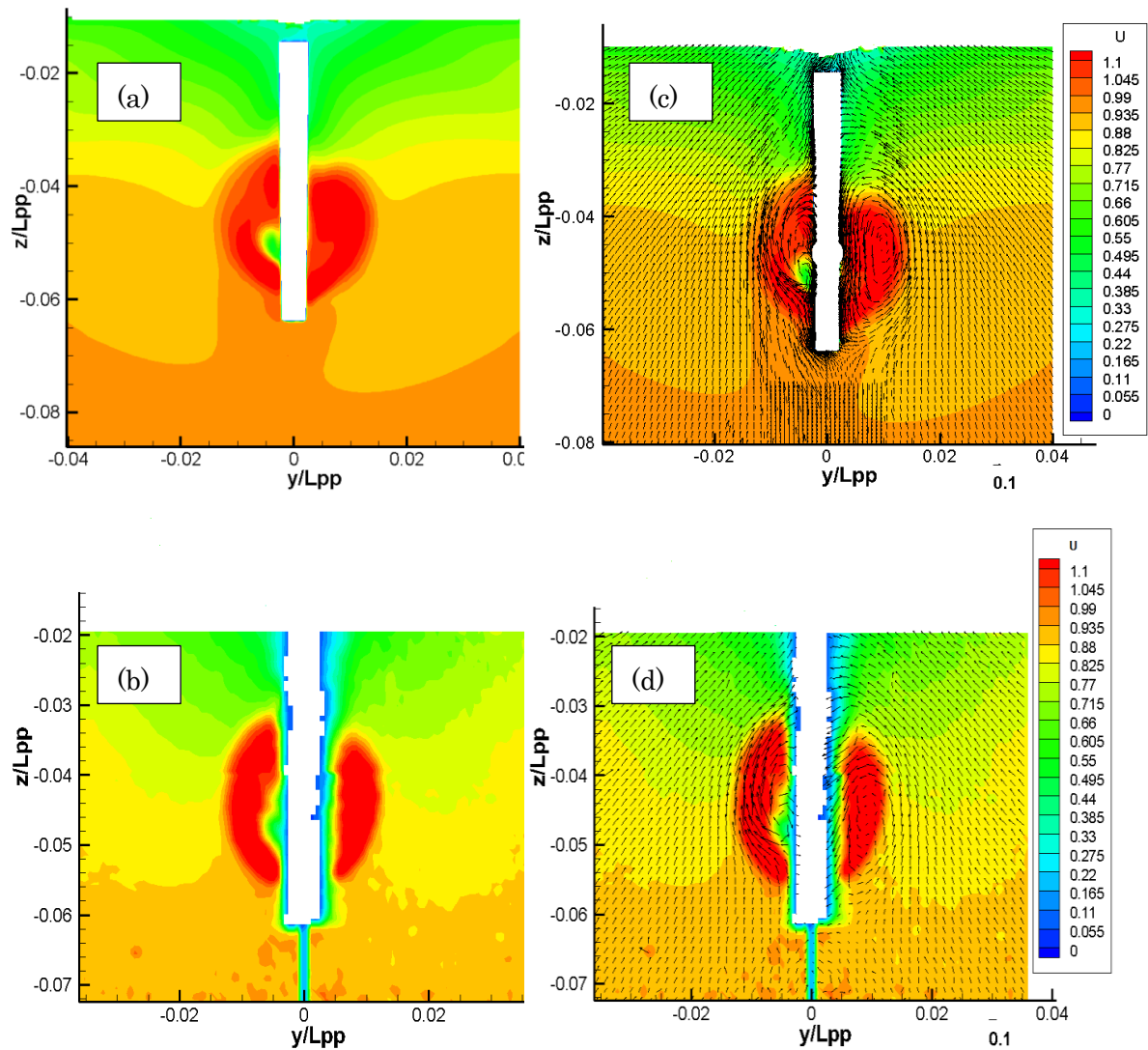


Figure 5-17 Comparison of Axial Velocity (a) CFD (b) EFD and cross-flow vectors (c) CFD (d) EFD at $X=1.0$ for with-rudder case at ship point

In Figure 5-17, 5-18 and 5-19, similar to Section 5.3, good agreements are obtained in both axial velocity profiles and cross-flow components. However, unlike the previous comparison, in this case, the highest contour level, 1.1 is same in both CFD and EFD result. The axial velocity profiles show CFD may be a little bit lower than EFD, but not as much as than the first experiment. The detailed comparison is made at $X=1.025$ for different Z locations and the good agreements are observed between CFD and EFD. So, in overall, it could be concluded that the computations give better agreement to the second experimental data.

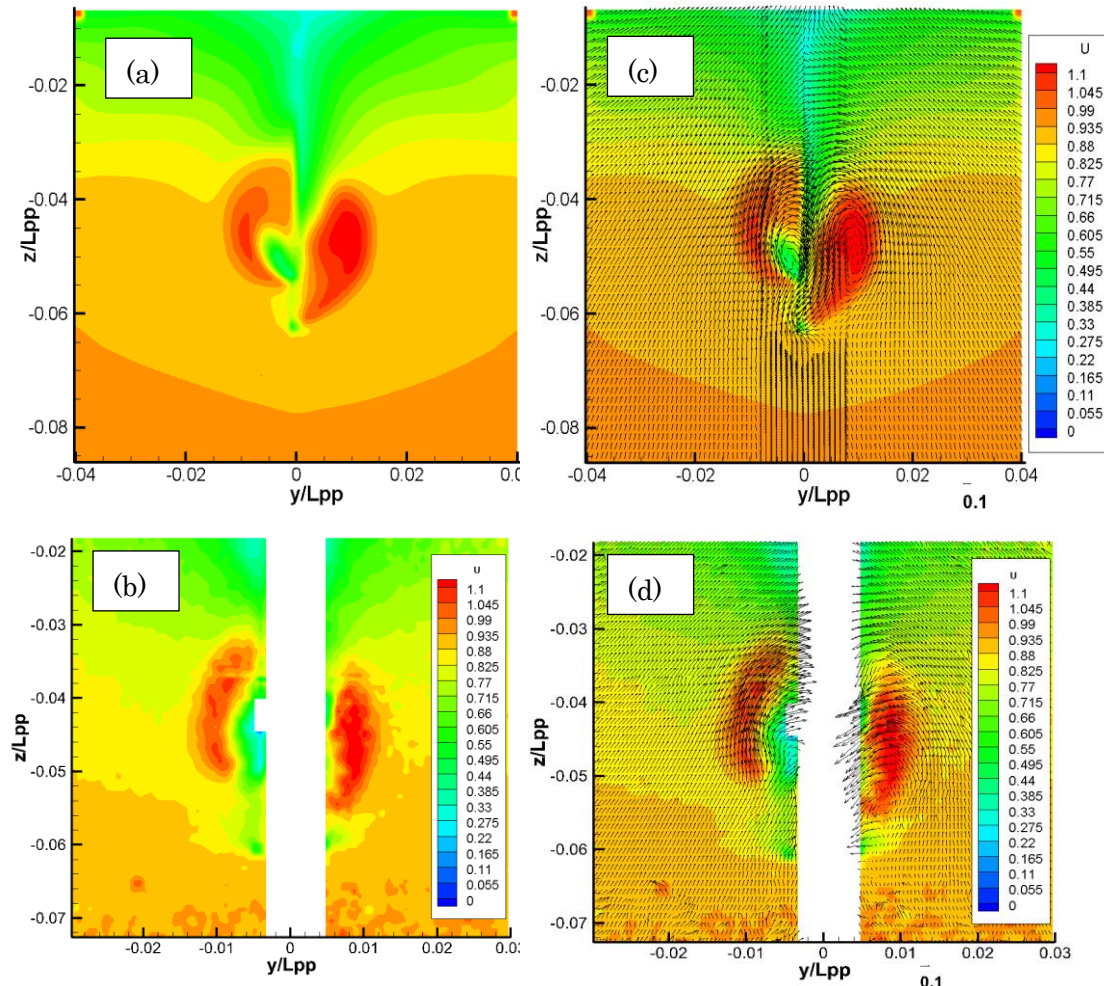


Figure 5-18 Comparison of Axial Velocity (a) CFD (b) EFD and cross-flow vectors (c) CFD (d) EFD at $X=1.01875$ for with-rudder case at ship point

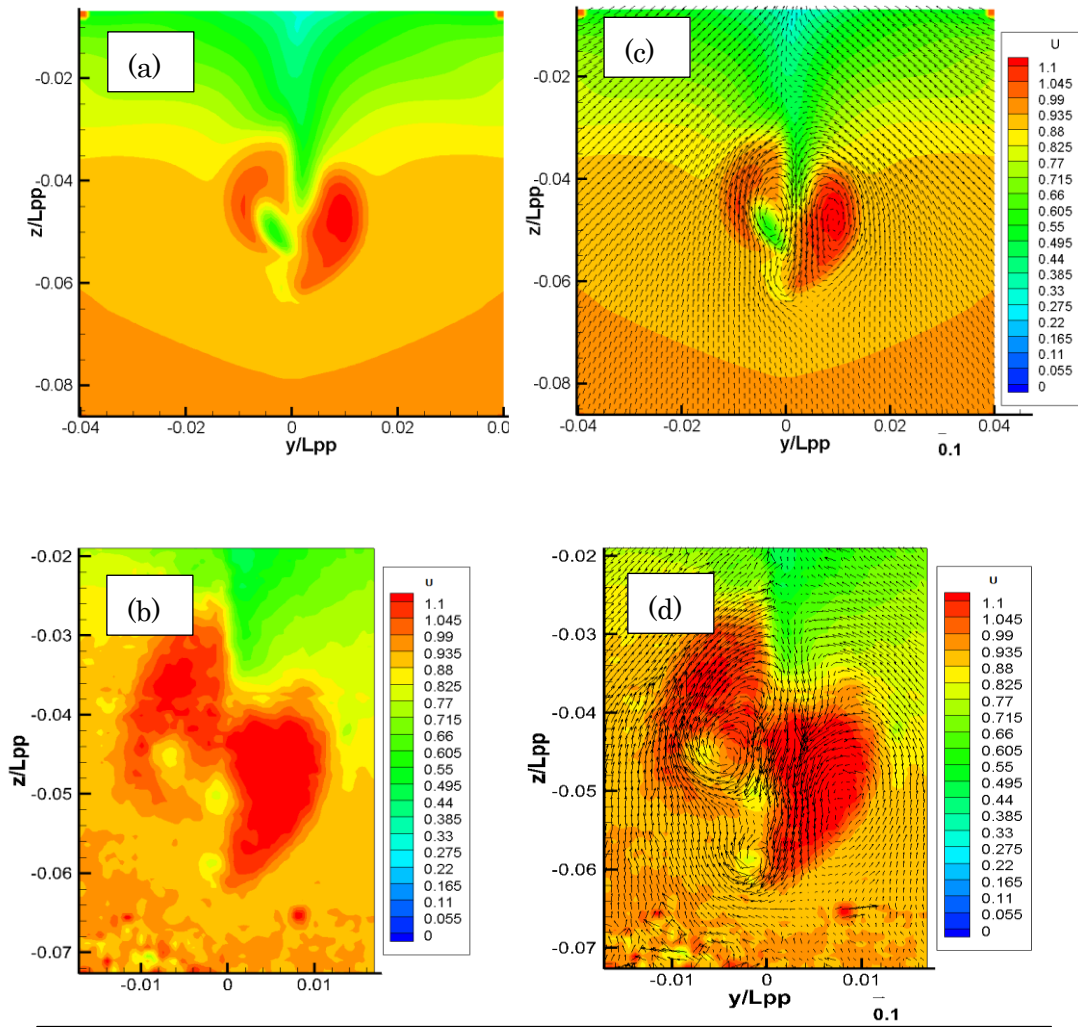
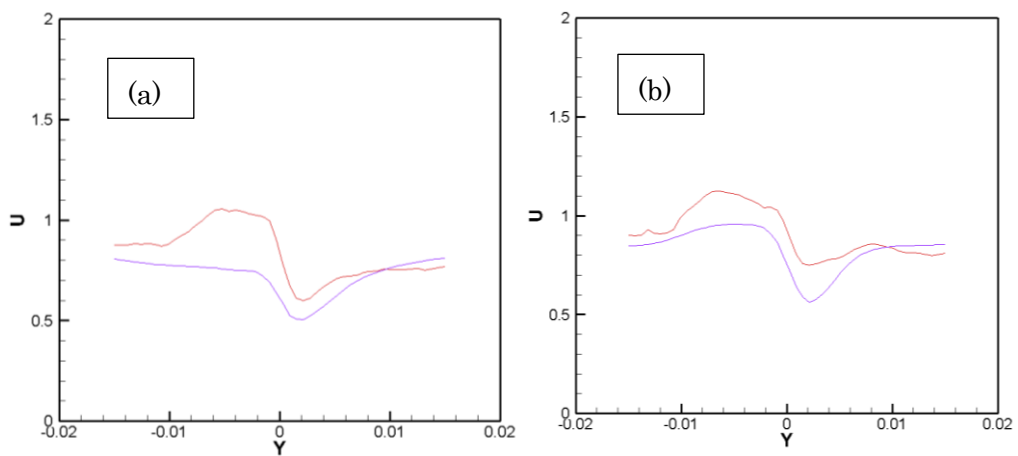


Figure 5-19 Comparison of Axial Velocity (a) CFD (b) EFD and cross-flow vectors (c) CFD (d) EFD at $X=1.01875$ for with-rudder case at ship point



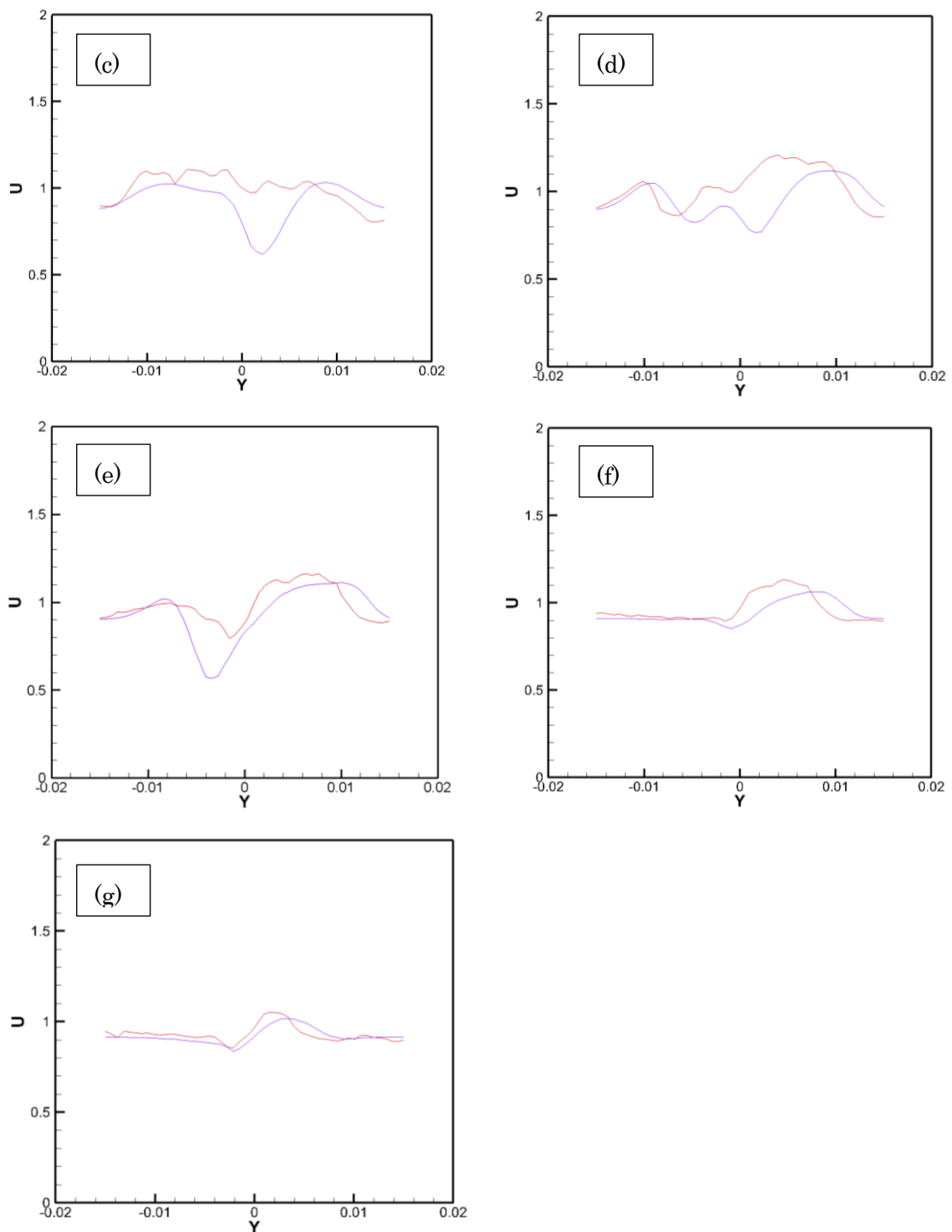


Figure 5-20 Comparison of axial velocity at ship point between CFD and EFD at $X=1.025$ for each vertical position (a) $Z=-0.03$ (b) $Z=-0.035$ (c) $Z=-0.04$ (d) $Z=-0.05$ (f) $Z=-0.055$ (g) $Z=-0.06$

5.5 COMPARISON WITH REAL GEOMETRY PROPELLER COMPUTATION AND OTHER BODY-FORCE PROPELLER MODELS

The capability of propeller model has been computed and validated with two sets of EFD. Because of the inconsistent agreements between first and second experiments, the computation needs more confirmation to convince the propeller model so that the matter becomes to compare with the computational result of real propeller geometry and other body-force propeller models using the same CFDShip-Iowa RANS code. For doing so, the corresponding results for the actual propeller case, axisymmetric model and Yamazaki model are provided by IIHR of the University of Iowa. These three computations are carried out for the free running and self-propulsion and their RPS are different to each other. As the main purpose is to compare this model with actual propeller computation, all the settings are fixed according to the actual propeller one. The running conditions and particulars of the real propeller computation are shown in Table 5-2 in which they use the combined particulars of INSEAN ship hull, speeds and NMRI propeller diameter. The computation is carried out at the same conditions and the converged thrust and torque coefficients are summarized in Table 5-3. In comparison of the thrust identities between the current model and the actual propeller results, close agreements are achieved.

For the flow field analysis, the comparison between the four methods are illustrated in Figure 5-21 at the aft perpendicular section, $X=1$. Here, it should be noted that the real propeller geometry result is not time-averaged and it is just the solution at one instant time while the other models are time-averaged solutions. The highest contour level of the axial velocity profiles are set at 1.7 and all solutions can give that amount

except the Yamazaki model. At the first glance, it can be said that the current model is lower than the real one but if many solutions for many time steps of the actual propeller are made to be time-averaged, it is believed that the current model can predict as much similar as the real one. The reason can be explained as follows. In accordance to the self-propulsion in the free running case, the three propeller models RPS are different and among these, the axisymmetric model RPS is the highest with 12.275. If the current model is run at that RPS, it is sure it can predict even higher than the axisymmetric one. Moreover, the RPS of Yamazaki is higher than the current propeller, but in terms of solution, the current result gives stronger flow field than Yamazaki model. That means the current model can predict better than the other models in the time-averaged manner and as close as to the actual propeller prediction.

In order to understand the vortex structure, the Q criterion with $Q=5000$ colored by the axial velocity contours is illustrated in Figure 5-22 and Figure 5-23 for all four models. The mathematical equation of Q-criterion is shown in equation (34). In that figure, it is clear that the tip-vortex shedding can be estimated only by the real geometry propeller and the other body-force models can give the ring shape only. Among the body-force models, the current propeller gives similar trend with the other models normally. But, the rotating hub effect is included and the stronger hub vortex can be seen while that behavior is lack in the other models.

$$Q = \frac{1}{2} (|W_{ij}|^2 - |S_{ij}|^2) \quad (34)$$

Here, the non-dimensional strain-rate, S_{ij} is defined as

$$S_{ij} = \frac{1}{2} \left(\frac{\partial U_i}{\partial x_i} + \frac{\partial U_j}{\partial x_i} \right) \quad (35)$$

and the vorticity tensor is

$$W_{ij} = \frac{1}{2} \left(\frac{\partial U_i}{\partial x_i} - \frac{\partial U_j}{\partial x_i} \right) \quad (36)$$

Table 5-2 Running conditions of the computations by IIHR

L_{pp}	7 m
Dia	0.21656 m
RPS	10.52
U_0	1.179 m/s
Re	8.237×10^6
Fr	0.142
J_s	0.5175

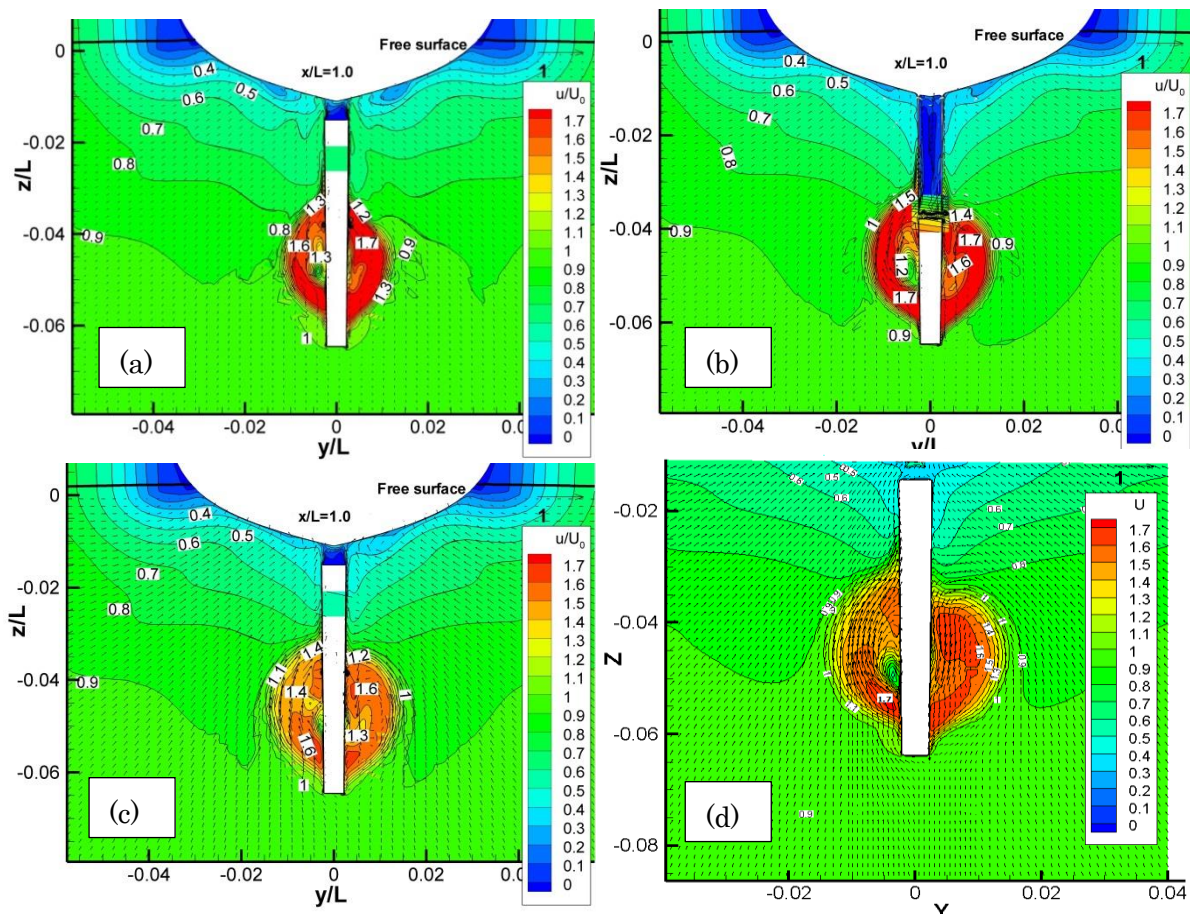


Figure 5-21 Comparison of axial velocity profiles at $X=1$ (a) Actual Propeller (b) Axisymmetric Model (c) Yamazaki Model (d) Current Propeller Model

Table 5-3 Comparison for all four propeller models

Propeller Model	Method	K_T	K_Q	RPS
Actual Propeller	Free Running	0.192	0.0237	10.52
Axisymmetric Propeller		0.147	0.0188	12.275
Yamasaki Propeller		0.174	0.0193	11.17
Current Propeller	Captive	0.187	0.0214	10.52

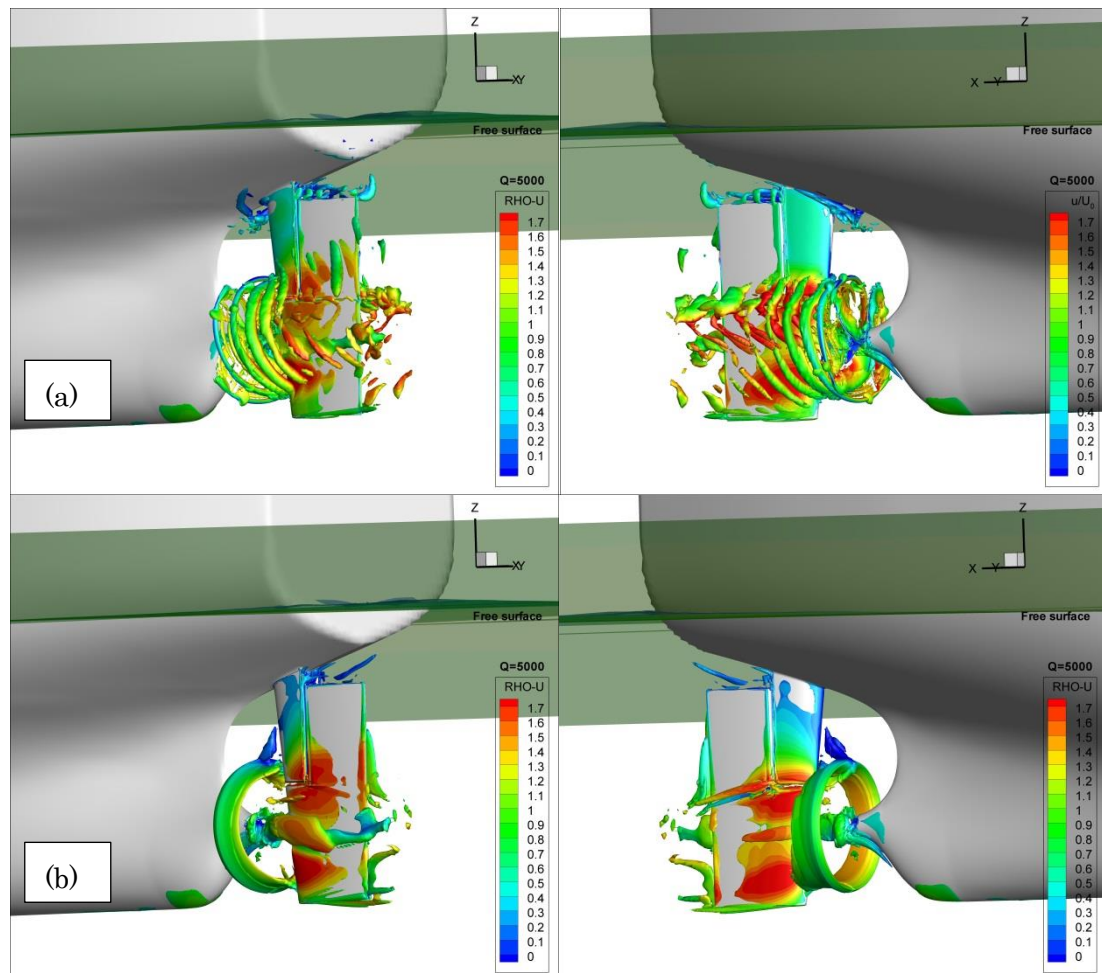


Figure 5-22 Illustration of Q-criterion for $Q=5000$ colored by the axial velocity contours (a) Actual Propeller (b) Axisymmetric Model

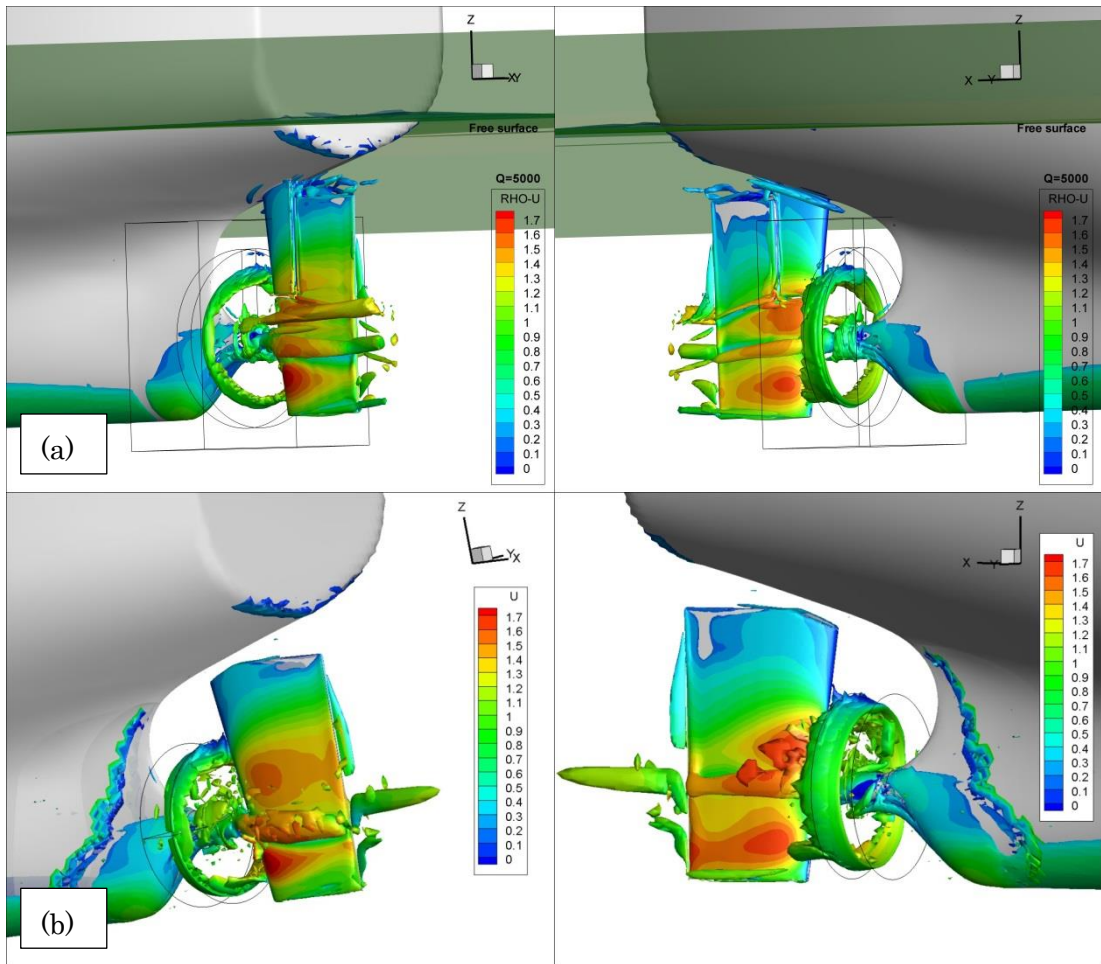


Figure 5-23 Illustration of Q-criterion for $Q=5000$ colored by the axial velocity contours (a) Yamazaki Model (b) Current Propeller Model

5.6 DISCUSSION AND SUMMARY

The computation for without-rudder and with-rudder cases have been carried out and compared with two sets of EFD data. In the nominal wake comparison, first EFD data is lower and when it is corrected, it becomes similar with CFD. However, in the effective wake in both without-rudder case and with-rudder case, most of CFD results are lower than EFD. If the nominal result of EFD is corrected, it will be far higher in the

effective wake. So, the experimental data is decided not to correct and the reason why CFD is under-predicted is analyzed and discussed. So, the second experimental data is used for the comparison with CFD. But, for this case, only ship point results and with-rudder case are available. The computation is set at the same conditions and the comparison is made for the downstream of the propeller. In the second comparison, the close agreement is observed with the conclusion that CFD has better results with second EFD data. All the computation conditions are the same but as the agreement level is different; it cannot be denied that the two experiments give different solutions. Because of the inconsistent agreements in the comparison with EFD results, the computation is carried out to compare with the real propeller geometry computation and with other body-force models. By analyzing and comparison with these solutions, the behavior of the current body-force model becomes more understandable and the capability of the current model is more convinced.

However, it cannot be denied that there is the dissipation problem in the computation. One reason might be the turbulence model as the wake field has separations and the turbulence model might have some failures to capture the flow field in details and other kinds of turbulence models will need to be tested. One more possibility is the overset grid spacing. SUGGAR is used for the grid overset region which automatically cuts the coarser grid if the two grid spacing is reasonably matched. That means if the grid spacing for the two blocks is quite different, SUGGAR will not be executable and the computation cannot be carried out. But, still, in the current case, some grid spacing for one block is much larger than the other one which will be hard for the interpolation between each block. As a numbers of blocks are used in the stern part of the ship, this grid issue might also be a reason of the under prediction of the flow field.

CHAPTER 6: STUDY OF COORDINATE SYSTEMS

6.1 OVERVIEW OF COMPUTATIONAL COORDINATES

The simple body-force propeller model has been developed and the interaction with the ship hulls has been studied. It is strongly believed that the model will be a reliable computational tool for the propulsion simulation in the future including from the free-running test, self-propulsion test to the seakeeping test. Until now, the proposed model is implemented on the polar type of grid and rectangular type of grid but in the future, the model will be implemented on any type of grid e.g. the boundary layer grid of ship hull so that no special grid treatment will be required for the model. Moreover, using this model, the computation will be carried out on earth-fixed inertial coordinates system for several kinds of maneuvering motion tests.

So, in this thesis, some assessments of coordinate transformation in the computation code are introduced briefly as part of the future plans. The coordinates system for the computational domain is studied with some mathematical models and some simple tests for the support of future work. Due to the lack of time, the thesis is terminated at the assessment of the coordinate study and all the consequent purposes will be left as the future work. However, the primary purpose of the thesis which is to introduce the new simple propeller model has clearly been presented.

The computations in Chapter 3, Chapter 4 and Chapter 5 are based on ship-fixed non-inertial coordinates system. But, the role of CFD will be quite limited if the playground for the CFD users is narrow. It is good enough for studying the wake field analysis and propeller performance in ship-fixed coordinate system but it has a great

limitation in terms of maneuvering tests in which the ship will be moving in multi degrees of freedoms and the desired relative motions of the surrounding fluid is difficult to implement as the boundary condition. In that sense, earth-fixed inertial coordinate system is used with its ease for simulating PMM test, CMT test and self-propulsion test and the method is also well-known as Computational Towing Tank and the desired motions are much easier to implement into the computational code compared to non-inertial coordinate system.

As the new propeller model has been coupled with the ship hull and the corresponding outcomes have been proved with reasonable agreements with EFD, the propeller model is desired to use for different types of simulations like several maneuvering simulations with captive, semi-captive or free running. So, some brief assessment of the coordinate system is studied and will be presented in this chapter. Although CFDShip-Iowa has an option to choose desired coordinate system, the analysis is carried out for general computational code as the knowledge can be applied for any computational code and will be explained in the following sections.

6.2 SHIP GEOMETRY AND GRID GENERATION

A simple hull form is selected for this study. The Wigley model which has parabolic waterlines and symmetrical shape of aft and bow can be simply developed by the equation (37). In this case, the notations for the coordinate system will be a bit different with the previous chapters. Here, (x', y', z') is referred to ship-fixed non-inertial coordinates, (X', Y', Z') is referred to earth-fixed inertial coordinates and both of these are in non-dimensionalized parameters. In this study, the computation

code of the author's laboratory which is based on non-inertial ship-fixed coordinates system is used. According to the computation code, the definition of the coordinate is different from previous notation again e.g. x' or X' is defined along the ship length with origin at the bow and positive towards the stern, y' or Y' is defined along the depth of water with positive towards deep water and z' or Z' is towards the lateral sides of the ship with positive for the starboard side. All the related computations will be based on these notations.

The governing equation is Navier-Stokes equation and the 12 points Finite Analytic Method (FAM) for space discretization and Euler Implicit Scheme for time discretization are used along with the PISO algorithm for velocity-pressure coupling. A single block domain grid, H-type grid is generated around the ship. The computational domain covers from -1 to +4 in x' -direction, from 0 to +3 in y' -direction and from -3 to +3 in z' -direction. The total grid size is $(91 \times 41 \times 51)$ with the non-dimensional ship length, 1. The standard Wigley dimension is used where the breadth to length ratio used is 0.1 and depth to length ratio is 0.125. The generated grid domains with usual coordinate systems using in CFD are shown in Figure 6-1.

$$z'_b = \frac{1}{2}B \left\{ 1 - \left(\frac{2x'}{L} \right)^2 \right\} \left\{ 1 - \left(\frac{y'}{D} \right)^2 \right\} \quad (37)$$

L, B and D referred to length, breadth and depth of the hull and z'_b is the half breadth offset. The grid domains are generated by the grid generation code of the Authors' laboratory by setting small meshes near the body surface for capturing of the detailed flow field near the surface. The body part is covered by 41 and 21 grid points in x' and y' direction respectively. The minimum grid spacing is 0.0015 in non-dimensional lengths in y' and z' -direction. The grids generation is checked to be more orthogonal by solving the Poisson's equation.

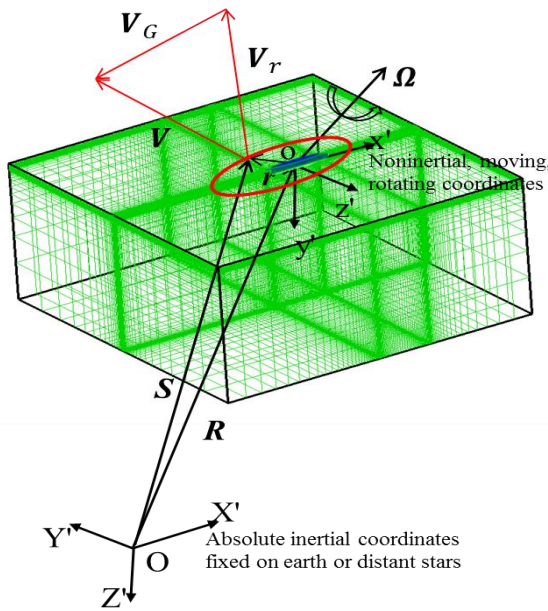


Figure 6-1 Grid domain with different coordinate systems definitions

6.3 COORDINATE TRANSFORMATION

As the purpose of this research is to develop the computation code in inertial frame, the relation between the non-inertial and inertial frames is shown in Figure 6-1. In non-inertial coordinate (x', y', z') which is fixed on the body, every single point on its wet surface will have corresponding relative velocity to the surrounding fluid denoted by \mathbf{V}_r . Therefore, the momentum equation in this frame is written in tensor form in equation (38) with body-force term \mathbf{a}_{rel} in equation (39) which is a composition of translational and rotational movement of the fluid. The continuity equation in terms of relative velocity is written in equation (40).

$$\frac{\partial \mathbf{V}_r}{\partial t} + \mathbf{V}_r \cdot \nabla \mathbf{V}_r = -\nabla(p + \gamma \cdot y') + \frac{1}{Re} \nabla^2 \mathbf{V}_r - \rho \mathbf{a}_{rel} \quad (38)$$

$$\mathbf{a}_{rel} = \ddot{\mathbf{R}} + 2\boldsymbol{\Omega} \times \mathbf{V}_r + \boldsymbol{\Omega} \times (\boldsymbol{\Omega} \times \mathbf{r}) + \dot{\boldsymbol{\Omega}} \times \mathbf{r} \quad (39)$$

$$\nabla \mathbf{V}_r = 0 \quad (40)$$

In inertial coordinate (X', Y', Z') , the momentum and continuity equations will be represented by the absolute velocity of the ship and are written in equation (41) to (43).

In the momentum equation, the convection term will have to consider the grid velocity (equation (43)) in inertial frame which is corresponded to the translating velocity and rotational term. The absolute velocity \mathbf{V} in inertial frame is the resultant of the relative velocity \mathbf{V}_r and grid velocity \mathbf{V}_G which is illustrated in figure 6-1.

$$\frac{\partial \mathbf{V}}{\partial t''} + (\mathbf{V} - \mathbf{V}_G) \cdot \nabla \mathbf{V} = -\nabla(p + \gamma \cdot y') + \frac{1}{Re} \nabla^2 \mathbf{V} \quad (41)$$

$$\nabla \mathbf{V} = 0 \quad (42)$$

$$\mathbf{V}_G = \dot{\mathbf{R}} + \boldsymbol{\Omega} \times \mathbf{r} \quad (43)$$

The governing equation of the computation in earth-fixed inertial coordinate system will be based on equation (41) and it is modified for free movement in 3 DOF of the grid, leaving the velocity components in inertial frame. The transformation is performed in components form and the moving grid position which is a combination of the translational and rotational motion as a function of time are as shown equation (44) to equation (47) where (X'_0, Y'_0, Z'_0) is the arbitrary grid position in inertial frame with the geometry shown in Figure 6-2 and t is the time represented in non-inertial frame.

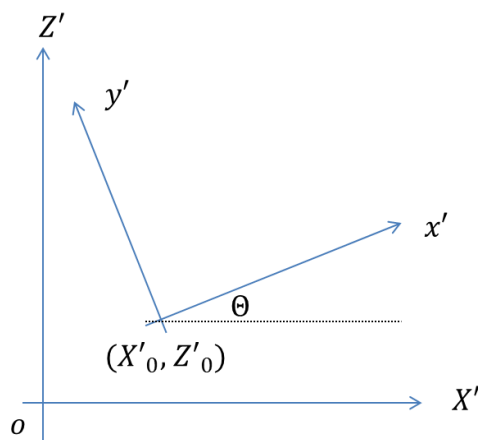


Figure 6-2 Moving grid geometry

$$X' = X'_0(t) + x' \cos(\Theta(t)) - z' \sin(\Theta(t)) \quad (44)$$

$$Z' = Z'_0(t) + x' \sin(\Theta(t)) + z' \cos(\Theta(t)) \quad (45)$$

$$Y' = Y'_0(t) = 0 \quad (46)$$

$$t'' = t \quad (47)$$

Using these relations, the momentum equation (equation (41)) is operated differentially by each term and then transformed from the physical domain to the computational domain in non-orthogonal curvilinear coordinate (ξ, η, ζ, τ) . A partial transformation is used in which only the independent variables are transformed, leaving the velocity components in physical domain. But, all the velocities and geometrical coefficients in the transformed equations still belong to the moving coordinate. According to the purpose of this computation, the velocity components are defined in the absolute inertial earth-fixed coordinates (X', Y', Z') so the velocity components with corresponding geometrical coefficients must be transformed back into inertial coordinates. Finally, the momentum equations with the velocity components in inertial coordinates in the moving non-inertial grids are obtained and the detailed mathematical works will be omitted here.

6.4 COMPUTATIONS OF MANEUVERING MOTIONS

Now, the governing equations are in inertial frame and the computation of maneuvering motions is comparatively easier by giving the desired body movement velocity to the ship hull. The boundary condition of the computation is shown in equation (48) to (51). In the inertial frame, the velocity components and pressure value in the far field could be almost zero. This condition can make the computation

much easier to get the converged solution compared to the computation in non-inertial frame.

$$\text{Inlet} : U = V = W = p = 0 \quad (48)$$

$$\text{Far field} : \nabla U = \nabla V = \nabla W = \nabla p = 0 \quad (49)$$

$$\text{Free surface (i.e., } y' = 0) : V = 0 \quad (50)$$

$$\text{On the body surface} : U = U_G, V = V_G, W = W_G \quad (51)$$

In this study, different kinds of motions like static drift, pure sway, pure yaw and circular motion test have been computed by giving the velocity components boundary condition at the solid surface of ship hull. The computation process to accomplish such complicated motions could be carried out with less effort in inertial code. The pure yaw and circular motion test cases are briefly described here.

In the steady movement with $U_G = -1$ (minus refers to the direction of ship motion towards negative X' -direction), the hull is given the sway velocity W_G . The sway distance is a sinusoidal sine with a function of frequency as shown in equation (52) where A is the amplitude of the motion, ω' is the frequency, t is the time. In this case, amplitude is taken as 0.05; frequency is 2.094 with the three periods (T') non-dimensionally. The sway velocity is the differentiation of the sway distance with respect to time and shown in equation (53). The value of V_G is imposed by zero as there is no movement in y -direction. In addition to sway motion, the yaw angle and the corresponding yaw rate are imposed as in equation (55) and (56).

$$Z'_0(t) = A \sin(\omega' t) \quad (52)$$

$$W_G = Z'_0(t) = A\omega \cos(\omega' t) \quad (53)$$

$$\omega' = \frac{2\pi}{T'} \quad (54)$$

$$\Theta(t) = \tan^{-1} \frac{W_G}{U_G} \approx \frac{W_G}{U_G} = \frac{A\omega \cos(\omega' t)}{U_G} \quad (55)$$

$$\dot{\Theta}(t'') = \frac{\ddot{z}_0(t)}{U_G} = \frac{-A\omega^2 \sin(\omega' t)}{U_G} \quad (56)$$

For the yaw rotation, the referenced point is taken at the center of gravity of the plate at (0.5,0)in (X',Z') plane. Centered at this point, the ship is rotated in a sinusoidal cosine with a function of frequency (equation (54)). The sway and yaw movements are ninety-degree phase different. The computation for this case is carried out at zero drift angle. To get rid of the non-uniform disturbance, the simulation is carried out up to three periods of motion. The pressure force distribution and the shear force distribution over a period of motion are shown in Figure 6-4 and Figure 6-5. The smooth hydrodynamics forces in one period show that the computation code is working well.

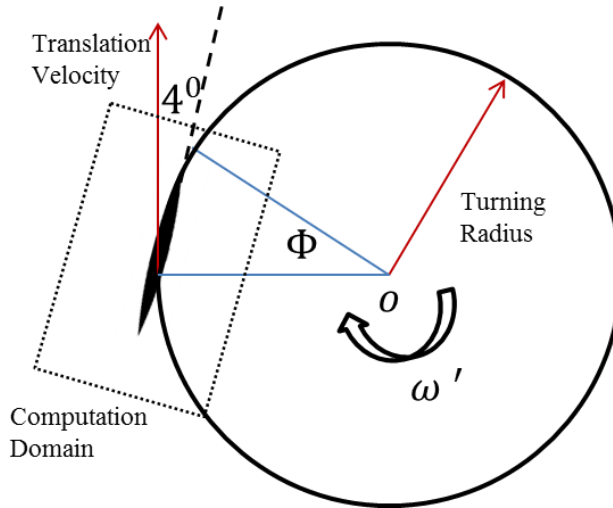


Figure 6-3 Motion algorithms of CMT test

The circular motion test is important for the maneuvering test of rudder and it is also computed using the inertial coordinate code. The motion algorithm is shown in Figure 6-3. The whole domain with the ship has to move in the circular path centered at O. In this study, the center of rotation is taken reference at (0.5, 3) in (X',Z') plane with the

turning radius in inertial frame. The rate of rotation or frequency ω (equation (57)) is kept constant at 0.2. In order to achieve the circular motion with the centripetal force towards the center O, some drift angle is imposed by 4 degree to the inside of the circle. The simulation is carried out for two full circles of motion and the surge force (x' -direction) and sway force (z' -direction) on the ship hull in non-inertial coordinate is shown in Figure 6-6.

$$\omega' = \frac{d\Phi(t)}{dt} = \frac{2\pi}{T'} \quad (57)$$

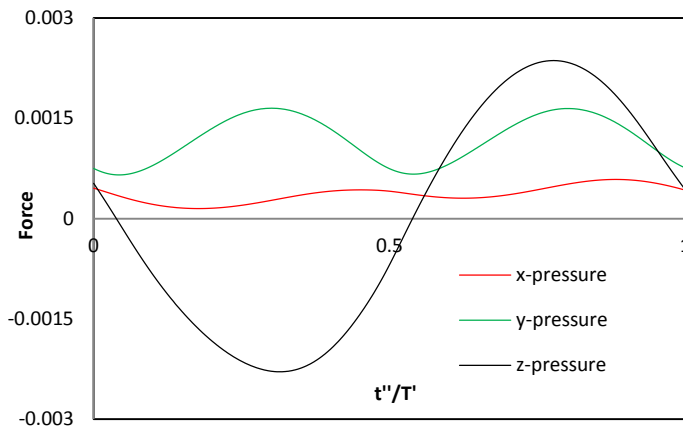


Figure 6-4 Pressure force distributions on the hull

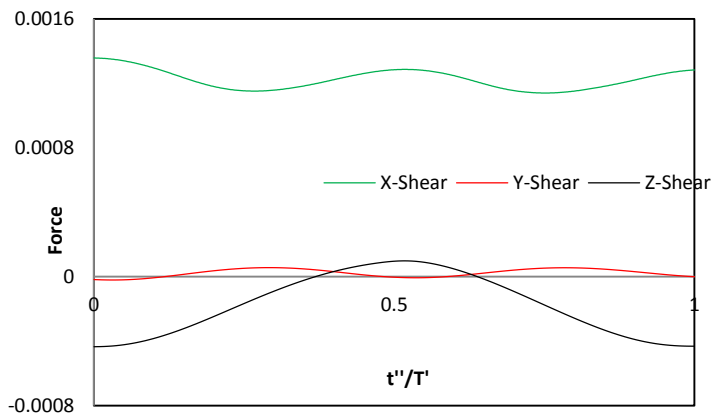


Figure 6-5 Shear force distributions on the hull

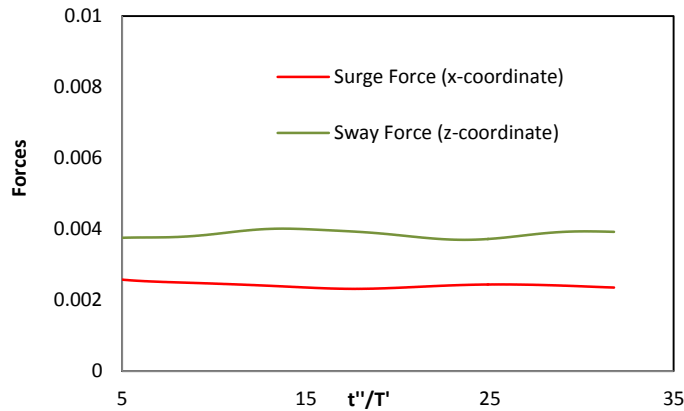


Figure 6-6 Hydrodynamics forces on the hull in CMT test

6.5 CONCLUSION

The coordinate analysis has been described briefly in this chapter. It is distinct that for the maneuvering computation, the earth fixed coordinate system is much simpler for CFD computation. The proposed propeller model which can work on any coordinate system will be an effective tool for future researches in any specific field. Even though the self-propulsion test in multi-degree of freedom movement is an interest for future work, due to the lack of time, only the assessment of the coordinate study could be accomplished in this thesis. All of the corresponding works will be left as the future works.

CHAPTER 7: SUMMARY AND CONCLUSION

7.1 SUMMARY OF THE THESIS

7.1.1 S60 cases

The contents of the thesis have been explained in step-by-step ways. The proposed body-force propeller model which was successfully simulated for open water characteristics is brought to couple with ship hull and the interaction case is analyzed in this thesis. Firstly, the simple S60 ship hull without hub in original offset is used and validation is carried out with experimental results. A new propeller model with blade element theory is coupled with RANS computation code without requiring detailed modeling of propeller geometry and unnecessarily required to choose grid type for the propeller. Before implementing the propeller model, the flow around the bare hull itself is computed and the flow field near the wake regions is observed, discussed and validated. The discussion is focused mainly on the experimental model point at $n_{rev}=7.8$ rps. A lot of researches are performed by many authors in this case and the comparison is made not only with the EFD data but also with some previous models. The computation results are interpreted, discussed and some weak facts are discovered for avoidance in future research like the lack of hub geometry. The computation results on various propeller loadings are also discussed and the capability for free-running test with corresponding comparison with the EFD data is proved. The total resistance forces and the wake fractions are plotted based on thrust loading coefficients and the behavior of the propeller is observed.

Due to the lack of hub surface effect, the S60 ship hull is then modified in the stern part to fit with the boss block and the simulation is carried out again as the next approach. As the energy saving issue is the priority target in shipping industry in present days, many researchers are trying to install energy saving devices on the ship hull. The installation of these devices behind the propeller is mostly popular as they could increase the propulsive efficiency more. In that sense, the output flow by the rotating propeller blade with the rotating hub is very important as they become the inflow to the energy saving device. Without considering hub effect, the effectiveness of these devices could not be observed well. So, the effect of rotating hub should not be neglected especially in the computational field. Based on the fact mentioned above, the research has been extended from the computation of the hull S60 in original offset by adding the stern tube on the hull and the hub which is similar to the geometry used in experiment to prove that the propeller model works properly and the effect of the hub is observed which many researchers omitted in their researches. Even though the hub makes the grid generation more complicated, the outputs are better and quite impressive. In this thesis, the detailed flow field is analyzed and closer agreement with EFD is achieved by the computation with the hub in propeller model with the stronger vortex pattern at the downstream part of the propeller caused by the rotating hub. The propulsive quantities of the propeller are computed, the wake field region behind the propeller is analyzed and the propeller-hull interaction is investigated by plotting the surface pressure with the observation of the effect of propeller. In overall, the ability of the proposed propeller model has been proved in the computation of with-hub and without-hub and both of which give satisfactory outputs with the better results with the hub.

7.1.2 KVLCC2 case

After the reasonable results are achieved that the propeller model is working well with the simple hull form, then the model is again coupled with the well-known tanker model KVLCC2 and the flow field is analyzed with the rudder as well. The ship hull is an interesting tool for studying the local fields around the tanker hull form and many institutes have already submitted the patterns of these flow fields. The main interest in this thesis is to analyze the effective wake field with the current proposed propeller model. In this case, the hub block is generated and used throughout the computation. So, the cases are divided into with-rudder and without-rudder cases. The computational setting is defined similar as the experimental settings which were carried out two times in 2013 at Osaka University towing tank in different seasons. The propeller revolution rate is set at the self-propulsion point of the model at 16.5 rps and 11.1 rps for the ship point. According to the experiment, the ship hull is in the trim condition by the bow. Together with the computational outcomes of the two cases, the discussions are made and the validations are carried out with EFD. In this computation, some differences in the comparison between CFD and EFD are found which seem to be the errors raised from the numerical dissipation or the overset grid spacing. But, better agreements are achieved with the second experimental works than the first one. Even though CFD computation gives lower results than EFD, the flow patterns are very similar.

In order to convince the propeller model, the computation is compared with actual propeller computation and other body-force propeller models (axisymmetric and Yamazaki model) using the same RANS code CFD-SHIPiowa. By comparing the results of the four propeller models, the capability of the current propeller model is more

convinced.

However, it is undeniable that there is some dissipations in the computation. So, several tests by using different turbulence models or different kinds of overset grid are needed to carry out to understand the reason of the differences. However, the propeller model has been proved for its effective prediction by some extent and it is believed to be working well and the consequence tests will be continued as future research plan.

7.2 OVERALL CONCLUSION

For the review of the whole thesis, the propeller-hull and propeller-hull-rudder interaction computations have been discussed by using the RANS code and simple body-force distribution propeller model. The new proposed simple body-force model, which has been proved of its open water characteristics curves by using Polar-grid or Cartesian rectangular grid and also, has estimated the effect of free surface on the propeller thrust identities, is successfully implemented and proved that it is working well in the wake field behind the ship.

In this thesis, the propeller model has been computed with two different hull forms and the impressive results could be achieved. The wake field behind the ship is much complicated and to predict the fields with the rotating propeller is not an easy job to deal with. The correct prediction of interaction between the ship and propeller or rudder will not be achieved without a high prediction of the correct flow field by the ship as well as a reliable prediction of the propeller model. In this work, the newly proposed propeller model is brought to couple with well-known computation code CFDSSHIP-Iowa and the impressive predictions by the propeller model have been presented and

discussed in the previous chapters. The results are agreeable and reasonable with experiments and some predictions are even better than the other propeller models. Some few weak points are found out and even though the reasons are in the vague conditions, some of the opinions are discussed in each chapter. With several expected future works, the propeller model has been computed and validated for its predictable quality in this thesis.

The main purpose of the research, which is to introduce a new technique to predict body-force for the propeller effect and to prove its capabilities whether it is working well in the complicated wake field and can predict the propulsive quantities with the reasonable outputs, is believed to be well presented in this thesis. There are many research activities whereas the high quality of the detail flow field around the propeller blade is unnecessary in the propulsion field as well as in the seakeeping or maneuvering fields and it is so inconvenient to use the real geometry propeller computation for these kinds of researches because of complication, time consuming and high cost. Moreover, some concepts of using body-force effects are still complicated as there are several steps to adjust between the RANS and propeller performance programs because the effective wake is required to be extracted from the total velocity fields in order to let the propeller model work to get the thrust and torque forces. The current proposed propeller model is so simple and just a very short subroutine of the program is enough to compute the body-force terms. It has been commented for the current model that the fact that the current propeller model can predict the high quality flow field better than the other models is not because of the un-necessity to extract the propeller induced velocity to get the effective inflow velocity into the propeller plane but because the current model utilizes each blade element as well as on the effective pitch in the theory to get the lift

force. In response to this, the current model is basically similar to other potential theory based models and it is true that the concepts are same with these models. However, for CFD researchers, the programming step needed to deal with this model is much simpler than the other models.

Moreover, this concept could be applied to any types of grid by just searching the grid points near the propeller plane for the thrust and torque computation. The simplicity and flexibility of the proposed body-force propeller model will be great advantages in the future research related to propulsion field like; free-running computation, several kinds of maneuvering computations in inertial coordinates and ship-ship interaction case for extensive research field by overcoming the restrictions of the propulsion capability in the computation field presently. Actually, it is the responsibility of the researcher to make the CFD application tool to be easier and more users friendly, it is proud to publish this new model. Finally, the current proposed propeller model is believed to be useful as an effective tool for all computational propulsive research activities in the future.

References

Abtel-Maksoud, M, Rieck, K, and Menter, F. R et al.: Unsteady numerical investigation of the turbulent flow around the container model (KCS) with and without propeller: Proc Workshop on Numerical Ship Hydrodynamics, Workshops on Numerical Ship Hydrodynamics, Gothenburg, Sweden, September, 2000.

Chou, S.K., Chau, S.W., Chen, W.C., and Hsin, J. Y.: Computations of ship flow around commercial hull forms with free surface or propeller effects: Proceedings, Workshop on Numerical Ship Hydrodynamics, Gothenburg, Sweden, 2000.

Hough, G and Ordway, D et al.: The generalized actuator disk: Tech. Report TAR-TR 6401, Therm Advanced Research, Inc., Ithaca, New York, 1964.

Kawamura, T, Miyata, H, and Mashimo, K et al.: Numerical simulation of the flow about self-propelling tanker models: Journal of Marine Science and Technology, Vol 2, pp 245-256, 1997.

Lars, L, Stern, F, Michel, V et al.: Numerical Ship Hydrodynamics: An assessment of the Gothenburg 2010 Workshop, March, 2013.

Paterson, E. G., Wilson, R. V., and Stern, F.: General-purpose parallel unsteady RANS ship hydrodynamic code: CFDSHIP-IOWA, IIHR report No. 432, 2003.

Simonsen, C.D., and Cross-Whiter, J.: Study of three RANS body-force propeller models: Proceedings, 5th Numerical Towing Tank Symposium, Pornichet, France, 2002.

Simonsen, C.D and Stern, F et al.: RANS Maneuvering Simulation of Esso Osaka with Rudder and a Body-Force Propeller: Journal of Ship Research, Vol. 49, No. 2, pp.

98-120, 2005.

Shen, W.Z, Sorensen, J.N and Mikkelsen, R et al.: Tip Loss Correction for Actuator/Navier-Stokes Computations: *Journal of Solar Energy Engineering*, Vol. 127, pp.209-213, 2005.

Stern, F, Kim, HT, Patel, V. C, and Chen, H. C et al: A viscous-flow approach to the computation of propeller-hull interaction: *Journal of Ship Research*, Vol. 32, No.4, pp. 263-284, 1988.

Stern, F, Kim, HT, Zhang, D.H, Toda, Y, Kerwin, J and Jessup, S et al.: Computation of Viscous Flow Around Propeller-Body Configurations: Series 60 CB = 0.6 Ship Model: *Journal of Ship Research*, Vol. 38, No.2, pp. 137-157, 1994.

Tahara, Y., and Ando, J.: Comparison of CFD and EFD for KCS container ship in with/without propeller conditions: *Proceedings, Workshop on Numerical Ship Hydrodynamics*, Gothenburg, Sweden, 2000.

Takada, N., and El Moctar, O. M.: Simulation of viscous flow about “Esso Osaka” in maneuvering motion, *Proceedings: 3rd Numerical Towing Tank Symposium*, Tjarno, Sweden, September, 2000.

Toda, Y., Stern, F., Tanaka, I. and Patel, V.C.: Mean-flow measurements in the boundary layer and wake of a series 60 CB = 0.6 model ship with and without propeller: IIHR Report No. 326, Iowa Institute of Hydraulic Research, The University of Iowa, Iowa City, 1988.

Toda, Y, Stern, F, Tanaka, I and Patel, VC et al.: Mean-flow measurements in the boundary layer and wake of a Series 60 CB=0.6 model ship with and without propeller: *Journal of Ship Research*, Vol.34, No.4, pp. 225-252, 1990.

Tokgoz, E, Win, YN, Kuroda, K. and Toda, Y et al.: A New Method to Predict the Propeller Body Force Distribution for Modeling the Propeller in Viscous CFD Code without Potential Flow Code: 2nd East Asia International Student Symposium on Maritime Sciences, Kobe, Japan, Vol. 4, pp. 20-24, 2012.

Tokgoz, E, Win, YN, Kuroda, K. and Toda, Y et al.: A New Method to Predict the Propeller Body Force Distribution for Modeling the Propeller in Viscous CFD Code without Potential Flow Code: Journal of Japan Association of Naval Architects and Ocean Engineers (JASNAOE), Vol. 19, pp 1-7, 2014.

Yamazaki, R et al.: On the Propulsion Theory of Ships on Still Water (Improved Theoretical Method): Memoirs of the Faculty of Engineering, Kyushu University, Vol. 34, No.1, pp. 65-88, 1977.

Yokota, S et al.: The simple prediction method for body-force distribution in CFD code, *B.S. Thesis (In Japanese)*, Osaka University, 2013.

Win, YN, Tokgoz, E, Wu, PC, Stern, F and Toda, Y et al.: Computation of Propeller-Hull interaction using Simple Body-Force Distribution Model around modified Series 60 $C_B=0.6$ with hub: Proceedings of 24th International Ocean and Polar Engineering Conference, Volume 4, pp. 759-765, 2014.

Win, YN, Tokgoz, E, Wu, PC, Stern, F and Toda, Y et al.: Computation of Propeller-Hull Interaction using Simple Body-Force Distribution Model around Series 60 $C_B=0.6$: Journal of Japan Association of Naval Architects and Ocean Engineers (JASNAOE), Vol. 18, pp. 17-27, 2013.

Win, YN and Toda, Y et al: Viscous Flow Computation around the Wigley Hull with the maneuvering motion using the Inertial Coordinate System on the Non-Inertial

Grids: Jurnal Teknologi, Volume 66, No.2 pp. 77-84, 2013.

Win,YN and Toda, Y et al: Viscous Flow Computation around the Wigley Hull with the maneuvering motion using the Inertial Coordinate System on the Non-Inertial Grids: Proceedings of 6th Asia Pacific Workshop on Marine Hydrodynamics -APHydro2012, pp. 270-275, 2012.

Appendix A – Open Water Characteristics

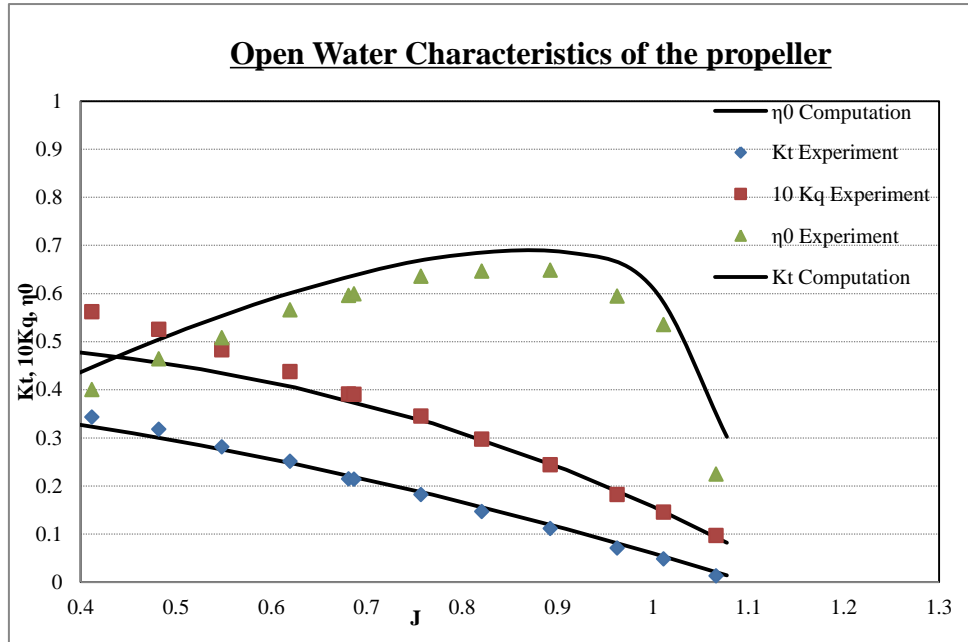


Figure A-1 Open water characteristics curve of S60 propeller provided by Tokgoz

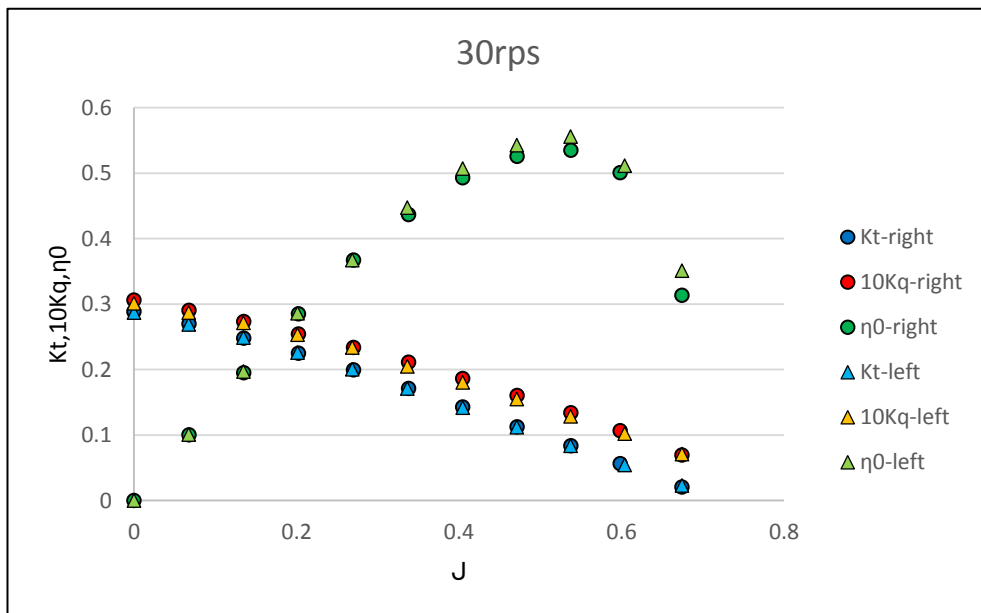


Figure A-2 Open water characteristics curve of KVLCC2 right- and left-handed propellers for 30 rps provided by Akamatsu

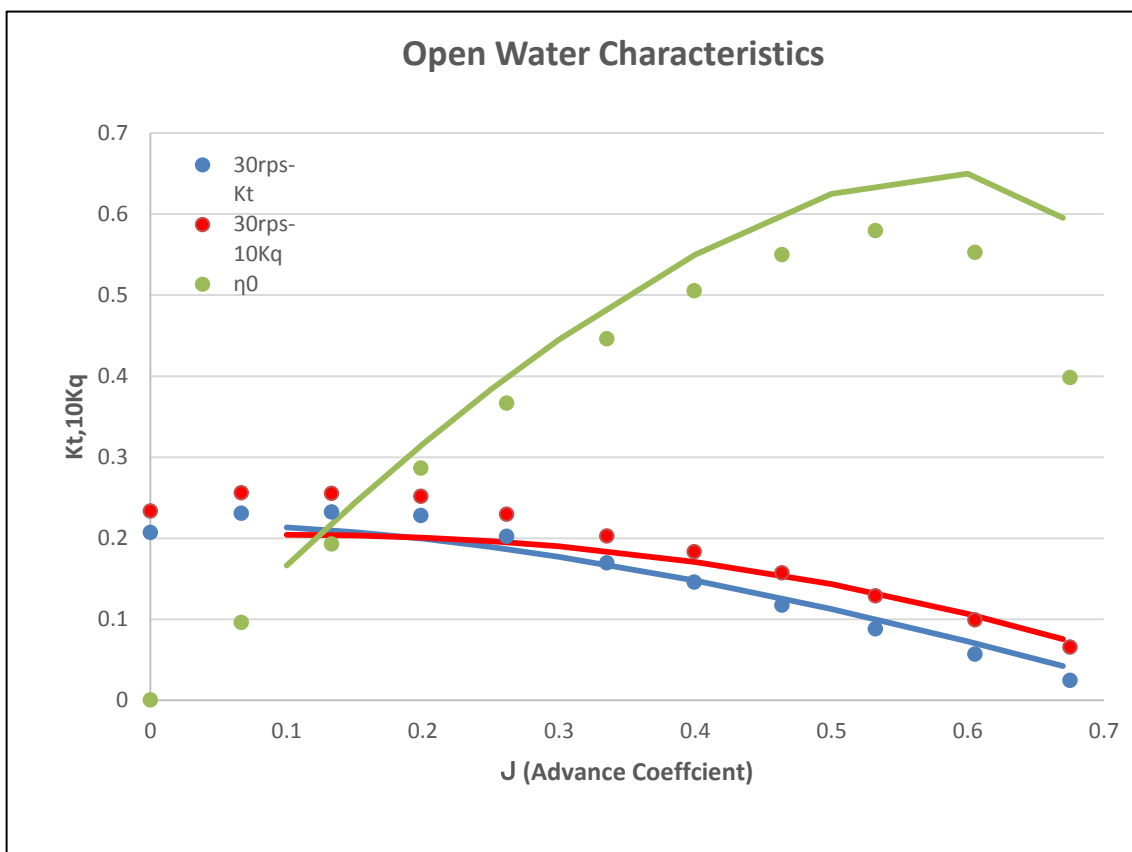


Figure A-3 Open water characteristics of KVLCC2 propeller computation and comparison with EFD data provided by Tokgoz

Appendix B – Computational results at Model Point

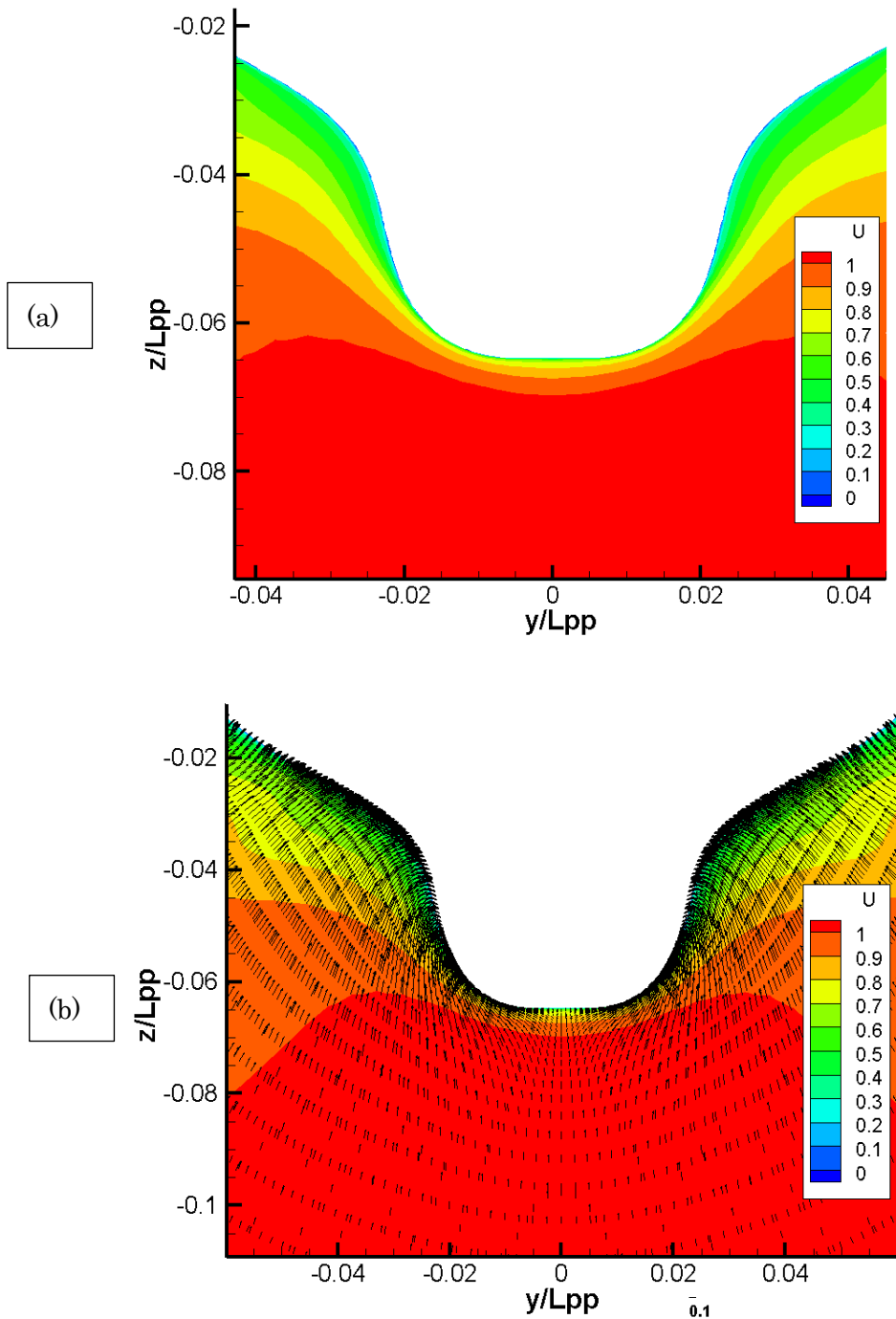


Figure B-1 (a) Axial velocity profiles and (b) cross-flow components at $X=0.9$ section for with-rudder condition of KVLCC2

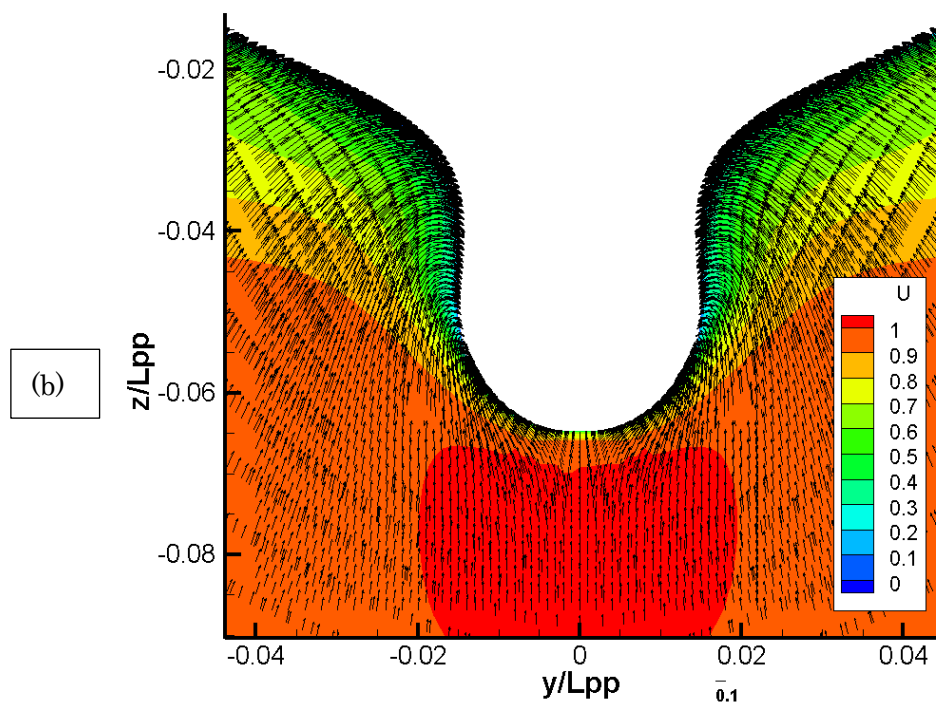
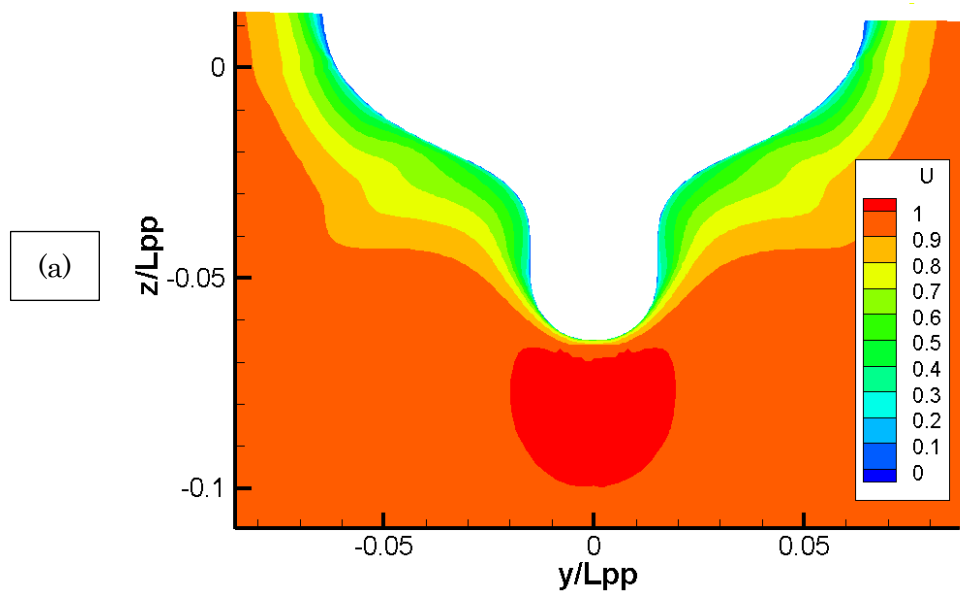


Figure B-1 (a) Axial velocity profiles and (b) cross-flow components at $X=0.925$ section for with-rudder condition of KVLCC2

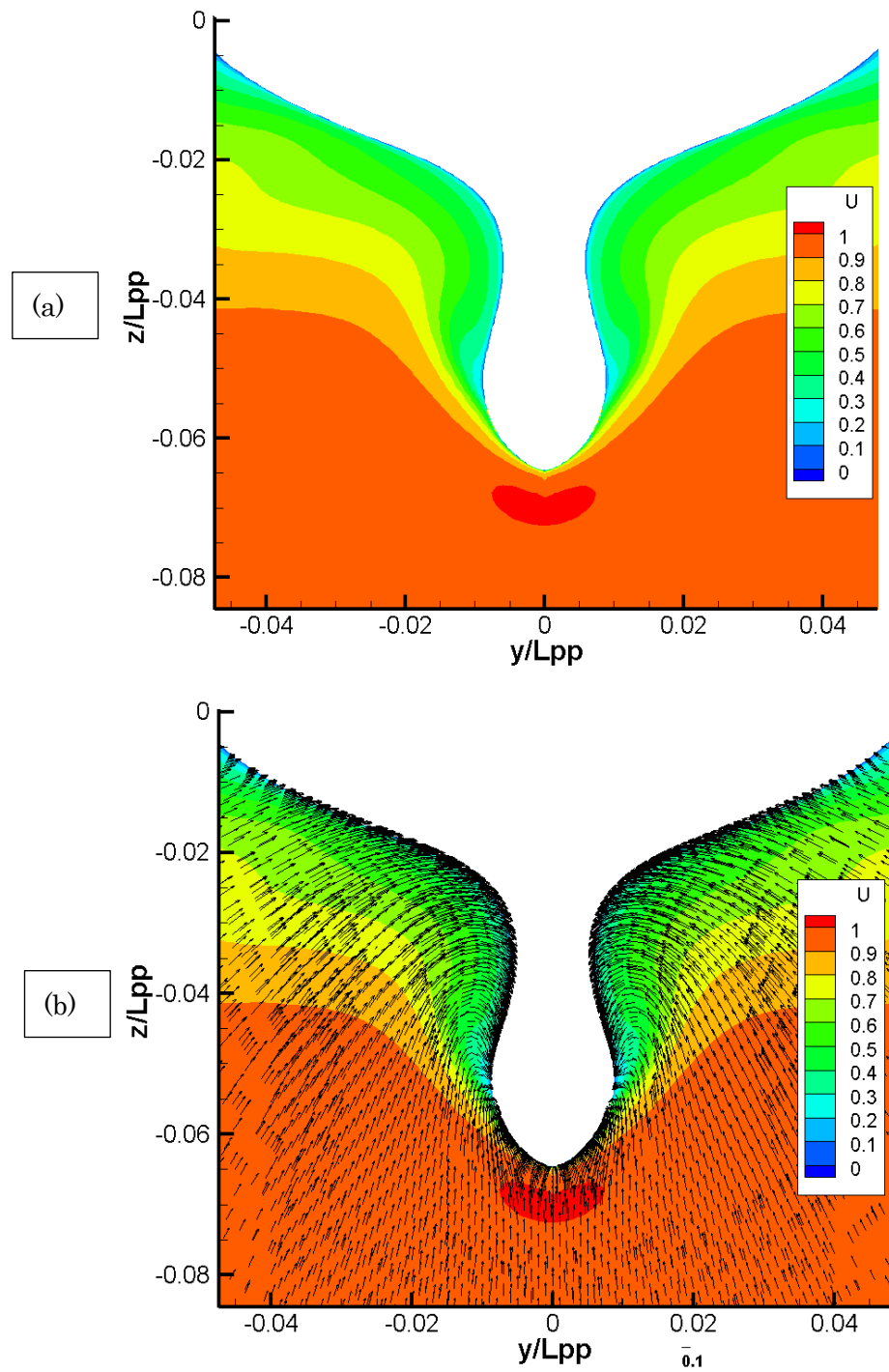


Figure B-1 (a) Axial velocity profiles and (b) cross-flow components at $X=0.95$ section for with-rudder condition of KVLCC2

Appendix C– Computational result at ship point

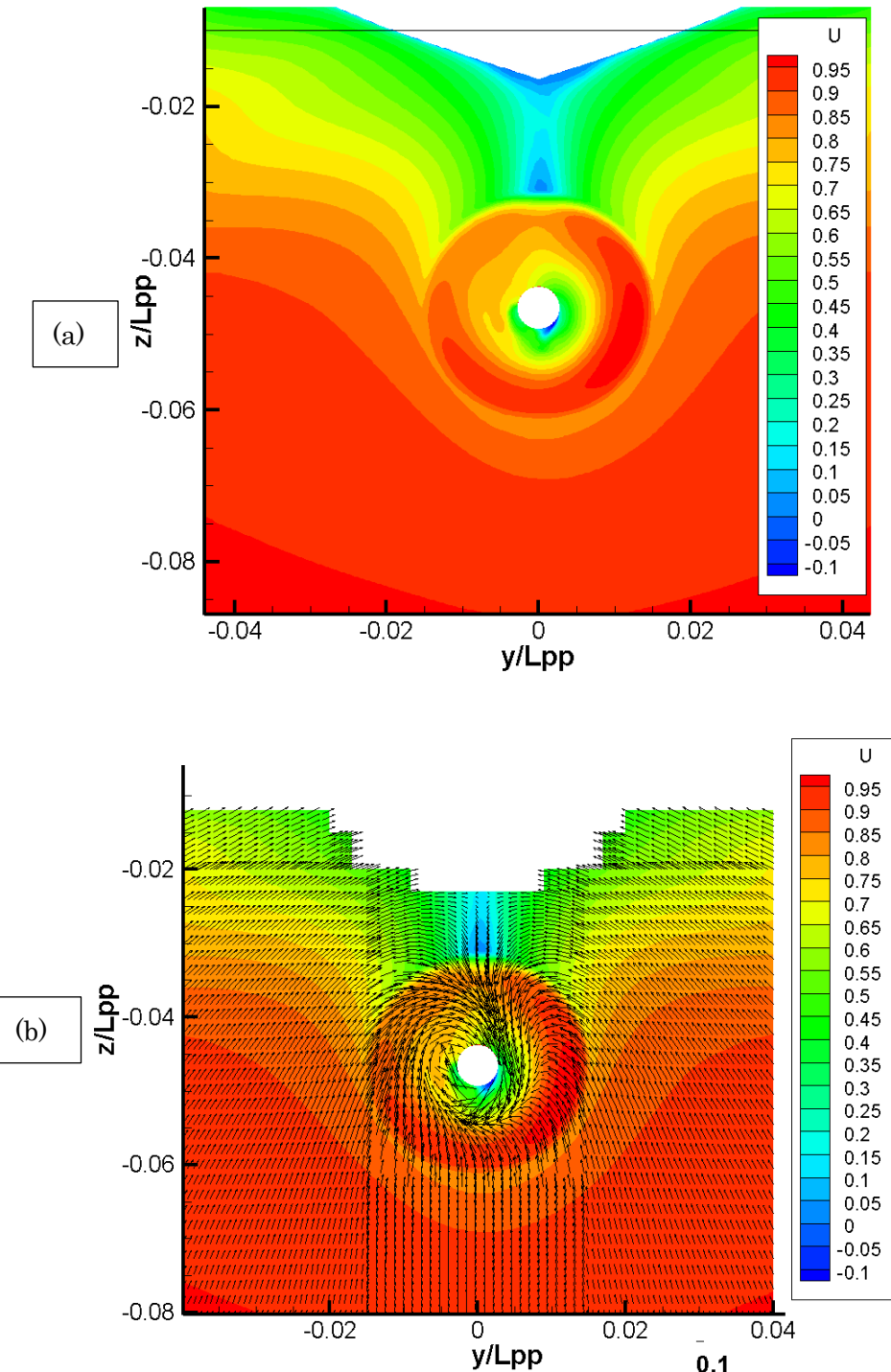


Figure C-1 (a) Axial velocity profiles and (b) cross-flow components of CFD at $X=0.98125$ section at ship point for with-rudder condition of KVLCC2 (EFD data unavailable)

Acknowledgement

First of all, I would like to give my heartily thanks to my supervisor, Prof. Yasuyuki Toda for his kind supervisions and effective instructions throughout my doctoral academic years. My appreciation would also go to the support of Prof. Yasuyuki Toda for all facilities for my research such as the cluster computer which is very effective for numerical computation that would make my publication of this thesis in time.

I would like to thank Professor Frederick Stern of IIHR for his kind allowance to let me use the CFDShip-Iowa version 4. I also would like to thank Dr. Seyed Hamid Sadat Hosseini, an assistant research scientist of IIHR, for his kindly help related to the computation code.

The person I would like to give special thanks is my respectful senior, Dr. Ping-Chen Wu, who has helped me throughout my research by introducing techniques related to the CFDShip-Iowa and by running the confidential SUGGAR package for the overset grid part whenever the grids are generated.

I also would like to extend my thanks to the thesis committee member and professors, such as Prof. Yasuyuki Toda, Prof. Masashi Kashiwagi, Prof. Kiyoshige Matsumura and Prof. Hiroyoshi Suzuki, for reviewing my work, giving valuable comments and attending my final defense presentation. I would like to thank all of my lab mates, colleagues and friends in Osaka University and in Japan for spending time with me while I am away from my home country.

Especially, I would like to thank the Osaka University for accepting me as one of its students and the Japanese government for providing me with the MEXT scholarship which is the main reason that I can finish the work. I would like also to thank to all of

the Professors and friends of Myanmar Maritime University who have motivated me to be more interested in the Naval Architecture and Ocean Engineering field and for cheering me to study abroad.

And, this work would not be finished when the advanced computing systems and computation codes are not available. I would like to give my thanks to all of those who have developed such amazing advanced technology and for their kind contribution.

Finally, I would like to thank my parents for giving me a birth to this world and this thesis will be a precious gift to my parents for their effort of raising me in education throughout my life.

List of publications

Publications as first Author

- (1) Viscous Flow Computation around the Wigley Hull with the maneuvering motion using the Inertial Coordinate System on the Non-Inertial Grids(Proceedings of 6th Asia Pacific Workshop on Marine Hydrodynamics-APHydro2012)
(Authors: Yan Naing Win, Yasuyuki Toda)
- (2) Viscous Flow Computation around the Wigley Hull with the maneuvering motion using the Inertial Coordinate System on the Non-Inertial Grids (Jurnal Teknologi, Volume 66, No.2 pp77-84, 2013)
(Authors: Yan Naing Win, Yasuyuki Toda)
- (3) Computation of Propeller-Hull interaction using Simple Body-Force Distribution Model around Series 60 $C_B=0.6$ (JASNAOE, Volume 18, pp17-27, 2013)
(Authors: Yan Naing Win, Tokgoz Emel, Ping-Chen Wu, Frederick Stern, Yasuyuki Toda)
- (4) Computation of Propeller-Hull interaction using Simple Body-Force Distribution Model around modified Series 60 $C_B=0.6$ with hub (Proceedings of 24th International Ocean and Polar Engineering Conference, 2014)
(Authors: Yan Naing Win, Tokgoz Emel, Ping-Chen Wu, Frederick Stern, Yasuyuki Toda)

Publications as Co-author

- (1) A New Method to Predict the Propeller Body-Force Distribution for Modelling the Propeller in Viscous CFD code without Potential Flow Code (Proceedings of the 2nd East Asia International Student Symposium of Maritime Sciences (EAISS2012), pp20-24)
(Authors: Emel Tokgoz, Yan Naing Win, Kazuhiro Kuroda, Yasuyuki Toda)

(2) A New Method to Predict the Propeller Body-Force Distribution for Modelling the Propeller in Viscous CFD code without Potential Flow Code (Conference Proceedings, The Japan Society of Naval Architects and Ocean Engineers, Vol.16)

(Authors: Emel Tokgoz, Yan Naing Win, Kazuhiro Kuroda, Yasuyuki Toda)

(3) A New Method to Predict the Propeller Body-Force Distribution for Modelling the Propeller in Viscous CFD code without Potential Flow Code (JASNAOE, Volume 19)

(Authors: Emel Tokgoz, Yan Naing Win, Kazuhiro Kuroda, Yasuyuki Toda)

Curriculum vitae

Personal Information

Date of Birth : 17th September, 1986 (28 years old)
Gender : Male
Marital Status : Single
Nationality : Myanmar
Language Proficiencies : Burmese, English, Japanese
Contact Number : +81 80 3852 5214
Contact Email : indigozodiac@gmail.com
: Yan_Naing_Win@naoe.eng.osaka-u.ac.jp

Educational Background

B.E. : Myanmar Maritime University (December 2002 to April, 2008)
(Naval Architecture and Ocean Engineering)

M.E. : Osaka University (October, 2009 to September, 2011)
(Naval Architecture and Ocean Engineering)

Ph.D. (expected): Osaka University (October, 2011 to September, 2014)
(Naval Architecture and Ocean Engineering)

Scholastic Achievement

The 2006 RINA-MYANMA Shipyards Student Naval Architect Award (by the Royal Institution of Naval Architects, United Kingdom)

Technical Skills

Operating systems : Windows, Mac, Linux (Redhat in Clusters, Ubuntu)

Software	:	AutoCAD, PointWise Gridgen, Microsoft Office, Tecplot, MaxSurf
Languages	:	Fortran, C, C++

Research History

In my undergraduate final year thesis, I have carried out the designing of the planning hull patrol boat. It was a test of the design knowledge for a naval architect and to promote my capability of software usage. Based on the mother ship (boat) lines plans, I modified and designed according to the requirements of the patrol coast guard planning hull. Using the Maxsurf Student version software, I could analyze the resistance, the design draft and the necessary power prediction. The GA (General Arrangement) plan was out of the scope at that time as the shortage of project time, but the rough arrangement of the engine and the propeller could have been sketched.

In my graduate school as a master student, I was a team member of CFD groups in my laboratory. My research was to transform the original computation code of the laboratory which is in ship-fixed non-inertial coordinate system into the earth-fixed inertial coordinate system. The code has a time discretization by Euler backward scheme and Finite-Analytic Method for Space discretization. Using the transformed computation code, I have carried out the maneuvering motions test using Wigley model up to three degrees of freedom. All are captive model tests including pure yaw, pure sway and circular motion tests which are comparatively much easier than the one in non-inertial code. That was the part of developing code that I have carried out in my master student life.

In my current research, I am doing the propeller-hull and propeller-hull-rudder interaction using the simple body-force propeller model which has been developed in our laboratory. Using the computation code CFDSHIP-Iowa 4, the computation is carried out by overset grid type with MPI based domain decomposition. The facility of the computer currently using is Clusters with 100 CPUs owned by the laboratory. The current computation is based on the ship-fixed case and the future work will cover the free running test or self-propulsion test with the proposed propeller model. In addition to the current publications, more publications will be submitted before graduation.

Employment History

(1) Project Engineer

Plant Engineering Construction Pte Ltd (Singapore)
(April 2008 to August 2008)

As a fresh graduate, I was assigned at the tendering department of the company at first. After training for two months, I was sent to one of the construction sites that was the construction of Pharmaceutical factory. The main job of the company is to construct the pipeline of factories. In this work, I had to deal with pipeline drawings and worked together with planning engineer. Sometimes, I had to stay at sites and dealt with the drawings and the actual construction layout. After 5 months of working in this company, even though I enjoyed the type of work, I preferred to work as Naval Architect and I decided to resign the job.

(2) Naval Architect (Marine Warranty Surveyor)

London Offshore Consultants Pte Ltd (Singapore Branch)
(September 2008 to August 2009)

The scopes of work included the surveying of all projects for FPSO conversion. The projects included the documents review, consulting, discussing and advising the clients as well as the site attendance and issuing the approval for operations such as load-in, load-out operations, barge and tug inspections, sea-fastening/lashing inspections, heavy lift operation inspection and installation inspections of these modules to the FPSO. The documents review was based on the naval architecture and engineering knowledge and site attendance and meeting with clients was based on the social communication skills. Occasional scopes also included the writing of quotation and tendering proposal to the clients. While I was working at LOC (Singapore), I have accomplished one FPSO conversion project completely and one quotation submission completely.

(3) Teaching Assistant

Department of Naval Architecture and Ocean Engineering, Osaka University
(May 2012 to March 2013)

The scopes of work included assisting of Professors for their teaching classes and experimental classes. From May, 2012 to August, 2012, I have assisted Professor Yasuyuki Toda in his resistance test experimental teaching at University's circulating water channel. The students are third year undergraduate students and I have assisted the preparation of the channel, the teaching board and helped the students in reading the experimental result. From October, 2012 to March, 2013, I have assisted the teaching class belonged to Division of Global Architecture of Osaka University. The class was taught by Professors from Architecture, Civil Engineering and Naval Architecture Departments and I have assisted by preparing and distributing of the teaching materials for students, collecting the class attendance and taking responsibility for examination room.

Disclaimer: The information provided in the curriculum vitae is true and references will be provided once asked upon.